Astrophysical Applications of Gravity-waves

by Bence Kocsis

A dissertation submitted in conformity with the requirements for the degree of
Doctor of Philosophy

Thesis advisor:	PhD program leader:	PhD school leader:
Dr. Zsolt Frei	Dr. Ferenc Csikor	Dr. Zalán Horváth
Associate Professor	Professor of Physics	Professor of Physics

Particle Physics and Astronomy PhD Program
Eötvös Loránd University, Institute of Physics

Budapest, Hungary
2007

Declaration

This dissertation is the result of my own work, except where explicit reference is made to the work of others, and has not been submitted for another qualification to this or any other university.

Bence Kocsis

Acknowledgements

Of the many people who deserve thanks, some are particularly prominent:

Above all, I would like to thank my supervisor Zsolt Frei for the continuous help, support, and inspiration, and my outside advisors, Zoltán Haiman, Szabolcs Márka, Kristen Menou, and Abraham Loeb without whom this work could not have been completed. I am also very greatful for Merse E. Gáspár for intriguing discussions and lots of help during the start of the project about the parabolic encounters.

I would like to express my gratitude to Scott Hughes and Dan Holz for useful discussions, to Sheng Wang for providing the Fisher matrices for the cosmological uncertainties, Samuel Finn and Shane Larson for influential early discussions on the premerger localization problem, and Tom Prince for valuable comments on the corresponding publication. Moreover, I thank Kip Thorne for initial motivation and suggestions about the parabolic encounter project and thank Luca Matone, Peter Shawhan, Patrick Sutton for valuable comments on the published paper and the LIGO Scientific Collaboration Review, in particular Vicky Kalogera for pointing out the relevance of Spitzer instability for my estimates. I am grateful for the Caltech SURF program and the LIGO collaborationm, the Smithsonian Astrophysical Observatory Predoctoral Fellowship, and NKTH's Öveges József Fellowship for support. I am very honored by the Association of the Hungarian PhD Students Best Publication Award for recieving the first prize in two successive years for the papers Kocsis, Haiman, & Frei (2005) and Kocsis, Gáspár, & Márka (2006).

And above all, I thank my wife all of the love and encouragement, supporting my dedication and efforts, and thereby enabling this work to be completed at the highest level of my abilities.

Contents

List of Figures

List of Tables

Chapter 1

Introduction and Overview

The observation of gravitational waves (GWs) is expected to open a new window on the universe within the following decade. First generation GW detectors (InLIGO, VIRGO, TAMA, GEO) are already operating at or close to their design sensitivity levels and the development of the next advanced-sensitivity GW detectors (Advanced LIGO, Advanced Virgo, LCGT) and the space-detector LISA are well underway. The community is eagerly waiting for the "first light" to show up in the datastreams; up to the present day, no GWs detections have been yet reported. It is now increasingly important to assess the spectrum of possibilities that this phenomenon entails for astronomy and astrophysics, and to fully understand the precise characteristics of the gravity waveforms that we expect to observe. In addition to its fundamental theoretical importance, the research in the emerging field of GW astronomy also helps to tune technical developments of GW detection facilities. My PhD research focuses on three different fields in gravitational wave astronomy: (1) standard sirens, (2) GW parameter estimation, and (3) GW event rate computation. I elaborate the main motivations and provide a brief overview of the previous related works to my studies below.

Standard sirens are supermassive black hole (SMBH) merger events that produce both gravitational and electromagnetic (EM) radiation. The spectrum of the EM waves allows to determine the redshift, while the measurement of gravitational radiation gives direct independent information on the luminosity distance of the source. Combining these information, standard sirens are capable of probing the cosmological model of the universe, but to higher redshifts and with different systematics than the analagous type-Ia supernova standard candles. Moreover, the secure identification of the EM counterpart to even a single GW event could be also useful to improve our understanding of the SMBH accretion physics and to clarify the role of gas as a catalyst in SMBH mergers. A joint GW-EM analysis could, in principle, determine the masses and orbital parameters of the SMBH binary and yield a precise measurement of the Eddington ratio, $L/L_{\rm Edd}$, which will supply a key parameter in studies of the evolution of the BH/quasar population. Finally, the comparison of the EM variability with the GW-kick and spin observables would give new insights to BH accretion physics. For all of these reasons the observation of standard sirens are among the key goals of the planned LISA instrument. In fact, the results of my analysis have already made an impact on the LISA design, and have been included in the Science Requirements of the LISA Proposal.

Previously, it has been argued (Vecchio, 2004) that the GW source localization accuracy corresponding to the LISA measurement is too poor, and the identification of such EM counterparts will be difficult because there will be too many counterpart candidates to choose from. However, Vecchio (2004) associated counterparts with host galaxies and galaxy clusters, and used only the 2D angular positioning information for the analysis. I improved previous analyses by accounting for the full 3D spatial information by using the redshift of an EM counterpart candidate in relation with the luminosity distance determined by LISA and I focused on quasars as plausible counterparts. With these specifications, one can expect that a specific counterpart can be uniquely determined. Another possibility I have examined is to monitor the sky for EM counterparts in real time, even as the SMBH inspiral proceeds. Arguably, searching for a variable or transient EM signal, produced during the GW emitting phase, could be one of the most efficient ways to uniquely identify EM counterparts. Indeed, the exact nature of any such "prompt" counterpart is difficult to predict ab initio. The presence of gas is believed to be necessary to allow the coalescence of the binary on pc scales within a Hubble time (Escala et al., 2004). If one or both SMBHs continues to accrete gas in the GW-emitting stage, the coalescing binary may shine as a bright quasar (Armitage & Natarajan, 2002; Kocsis et al., 2006), with potential variability on a timescale of hours to days, owing to the inspiraling orbital motion of the binary. I have examined whether the LISA detector can constrain the position of the GW event to a precision that an EM counterpart be observed.

Aside from the astrophysical significance, this work is also important for the fundamental theory of GW parameter estimation. Unlike regular telescopes, the GW instruments are sensitive to sources from all directions on the sky and to all of the intrinsic parameters describing the sources. The development of data processing techniques on separating individual GW events from instrumental and astrophysical noise, is an outstanding task. Once the waveform of a given physical event has been separated, the various physical parameters describing the event have to be disentangled. Given the characteristics of the existing and planned GW instruments, and the theoretical expectations on GW sources, it is possible to obtain the expected error covariance of the physical parameter estimators. I have analyzed this problem to understand whether the early inspiral phase of SMBH binary mergers can be used to forcast the time and three dimensional position of the merger, before the merger actually happens. I was looking to find whether the parameter estimator covariance matrix has a special structure for the LISA GW instrument, and to see how it changes in time as the observation proceeds. Such a special structure can be expected due to the geometry of the motion of LISA, as it orbits around the Sun. This motion adds a periodic modulation to the waveform with a much smaller frequency than the GW carrier signal. Previous works (e.g. Berti et al., 2005a; Holz & Hughes, 2005; Hughes, 2002a; Vecchio, 2004) made no use of this special structure, and therefore were limited by computational resources. After devising a new algorithm and a new approximation scheme, such limitations can be hoped to be overcome, which has been the second driving goal of my research.

Finally, I have conducted research on the expected event rates of GWs. On the verge of the first direct GW detection, it is especially important to analyze the detection capabilities of the existing and planned GW detectors and to estimate the rates and characteristics of potentially detectable GW signals. There is already a considerable list of possible detection candidates (for a review see Cutler & Thorne, 2002): the inspiral of neutron star (NS) or black hole (BH) binaries, the tidal disruption of NS by BH in NS–BH binaries, BH–BH merger and ringdown, low-mass X-ray binaries, pulsars, centrifugally hung-up proto neutron stars in white dwarf accretion-induced collapse, supernova core collapse, gamma ray bursts, and the stochastic background.

In my thesis, I consider an additional possibility, GWs produced by unbound orbits. Among unbound orbits near-parabolic encounters (PEs) produce gravitational radiation with typical frequencies appropriate for detection with terrestrial facilities. For close PEs the gravitational radiation is short and intensive, that is observable to large distances. Parabolic encounters are primarily expected to occur in very dense environments of compact objects like galactic nuclei and globular clusters, but very little attention had been paid to any of these cases in the previous literature. In my pioneer study, I have considered the latter possibility and estimated the expected event rate of detections for specific current and near-future GW detectors. The most interesting aspect of these studies is that the resulting event rates are very sensitive to the model parameters.

Therefore the comparison of these estimates with observations with GW instruments in the future will make it possible to put stringent constraints on the composition and distributions of compact object populations of these systems.

The thesis is organized into three main segments described above. In Chapter 2, I derive expectations on locating the quasar counterparts of standard sirens. In Chapter 3, I present an analysis of the premerger localization of gravitational-wave inspirals. In Chapter 4, I discuss the detection rates of parabolic encounters. Finally, in Chapter 5 I draw the concluding remarks and summarize the most important findings in an itemized list of theses. Each of the chapters are written to be self-complete and can be comprehended individually without the necessity of reading the remainder of the Thesis. The various chapters of the thesis are based on the publications: Kocsis, Frei, Haiman, & Menou (2006); Kocsis, Gáspár, & Márka (2006); Kocsis, Haiman, Menou, & Frei (2007); and Kocsis, Haiman, Menou, & Frei (2007).

Chapter 2

Locating the Quasar Counterparts of Standard Sirens

2.1 Introduction

One of the main objectives of the *Laser Interferometric Space Antenna* (*LISA*), to be launched around the year 2018 (Danzmann & Rüdiger, 2003), is to detect the gravitational wave (GW) signals associated with coalescing supermassive black holes (SMBH) at cosmological distances. The *LISA* detector is designed to be particularly sensitive in the frequency range between $(3\times10^{-5}-10^{-4})\mathrm{Hz}\lesssim f\lesssim0.1\mathrm{Hz}$, allowing the detection of binary coalescences with total masses between 10^4 and $10^7\,\mathrm{M}_\odot$ out to high redshifts. The limiting redshift depends on several factors (such as the orientation of the spins and orbital plane of the SMBH binary, and its location on the sky relative to *LISA*), and is expected to lie between $z\sim5-10$ (Hughes, 2002b). A comparison of the gravitational waveform with the anticipated detector noise can be used to estimate the accuracy with which *LISA* will be able to extract the physical parameters of the coalescence events (Barack & Cutler, 2004b; Holz & Hughes, 2005; Hughes, 2002b; Vecchio, 2004). Of particular interest, in the context of searching for electromagnetic (EM) counterparts, is whether the spatial location of the GW event can be localized to within a sufficiently small three-dimensional volume. In this chapter, I determine the probability of finding a unique EM counterpart within the expected error volume associated with SMBH merger events, for a range of masses and redshifts.

It has been argued by Vecchio (2004) that the identification of such EM counterparts will be difficult because, in typical cases, there will be too many counterpart candidates to choose from. However, Vecchio (2004) associated counterparts with host galaxies and galaxy clusters, and used only the 2D angular positioning information for the analysis. In contrast, here I account for the 3D spatial information by using the redshift of an electromagnetic counterpart candidate in relation with the luminosity distance determined by *LISA* and I focus on quasars as plausible counterparts. With these specifications, I shall demonstrate that in some cases, a specific counterpart can be uniquely determined.

If electromagnetic counterparts to *LISA* events exist, they will likely be related to the accretion of gas onto the SMBHs involved in the coalescence. Provided this accretion is not supply-limited, bright quasar counterparts approaching the Eddington luminosity would then be expected. A few additional arguments favor this scenario: galaxy mergers in hierarchical scenarios of structure formation are expected to deliver a significant amount of gas to the central regions of the merging galaxies (Barnes & Hernquist, 1992), and this gas may play a catalyst role in driving SMBH coalescence (Begelman et al., 1980; Escala et al., 2004; Gould & Rix, 2000). Ultimately, however, many of the complex processes involved remain poorly understood. For example, Armitage & Natarajan (2002) have argued that, in the limit of a small mass ratio of the two SMBHs, a prompt and luminous electromagnetic signal may be expected during coalescence, while Milosavljevic & Phinney (2005) have argued that in the limit of equal mass SMBHs, only a much delayed electromagnetic afterglow would be expected. All "cosmological standard sirens" may thus not be equal in their potential for electromagnetic counterparts. [1] My working assumption in the present study is that bright quasar activity is a plausible electromagnetic counterpart to *LISA* events. This allows us to quantify the feasibility of an unambiguous identification of such a counterpart. As I shall see below, the search for the counterparts will allow a test of the assumption, as well.

The secure identification of the EM counterpart to even a single GW event could be useful in different ways: (1) to improve our understanding of the SMBH accretion physics, (2) to clarify the role of gas as a catalyst in SMBH mergers and (3) to supply an independent constraint on the background cosmology. A joint GW – EM analysis could, in principle, determine the masses and orbital parameters of the SMBH binary, and yield a precise measurement of the Eddington ratio, $L/L_{\rm Edd}$, which will supply a key parameter in studies of the evolution of the BH/quasar population (Haiman &

[1] The name "standard sirens" was suggested by Sterl Phinney and Sean Carroll (Holz & Hughes, 2005).

Loeb, 1998; Haiman & Menou, 2000; Kauffmann & Haehnelt, 2000; Small & Blandford, 1992; Wyithe & Loeb, 2003). This parameter is currently poorly known (constrained by indirect empirical correlations; Vestergaard 2004, Woo & Urry 2002, Kaspi et al. 2000). The values range from ≈ 0.1 to $\gtrsim 1$, with indications that higher-z quasars may be closer to $L_{\rm Edd}$ than the $z \sim 0$ quasars. Likewise, a joint GW – EM analysis could, in principle, be used to estimate cosmological parameters (Schutz, 1986), by comparing the luminosity distance (which is a direct observable by GWs) with the redshift (as inferred from the spectrum of the counterpart – in this case, a quasar). This would serve as a complement to constraints from the luminosity distance to high-z type Ia Supernovae (SNe), but with different systematic errors, and with the potential of extending to higher redshifts. New constraints, spanning the range $0 < z < 2$, would be particularly well–suited to probe the properties of dark energy, which is expected to become dynamically dominant within this cosmic epoch.

This chapter is organized as follows. In Section 2.2, I summarize my method to estimate the angular and radial positioning errors expected from *LISA*, for SMBHs with a range of masses at different redshifts. In Section 2.3, I discuss the conversion of the luminosity distance, as determined by *LISA* from the GW signal alone, to the redshift of the source. In particular, I discuss the uncertainty in the resulting redshift estimate. In Section 2.4, I discuss my estimates for the number of quasars that may be found in the 3D error volume provided by *LISA*, based on the luminosity function and clustering properties of known optical quasars. In Section 2.5, I present the main results, and show that for typical low-redshift GW events discovered by *LISA*, a unique quasar counterpart may be identified. In Section 2.6, I point out various implications of a successful identification and discuss several caveats to this conclusion. Finally, in Section 2.7 I summarize the conclusions. Unless stated otherwise, throughout this chapter I assume a standard cold–dark matter cosmology (ΛCDM), with (Ω_Λ, Ω_M, Ω_b, H_0) = (0.70, 0.30, 0.047, 70 km s^{-1} Mpc^{-1}), consistent with the recent results from the *Wilkinson Microwave Anisotropy Probe (WMAP)*(Spergel et al., 2003) and the Sloan Digital Sky Survey (SDSS) (Tegmark et al., 2004a).

2.2 Localizing LISA events

A few studies have been carried out so far to address how accurately *LISA* will measure the source parameters of a coalescing pair of SMBHs. In general, the accuracy

Table 2.1. *LISA* measurement errors

	$\delta\mathcal{M}/\mathcal{M}$	$\delta\mu/\mu$	$\delta d_{\rm L}/d_{\rm L}$	$\delta\Omega$
best	0.8×10^{-5}	2×10^{-5}	2×10^{-3}	$0.01\,\mathrm{deg}^2$
typical	2×10^{-5}	9×10^{-5}	4×10^{-3}	$0.3\,\mathrm{deg}^2$
worst	0.8×10^{-3}	0.1	2×10^{-2}	$3\,\mathrm{deg}^2$

Note. — Assumed SMBH binary parameters: $m_1 = m_2 = 10^6\mathrm{M}_\odot$ and $z = 1$.

depends on a large number of parameters: a total of 17 parameters in the most general case include 2 red-shifted mass parameters, 6 parameters related to the BH spin vectors, the orbital eccentricity, the luminosity distance, 2 angles identifying the position on the sky, 3 angles that describe the orientation of the orbit, a reference time, and a reference phase. Due to the resulting computational limitations, various studies have concentrated on small portions of the parameter space. The most up–to–date calculations estimating parameter uncertainties for SMBH in-spirals have been carried out by Berti et al. (2005a); Holz & Hughes (2005); and by Vecchio (2004). As compared to previous studies, Vecchio (2004) accounts for the effects of spins, and shows that parameter estimation errors improve significantly (by a factor of 3–10 for high spins) for selected parameters. Vecchio (2004) also adopts an optimistic *LISA* sensitivity curve, by adopting the smallest observable frequency to be ~ 3 times lower than previous estimates and only considers cases with equal mass SMBHs. My analysis, which relies on Vecchio's estimates, is therefore approximate to this extent.

For concreteness, I adopt the parameter uncertainties obtained by Vecchio (2004) for an equal-mass SMBH binary with $m_1 = m_2 = 10^6\mathrm{M}_\odot$ at redshift $z = 1$. The uncertainties vary as a function of the fiducial orientation of the source relative to *LISA*, and are primarily influenced by the BH spin magnitudes (i.e. higher spins lead to smaller uncertainties). Here I distinguish three cases. In the "best" case, I adopt the errors that correspond to the 10th percentile of the distribution of uncertainties obtained by Vecchio (2004) for high BH spins (with dimensionless spin $a = S/M^2 = 0.9$, where S is the magnitude of the total spin and M is the total mass). In the "typical" case, I adopt the errors corresponding to the 50th percentile in the case of moderate BH spins, with $a = 0.5$. In the "worst" case, I adopt the 90th percentile of the no spin case ($a = 0$). Note that SMBHs are generally expected to be spinning fast (e.g. Volonteri et al. 2005), so that our "best" case may actually be representative of a fair fraction of events. In Table 2.1, I list the errors on the chirp and reduced masses, $\mathcal{M} = (m_1 m_2)^{3/5}/(m_1+m_2)^{1/5}$ and $\mu = (m_1 m_2)/(m_1+m_2)$ respectively, and on the GW source location (i.e. luminosity distance, $d_{\rm L}$, and solid angle, Ω), for these three cases of interest.

In Vecchio (2004), parameter errors have only been estimated for a single choice of an equal–mass SMBH binary with total mass $M_0 = m_1 + m_2 = 2 \times 10^6 {\rm M}_\odot$ and redshift $z_0 = 1$. Starting from this result, I crudely estimate the uncertainties $\delta d_{\rm L}$ and $\delta\Omega$ for other combinations of masses and redshifts as follows. First, note that the luminosity distance is simply proportional to the inverse of the signal amplitude. Therefore its estimator depends primarily on the total signal power, rather than on the specific shape of the signal waveform[2]. The luminosity distance error would then obey the simple scaling

$$\frac{\delta d_{\rm L}(M,z)}{d_{\rm L}(M,z)} = \left[\frac{SNR(M,z)}{SNR(M_0,z_0)}\right]^{-1} \frac{\delta d_{\rm L}(M_0,z_0)}{d_{\rm L}(M_0,z_0)} \tag{2.1}$$

where $SNR(M,z)$ is the expected value of the signal to noise ratio of the detection,

$$SNR^2(M,z) = 4\int_{f_{\rm a}(M_z,\Delta T)}^{f_{\rm isco}(M_z)} \frac{h^*(f,M_z,z)h(f,M_z,z)}{S_n(f)}{\rm d}f. \tag{2.2}$$

Here, $M_z = (1+z)M$ is the red-shifted total mass, $h(f, M_z, z)$ denotes the Fourier decomposition of the signal detected by *LISA*, and $S_n(f)$ is the RMS noise density per frequency interval (including instrumental and confusion noise, Barack & Cutler 2004b[3]). A crucial parameter for high M_z values inscribed in $S_n(f)$ is the low frequency wall of the detector, which is further discussed below. The integration bound $f_{\rm isco}(M_z)$ corresponds to the innermost stable circular orbit (ISCO), beyond which the gravitational waveform is not well known, and $f_a(M_z, \Delta T)$ is the arrival frequency a time ΔT before the ISCO is reached by the coalescing binary (see Vecchio 2004 for details). Throughout this chapter, I fix the observation time of SMBH binaries at $\Delta T = 1$ yr, unless a binary is so massive or at such a high redshift that it is not observable by *LISA* for a full year and then

[2]The signal power also scales with the red-shifted chirp mass as $\mathcal{M}_z^{5/6}$. However, this parameter can be determined independently to high precision, from the phase information.

[3]For the instrumental noise, instead of the approximation of Barack & Cutler (2004b), I use the more exact sensitivity curve available at http://www.srl.caltech.edu/˜ shane/sensitivity/.

$\Delta T < 1$ yr. Note that $h(f, M_z, z)$ depends on other parameters, such as the angular momentum vector orientation relative to *LISA*'s arms, the magnitude of spins, etc. (see Vecchio 2004 and references therein). For this estimate I calculate the SNR with the leading order (i.e. Newtonian) contribution. The resulting dependence of the signal–to–noise ratio on BH masses and redshift are shown in Figure 2.1. The figure shows that the sensitivity degrades significantly for distant sources, and also that it peaks in the mass range of $10^5 - 10^6$ M$_\odot$, which produce GWs near the optimal frequencies within the *LISA* band.

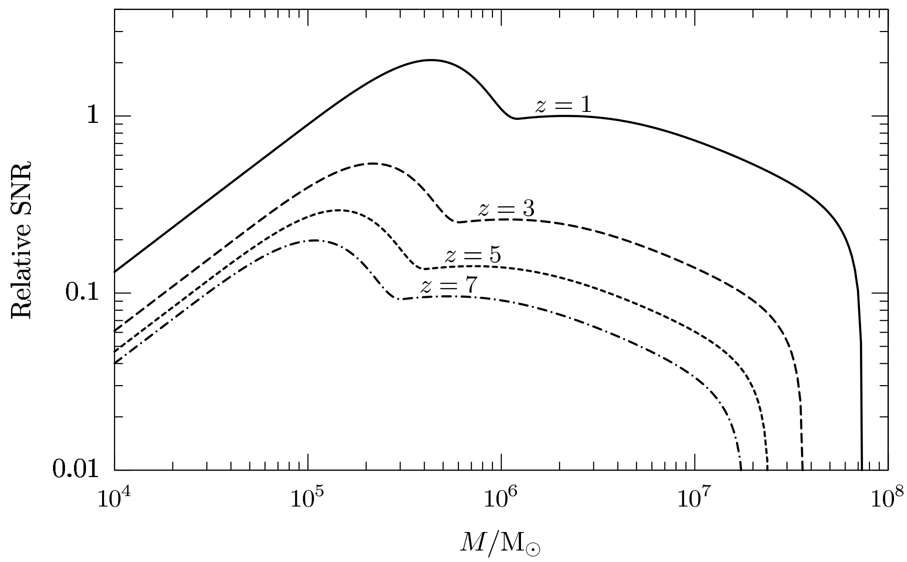

Figure 2.1 Relative signal–to–noise ratio (SNR) for *LISA* detections of the in-spiral phase of equal–mass supermassive black hole coalescences, as a function of total mass, M, and redshift, z. A 1–year observation is assumed and the normalization is for $M = 2 \times 10^6$ M$_\odot$ and $z = 1$.

The other important parameter, the angular position, is extracted from the change in the relative orientation of *LISA* during its orbit around the Sun. Since *LISA*'s orbital time–scale is much longer than the inverse of the signal frequency, it is plausible to assume that the angular position uncertainty decouples from the intricate waveform, and improves linearly with the signal amplitude. This assumption is consistent with Fig. 1 of Berti et al. (2005c) which shows that the inclusion of spin-orbit and spin-spin terms modifies the waveforms but does not alter the angular resolution. In fact, the angular resolution is shown to be independent even for alternate theories of gravity (e.g. scalar-tensor and massive graviton theories). Thus, similar to equation (2.1), I estimate the mass and redshift dependence of the positioning solid-angle error as

$$\delta\Omega(M,z) = \left[\frac{SNR(M,z)}{SNR(M_0,z_0)}\right]^{-2} \delta\Omega(M_0,z_0), \tag{2.3}$$

where the -2 exponent assumes that the uncertainty in this two–dimensional quantity is the product of independent uncertainties in the one-dimensional azimuthal and polar angles.

A limitation of the above analysis at the high–mass end of the range of SMBHs is that these events may not be visible for a full year, due to the low–frequency noise wall, below which *LISA* looses sensitivity. For instance, for $M_z > 9 \times 10^6 \mathrm{M}_\odot$ ($1.3 \times 10^6 \mathrm{M}_\odot$), the low frequency noise wall at 0.03mHz (0.1mHz) is crossed less than 0.25yr before reaching the ISCO. At higher masses or redshifts, therefore, the angular information, which is inscribed in a modulation with a 1yr period, becomes significantly harder to disentangle from other parameters, such as d_{L}, and the errors estimated from the SNR alone by equations (2.1) and (2.3) become less accurate. In this regime, a better approximation to the scaling of the errors is $\propto (\Delta T/1\ \mathrm{yr})^{-1/2} \times SNR^{-1}$, where $\Delta T \leq 1$ yr is the time elapsed from the moment the binary appears at the low–frequency wall to the moment it reaches the ISCO (Hughes 2005, private communication; see Holz & Hughes (2005) for a more detailed treatment and discussion).

2.3 Localizing the Counterparts

I next consider how to use the three–dimensional spatial localization of the SMBH merger event by *LISA*. The solid angle error box directly yields the two–dimensional angular position error on the sky, in which any EM counterpart will be located. However, an additional step is necessary to convert the luminosity distance, d_{L}, measured by *LISA* into a redshift, z, which is the relevant observable for the EM counterpart. With a particular choice of cosmological parameters $p_i = (H_0, \Omega_M, \Omega_{DE}, w)$, I can directly convert a redshift to a luminosity distance (see equation (2.4) below), and vice–versa. One may then envision the following strategy: given the precision with which p_i are known from other observations, one can estimate the redshift, and restrict the search for counterparts within the redshift shell corresponding to the *LISA*-measured luminosity distance, d_{L}. If a counterpart is uniquely identified within this redshift shell, and its redshift can be determined precisely, then one could hope for an improved measurement of the $d_{\rm L}(z)$ relation, and hence a refined determination of the cosmological parameters.

The first step in this exercise is to determine the expected redshift of the source. Apart from the errors on the cosmological parameters and on the measurement of $d_{\rm L}$, the peculiar velocity of the source relative to the Hubble flow, and its magnification due to weak gravitational lensing by inhomogeneities in the distribution of mass along the line of sight, introduce two additional sources of errors. In summary, the redshift uncertainty will thus include a combination of uncertainties from (i) the *LISA* luminosity distance, (ii) the cosmological parameters, (iii) peculiar velocities, and (iv) weak gravitational lensing magnification.

Hughes (2002b) made a simplified estimate of the redshift error, without peculiar velocities or gravitational lensing distortions, assuming a flat cosmology with a cosmological constant (assuming $\Omega_M \equiv 1 - \Omega_\Lambda$ and $w \equiv -1$), and ignoring correlations with other cosmological parameters. Here, I extend that study by using a general form of dark energy (relaxing the w prior), by taking into account the various parameter correlations, and by including errors due to peculiar velocities and gravitational lensing.

To begin, I recall the luminosity distance to a source at a fixed comoving coordinate in a smooth Friedmann universe,

$$d_{\rm L}(z, p_i) = (1+z)c \int_0^z \frac{{\rm d}z'}{H(z', p_i)}, \tag{2.4}$$

where

$$H(z, p_i) = H_0 \sqrt{\Omega_M (1+z)^3 + \Omega_{DE}(1+z)^{3(1+w)}}. \tag{2.5}$$

I ignore spatial curvature and set $\Omega_k = 0$, in line with previous studies and as suggested by recent *WMAP* data. For a source with a small but non–zero radial peculiar velocity, v, equation (2.4) is modified, and the luminosity distance is given by

$$d_{\rm L}(z, p_i, v) = d_{\rm L}[z_v, p_i, 0], \tag{2.6}$$

where $\Delta z \equiv z_v - z = (1+z)v/c$ is the additional apparent redshift due to the peculiar motion. In an inhomogeneous universe, sources along different lines of sight can suffer different amounts of gravitational lensing magnification μ. If μ denotes the magnification of the signal power, then the GW amplitude, and thus the inferred value of $d_{\rm L}^{-1}$, scales as $\mu^{1/2}$. For a line of sight that suffers a magnification μ, equation (2.6) is modified as

$$d_{\rm L}(z, p_i, v, \mu) = \frac{1}{\sqrt{\mu}}\, d_{\rm L}[z_v, p_i, 0, 0]. \tag{2.7}$$

In the limit of weak lensing $\mu^{1/2} \simeq 1 + \kappa$, where $\kappa \ll 1$ denotes the weak lensing convergence (see below).

Taking the variation in both sides of equation (2.7), I obtain

$$\delta d_{\rm L} = -d_{\rm L}\kappa + \frac{\partial d_{\rm L}}{\partial z}\delta z + \frac{\partial d_{\rm L}}{\partial v} v + \sum_i \frac{\partial d_{\rm L}}{\partial p_i}\delta p_i, \tag{2.8}$$

Solving for δz, taking the square and the expectation value of both sides, and using the fact that the *LISA* measurement, the peculiar velocities, and the cosmological uncertainties are independent, i.e. $\langle \delta p_i \delta d_{\rm L}\rangle = \langle v\, \delta d_{\rm L}\rangle = \langle \kappa\, \delta d_{\rm L}\rangle = \langle v\, \delta p_i\rangle = \langle \kappa \delta p_i\rangle = \langle \kappa v\rangle = 0$ for all i, I find

$$\langle \delta z^2\rangle = \left(\frac{\partial d_{\rm L}}{\partial z}\right)^{-2} \left(\langle \delta d^2_{\rm L,LISA}\rangle + \langle \delta d^2_{\rm L,cosm}\rangle + \langle \delta d^2_{\rm L,pec}\rangle + \langle \delta d^2_{\rm L,wl}\rangle\right) \tag{2.9}$$

or equivalently,

$$\langle \delta z^2\rangle = \langle \delta z^2_{\rm LISA}\rangle + \langle \delta z^2_{\rm cosm}\rangle + \langle \delta z^2_{\rm pec}\rangle + \langle \delta d^2_{\rm wl}\rangle, \tag{2.10}$$

where the notation was introduced to distinguish the intrinsic *LISA* measurement error, $\delta d_{\rm L,LISA}$, from the error resulting from cosmological parameters $\langle \delta d^2_{\rm L,cosm}\rangle$, peculiar velocities $\langle \delta d^2_{\rm L,v}\rangle$, and weak lensing magnification $\langle \delta d^2_{\rm L,wl}\rangle$. I now discuss each of these terms, whose forms and magnitudes follow directly from equation (2.7).

2.3.1 Cosmological Uncertainties

The cosmological term in equation (2.9) is

$$\langle \delta d^2_{\rm L,cosm}\rangle = \sum_{i,j} \frac{\partial d_{\rm L}}{\partial p_i}\frac{\partial d_{\rm L}}{\partial p_j}\langle \delta p_i\, \delta p_j\rangle, \tag{2.11}$$

where $d_{\rm L}$ and its derivatives are to be evaluated using equation (2.4), at the fiducial values of the cosmological parameters p_i, and for $v = \kappa = 0$. In order to place *LISA* in the context of other experiments planned in the next decade, I compute $\langle \delta d^2_{\rm L,cosm}\rangle$

from the covariance matrices $\langle \delta p_i \, \delta p_j \rangle$ expected from two future cosmological probes: *Planck*[4] (assumed to have measured the temperature and polarization anisotropies of the cosmic microwave background), and the Large Synoptic Survey Telescope, LSST[5] (assumed to have measured the power spectrum and redshift distribution of $\sim 100,000$ galaxy clusters). I adopt the forecasts for the Fisher matrices for these experiments by Wang et al. (2004). Their analysis assumes a flat background universe with 6 free parameters $(\Omega_{DE}, \omega_M, w, \omega_b, n_s, \sigma_8)$ where $\omega_M \equiv \Omega_M h^2 \equiv (1-\Omega_{DE})h^2$ defines the Hubble parameter. Note that the luminosity distance does not explicitly depend on n_s and σ_8, but they are included here, since they couple to the other four parameters as determined by *Planck* and LSST (and hence increase the uncertainties on these other four parameters). The fiducial parameters are $(0.73, 0.14, -1, 0.024, 1, 0.9)$, respectively (consistent with *WMAP*; Spergel et al. 2003). Since the two observations are independent, I simply sum up the two individual Fisher matrices; the covariance matrix, $\langle \delta p_i \, \delta p_j \rangle$, is obtained by taking the inverse of the Fisher matrix. In order to substitute in equation (2.11), it is necessary either to revert to the original cosmological parameters $(H_0, \Omega_{DE}, \Omega_M, w)$ in the correlation matrix, by performing an orthogonal transformation in the parameter space[6], or to simply write $d_{\rm L}(z, p_i)$ of equation (2.4) in terms of the parameters $(\Omega_{DE}, \omega_m, w)$ and evaluate the partial derivatives in equation (2.11) as a function of these parameters. Following either approach, I find $\langle \delta d^2_{\rm L,cosm} \rangle^{1/2}/d_{\rm L} = 1.7 \times 10^{-3}$ for $z = 1$. For comparison, I performed the same analysis using the Fisher matrices of WMAP (using only temperature anisotropies) and SDSS (using the power spectrum of the luminous red galaxies, together with the galaxies in the main SDSS survey, and following Hu & Haiman 2003 for redshift binning, mass limit, and sky coverage). I find $\langle \delta d^2_{\rm L,cosm} \rangle^{1/2}/d_{\rm L} = 1.1 \times 10^{-2}$ for $z = 1$ in that case.

The luminosity distance error corresponds to a redshift error according to equation (2.9). Note that equation (2.11) depends on the fiducial redshift through the $d_{\rm L}$ derivatives. This dependence of the redshift error is shown as a long–dashed curve in Figure 2.2, along with other sources of redshift errors. The luminosity distance at $z \approx 1000$ is measured very accurately by *Planck*, and its evolution is essentially unaffected by the cosmological parameters down to dark-energy domination at $z \lesssim 2$. The figure shows that, as a result, the relative cosmological error $\langle \delta z^2_{\rm cosm} \rangle^{1/2}/z$ reaches a constant value beyond $z \gtrsim 2$. The figure also shows that the cosmology error becomes smaller than the typical LISA uncertainty at $z \gtrsim 0.7$. I find that, even for the best–case *LISA* events,

[4]See www.rssd.esa.int/index.php?project=PLANCK
[5]See www.lsst.org
[6]The parameters $\delta\Omega_M$ and $\delta\Omega_{DE}$ will be fully anti-correlated, because of the assumption of flatness.

the cosmology error becomes sub–dominant at $z \gtrsim 1$.

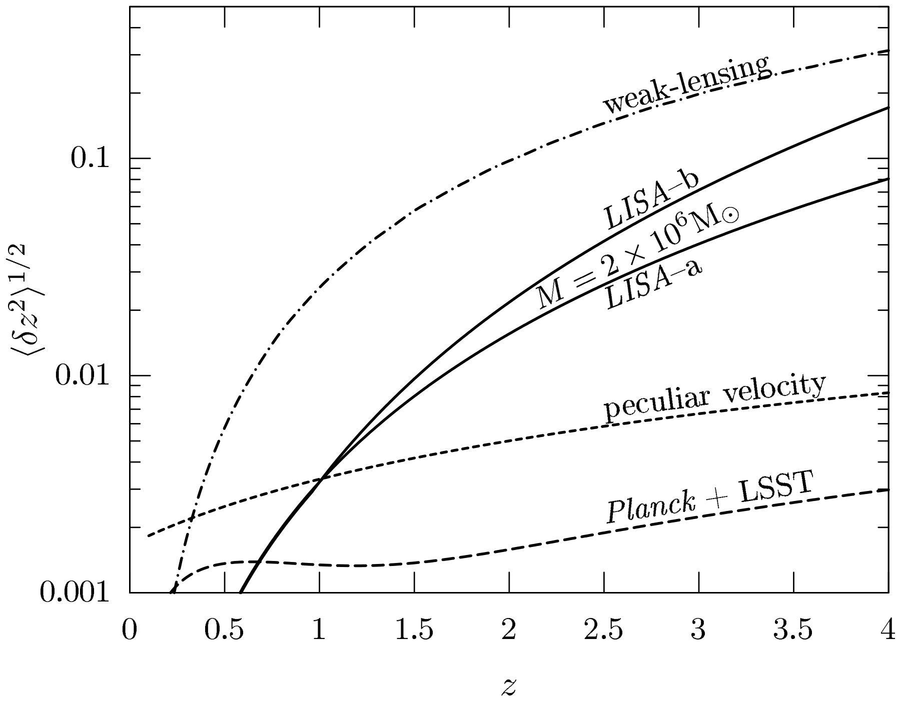

Figure 2.2 Errors on the inferred redshift of an electromagnetic counterpart to a *LISA* coalescence event, for $m_1 = m_2 = 10^6 M_\odot$. The intrinsic *LISA* error on the luminosity distance, d_L, is shown as a solid line for the two scalings $\delta d_\mathrm{L}/d_\mathrm{L} \propto SNR^{-1}$ ("*LISA*–a") and $\delta d_\mathrm{L}/d_\mathrm{L} \propto \Delta T^{-1/2} \times SNR^{-1}$ ("*LISA*–b"). Errors due to the peculiar velocity of the source (for $v = 500$ km s^{-1}; short–dashed line), uncertainties on the background cosmology (long–dashed line), and weak lensing magnification (dash–dotted line) are also shown (see text for details).

2.3.2 Peculiar Velocities

Equations (2.6), (2.8), and (2.9) yield, to first non-vanishing order in v/c, the uncertainty due to peculiar velocities, as a simple function of the r.m.s. peculiar velocity of the GW sources,

$$\langle \delta d^2_\mathrm{L,pec} \rangle / d^2_\mathrm{L} = \left[1 + \frac{c(1+z)^2}{H(z) d_\mathrm{L}} \right]^2 \frac{\langle v^2 \rangle}{c^2}. \tag{2.12}$$

I are assuming here that GW events correspond to luminous quasars, and unfortunately, the r.m.s. peculiar velocity of high-redshift quasars is not known empirically. I therefore employ theoretical predictions for the peculiar velocities of (quasar–host) galaxies within dark matter haloes. According to numerical simulations (e.g. Cen & Ostriker 2000), typical values are ~ 500 km s^{-1}, with a tail extending to ~ 1000 km s^{-1}. As an approximation, I assume that the scaling with redshift follows the linear growth in the amplitude of density perturbations, multiplied by the linear bias of the halos. Under this assumption, I find that for fixed halo mass, the typical peculiar velocity evolves very little from $z \sim 0$ to $z \sim 1$. This conclusion is consistent with the semi-analytic model of Hamana et al. (2003), which shows essentially no evolution (only a modest decrease from $z \sim 0$ to $z \sim 0.8$). Therefore, I substitute $v \sim 500$ km s^{-1} in equation (2.12) at $z \sim 1$, yielding an error of $\langle \delta d_{\rm L,pec}^2 \rangle^{1/2}/d_{\rm L} = 4.1 \times 10^{-3}$. The corresponding redshift r.m.s. error contribution (equation (2.10)) for $v \sim 500$ km s^{-1} is shown as a function of redshift in Figure 2.2 (short–dashed curve). The figure shows that the peculiar velocity error is lower than the typical *LISA* error for $z \gtrsim 1$.

Note that the r.m.s. peculiar velocity equals ~ 500 km s^{-1} in the most typical cases, but its exact value depends on the specific mass of the halo, $M_{\rm halo}$, embedding the quasar (Hamana et al., 2003), smaller $M_{\rm halo}$ implying lower velocities. For a specific source, $M_{\rm halo}$ can be estimated directly, using the number of galaxies that cluster around the identified quasar (Kauffmann & Haehnelt, 2002). The r.m.s. peculiar velocity error may then be estimated for this particular source, and may be somewhat lower/higher than the value shown in Figure 2.2, depending on whether the source is located in a galaxy–poor/galaxy–rich environment.

2.3.3 Weak Gravitational Lensing

The gravitational lensing term in equation (2.9), in the weak-lensing limit, is given by

$$\langle \delta d_{\rm L,wl}^2 \rangle / d_{\rm L}^2 = \langle \kappa^2 \rangle, \tag{2.13}$$

where κ denotes the r.m.s. effective convergence (e.g., White & Hu 2000). While the mean magnification is well approximated by $\langle \kappa \rangle = 0$ or $\langle \mu \rangle = 1$, the magnification distribution has a substantial width. The full distribution is given by Wang et al. (2002), and its variance reaches $\sim 12\%$ for sources at $z = 2$ (Dalal et al., 2003). Here I use equation (6) in White & Hu (2000) to compute the variance in effective convergence, $\langle \kappa^2 \rangle$, for point sources. This quantity is given by an integral over the matter power spectrum, and receives a contribution from small, non–linear scales. I employ the HALOFIT routine of Smith et al. (2003), and set the input cosmological parameters according to my convention (see Section 2.1). This routine encodes an accurate fitting formula for the matter power spectrum extending into the nonlinear regime. For $z = 1$, I find $\langle\kappa^2\rangle^{1/2} = 3.1\%$.

Weak lensing errors can, in principle, be improved by "corrective lenses" (Dalal et al., 2003), i.e. background galaxy shear maps, and using the cross-correlation between the magnification of a point source and the shear map smoothed on larger–scales. However, Dalal et al. (2003) found that the magnification errors can be improved by only a small amount, less then 20% relative to the uncorrected errors for a source at $z = 2$.

A different approach for reducing weak lensing magnification uncertainty would be to directly measure the inhomogeneities in the mass distribution along the line of sight. If this distribution could be directly probed down to a scale of $k_{\rm min}$, then the contributions to κ from all scales down to $k_{\rm min}$ could be directly subtracted from the uncertainty on the magnification. If the counterpart is indeed a quasar, then the line-of-sight density distribution could, in principle, be probed by studying its Lyman α absorption spectrum, as well as deep surveys of galaxies and clusters in the foreground and near the line of sight. At low redshifts ($z \sim 0.5$) which contribute significantly to the lensing magnification, the X-ray absorption forest (Fang & Canizares, 2000; Perna & Loeb, 1998) could provide additional information on the density fluctuations.

I leave a detailed assessment of the amount of correction that could be feasible to future investigations. However, to estimate the "target" scale at which the fluctuations would need to be measured in order to be useful as a lensing correction, I make the (unrealistically optimistic) simplifying assumption that the matter fluctuations above a certain length scale, and the corresponding contribution to lensing magnification, have been perfectly determined. The fluctuations on smaller scales, with $k > k_{\rm min}$, then determine the only remaining weak-lensing uncertainty. Therefore, I truncate the integral over the wavenumber (see equation (1) in Dalal et al. 2003) at $k_{\rm min}$. The resulting fractional improvement in $\langle\kappa^2\rangle^{1/2}$ (which equals $\delta d_{\rm L,wl}/d_{\rm L}$) is plotted in Figure 2.3. The improvement is about 8%, 20%, and 40% for $k_{\rm min} = 1$, 3, and 10Mpc^{-1}, respectively - i.e., about half of the weak lensing uncertainty is from length–scales $\lesssim 2\pi/k_{\rm min} \sim 0.6$ Mpc. The Lyman α transmission spectra of SDSS quasars have been used to determine the power spectrum down to scales of $k \sim 3$Mpc^{-1}, implying that the spectral resolution would need to be improved by a factor of ~ 3 to allow significant improvements.

The uncorrected weak-lensing redshift uncertainty $\delta z_{\rm wl} \equiv (\partial d_{\rm L}/\partial z)^{-1}\langle\delta d^2_{\rm L,wl}\rangle^{1/2}$ is shown in Figure 2.2. The plot clearly shows that weak lensing errors typically exceed

1% and dominate the other redshift errors for $z > 0.5$.

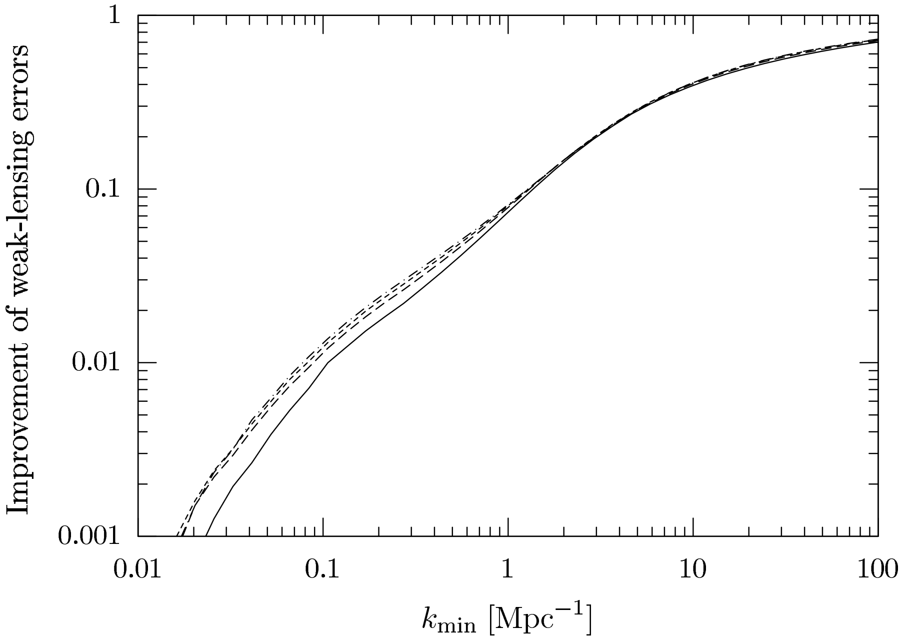

Figure 2.3 The relative improvement in the weak lensing magnification–induced redshift uncertainty to a background source. I show the fractional improvement that can be achieved by perfectly measuring density inhomogeneities down to a fixed scale. The x-axis shows the minimum wave number that is unmapped (larger scale fluctuations are assumed to be perfectly known along the line of sight to the source). Various curves correspond to sources at $z = 1$, 2, 3, and 4 (from bottom to top).

2.3.4 The Size and Orientation of the Error Volume

In Figure 2.2, I compare the contributions from four different sources of redshift errors: $\langle \delta z^2_{\rm LISA} \rangle^{1/2}$, $\langle \delta z^2_{\rm pec} \rangle^{1/2}$, $\langle \delta z^2_{\rm cosm} \rangle^{1/2}$, and $\langle \delta z^2_{\rm wl} \rangle^{1/2}$ for SMBH masses $m_1 = m_2 = 10^6 {\rm M}_\odot$. Weak lensing errors are dominant for $5 \gtrsim z \gtrsim 0.5$. The *LISA* redshift error is shown for both scalings $\delta d_{\rm L}/d_{\rm L} \propto SNR^{-1}$ (labeled "*LISA*–a") and $\delta d_{\rm L}/d_{\rm L} \propto (\Delta T/1\ {\rm yr})^{-1/2} \times SNR^{-1}$ (labelled "*LISA*–b"). These curves separate if the total maximum mass satisfies $M_z > 3.92 \times 10^6 {\rm M}_\odot$, since in this case the maximum observation time ΔT decreases under 1 yr. The other three sources of errors are within a factor of two of one another at $z = 1$, for typical *LISA* sources and peculiar velocities.

The total redshift uncertainty then follows from summing the uncertainties in quadrature, equation (2.10). The result for $m_1 = m_2 = 10^6\ {\rm M}_\odot$ and $z = 1$ is $\delta z = 2.57\%$, 2.59%, and 3.03% in the cases I labeled as best, typical, and worst, respectively. Note that I have not explicitly added an error due to the instrumental resolution of a spectrograph, because this is often much better than this value (e.g. for SDSS[7], the redshift resolution is between 10^{-3} and 10^{-4}).

I next use these redshift uncertainties to derive the three–dimensional error volume, $\delta V_{\rm tot}$, in which the EM counterparts need to be identified. The comoving volume corresponding to the above redshift uncertainties, combined with the solid–angle uncertainty $\langle\delta\Omega^2\rangle^{1/2}$, is

$$\delta V_{\rm tot} = \frac{\partial^2 V}{\partial z \partial\Omega}\langle\delta z^2\rangle^{1/2}\langle\delta\Omega^2\rangle^{1/2}. \tag{2.14}$$

Substituting the solid–angle errors from Table 2.1, I find $\delta V_{\rm tot} = 2.1\times10^3$, 6.3×10^4, and $7.4\times10^5{\rm Mpc}^3$ for the same three cases.

Equation (2.14) should be regarded as a simple estimate of the volume that needs to be searched. The 2D uncertainty $\langle\delta\Omega^2\rangle^{1/2}$ was obtained by a Fisher analysis, and represents the solid area of a 2D error ellipse. This equation then gives the volume of a cylinder with a height of $\langle\delta z^2\rangle^{1/2}$. The arguably more appropriate volume of an ellipsoid whose third semi–axis is $\langle\delta z^2\rangle^{1/2}$ would be a factor of 4/3 larger. On the other hand, equation (2.14) also naively assumes that δz and $\delta\Omega$ are uncorrelated – i.e., it describes an error ellipsoid whose z axis is oriented along the line of sight. The angular position is estimated by *LISA* from the GW signal alone, and is therefore indeed uncorrelated with the radial uncertainties due to cosmology, lensing, or peculiar velocities. However, the luminosity distance estimate from *LISA* itself is strongly correlated with its angular positioning (Hughes, 2002b), which results in an error ellipse that is 'tilted' relative to the line of sight, and has a smaller overall volume than the simple orthogonal product in equation (2.14) would imply.

I have utilized the correlation matrices for the *LISA* distance and angle estimates given in Table 1 and 2 of Hughes (2002b) for $m_1 = m_2 = 10^5{\rm M}_\odot$ at $z = 1$ and $m_1 = m_2 = 10^4{\rm M}_\odot$ at $z = 7$, to estimate the reduction in the total error volume due to these correlations. Note that this analysis applies only to the *LISA* uncertainties. Among the 11 free parameters in Hughes (2002b), the 3D error volume is determined by the parameters related to the spherical coordinates of the sources: $\ln d_{\rm L}$, $\mu_S = \cos\theta_S$, and ϕ_S. The error volume $\delta V_{\rm tot}$ quoted in equation (2.14) above corresponds to (3/4th of) the volume of an ellipsoid whose semi-axes are the *marginalized* errors in spherical coordinates; the true error volume $\delta V_{\rm ell}$ is that of the ellipsoid described by the full

[7] http://cas.sdss.org/dr3/en/tools/search/sql.asp

covariance matrix. The ratio $\delta V_{\rm ell}/\delta V_{\rm tot}$ depends on the actual position angle (θ_S, ϕ_S) of the source; averaging over all angles, I find $\langle \delta V_{\rm ell}/\delta V_{\rm tot}\rangle = 0.31$ (0.20) for masses $m_1 = m_2 = 10^5 \mathrm{M}_\odot$ (10^4) at redshift $z = 1$ (7).

If *LISA* errors dominated the total redshift uncertainty $\langle \delta z^2\rangle^{1/2}$, this implies that the correlations could reduce the mean number of counterparts by a factor of 3–4. However, as discussed above, the total uncertainty is likely going to be dominated by weak lensing errors; hence the inclusion of the correlations would reduce the final error volume only by a small factor ($\sim 15\%$). I make no use of this reduction in the results I quote below.

2.4 Quasar Counterparts

To estimate the typical number of quasar counterparts to a specific SMBH merger event, I combine the size, $\delta V_{\rm co}$, of the comoving *LISA* error box with the space density of quasars, by integrating over the quasar luminosity function, $\phi(L, z)$:

$$N = b\, \delta V_{\rm co} \int_{L_{\rm min}}^{L_{\rm max}} \mathrm{d}L\, \phi(L, z), \tag{2.15}$$

where b accounts for the bias due to the clustering of quasars, and $L_{\rm min}$ and $L_{\rm max}$ are the minimum and maximum quasar luminosities which could be associated to the specific SMBH merger event. I use $L_{\rm min} = 0.1 L_{\rm Edd}$ and $L_{\rm max} = 2 L_{\rm Edd}$, where $L_{\rm Edd}$ denotes the Eddington luminosity for the total BH mass. Motivations behind this particular near-Eddington choice are further discussed below.

2.4.1 Luminosity Function of Quasars

I adopt the standard empirical double power–law fit to the quasar luminosity function of the combined quasar samples from the Two-Degree Field (2dF) and Sloan Digital Sky Survey, with pure luminosity evolution valid for $z < 2.1$ (Croom et al., 2005; Richards et al., 2005). Unfortunately, these surveys extend only to relatively bright magnitudes ($B \lesssim 21$), corresponding to the Eddington luminosity of BHs with mass $M \gtrsim 3 \times 10^7\ \mathrm{M}_\odot$ for $z = 1$, which is above *LISA*'s optimal mass–range. In order to estimate the number of quasar counterparts for lower BH masses, I extrapolate the luminosity function to the faint end.

A limitation of this luminosity function is the simple quadratic fitting formula for the evolution (Croom et al., 2005; Richards et al., 2005), which is only valid for redshifts $z < 2.1$. To avoid these difficulties Madau et al. (1999) (hereafter MHR) proposed a more complicated empirical fitting formula with three adjustable parameters z_s, ζ, and ξ. These parameters were estimated using high-z quasars, and were improved to include the high-redshift SDSS sample and weak-lensing effects (Wyithe & Loeb, 2002). I obtain a luminosity function that is more precise at lower redshifts and is concordant with the redshift scaling by fitting the MHR model to the Richards et al. (2005) luminosity function in the interval $0.5 < z < 2.1$ and keeping the high–redshift asymptote at the Wyithe & Loeb (2002) value. The result is $L^* = 5.06 \times 10^{10}\mathrm{L}_\odot$, $z_s = 1.66$, $\zeta = 2.6$, and $\xi = 2.8$. Other parameters in the luminosity function that are independent of the evolution are adopted from Richards et al. (2005): $\beta_\mathrm{l} = 1.45$, $\beta_\mathrm{h} = 3.31$, and $\Phi^*_\mathrm{L} = 1.99 \times 10^{-6}\mathrm{Mpc}^{-3}$.

2.4.2 Clustering of Quasars

The bias, b, in equation (2.15) describes the enhancement in the number of quasars around a specific quasar being the potential counterpart, relative to the value for a homogeneous distribution. The clustering depends only weakly on quasar luminosity (Adelberger & Steidel, 2005; Lidz et al., 2006). I use the observed autocorrelation function of quasars from the 2dF survey (Croom et al., 2005), $\xi(s) = (s/s_0)^\gamma$ for $s > 0.1h^{-1}\mathrm{Mpc}$ (assuming no quasars with a smaller separation), where $s_0 = 5.48h^{-1}\mathrm{Mpc}$ (5.55) and $\gamma = 1.20$ (1.63) for $s < 25\mathrm{Mpc}$ (¿25Mpc), respectively. The bias is given by the average value of $\langle 1 + \xi(t)\rangle$ over the comoving error box. Assuming that the error box is a cylinder, with height $\delta y = c\delta z/H(z)$ (which is the comoving distance along the line of sight corresponding to the redshift error) and radius $\delta r = \sqrt{\delta V_\mathrm{co}/(\pi\delta y)}$ (corresponding to the angular uncertainty of *LISA*):

$$b = \frac{\int_0^{\delta r} 2\pi r \mathrm{d}r \int_0^{\delta y} \mathrm{d}y \, (1 + \xi(\sqrt{y^2 + r^2}))}{\int_0^{\delta x} 2\pi r \mathrm{d}r \int_0^{\delta y} \mathrm{d}y}. \tag{2.16}$$

I find $b = 1.50$, 1.23, and 1.07, for my best, typical, and worst cases, respectively. The corresponding comoving cylinder heights are $\delta y = 62.5$, 62.9, and 73.8 Mpc, and the cylinder radii are $\delta r = 3.3$, 17.8 and 56.4 Mpc.

Table 2.2. Survey characteristics

Survey	$M_{\rm min}$ $(z=1)$ $M_\odot$	Limiting mag	Sky cov. deg^2	Observing
2dF[a](2QZ,6QZ)	3×10^7	$b_J < 20.85$	750	1997-2002
SDSS[b](LRG)	2×10^8	$i < 19.1$	7×10^3	1998-2005
Deep2[c]	5×10^5	$R < 24.5$	4	2002-04
AGES[d]	1×10^7	$R < 21.5$	9	2004-06
DES[e]	7×10^5	$AB < 24.7$	5×10^3	2009-13
LSST[f]	2×10^5	$AB < 26.5$	1.8×10^4	2012

[a]Two-Degree Field, see http:/www.2dfquasar.org/

[b]Sloan Digital Sky Survey, see http:/www.sdss.org/

[c]See http:/deep.berkeley.edu/

[d]AGN and Galaxy Evolution Survey, covers radio, IR, optical, and X-ray bands, see http:/cmb.as.arizona.edu/ $\sim$ eisenste/AGES/

[e]Dark Energy Survey, see http:/cosmology.astro.uiuc.edu/DES/ and http:/decam.gnal.gov/

[f]Large Synoptic Survey Telescope, see http:/www.lsst.org/

2.5 Results

The main results are presented in Figure 2.4, which shows $\langle N \rangle$, the average number of counterparts within the 3D *LISA* error volume, for various total masses M and redshifts z. Recall that I have assumed that the GW event is always accompanied by quasar activity. According to my definition, $\langle N \rangle$ then corresponds to the mean number of quasars that would be found in *LISA*'s error box, *in addition* to the quasar actually associated with the GW source. A straightforward identification of a unique counterpart therefore requires that there be no additional quasars in the error volume and that the EM observation sensitivity goes below the actual counterpart luminosity (so that the presence of fainter quasars can be ruled out). A simple criterion for a reasonable chance not to have any additional counterparts candidates is $\langle N \rangle < 1$.[8] I find that this simple condition is satisfied in the case of a "typical" event at $z = 1$ with total masses $\sim 4 \times 10^5$ $\mathrm{M}_\odot$ or $\sim 8 \times 10^6$ $\mathrm{M}_\odot$. At higher redshifts, the average number of potential counterparts will be much larger, due mostly to the increasing weak lensing errors. At $z \gtrsim 3$, even the best case events will typically have at least one additional quasar in their error box. On the other hand, the increase from $z = 3$ to $z = 5$ in the number of quasars located in the error-box is partly mitigated by the drop in the abundance of quasars at $z \gtrsim 3$. The three panels of Figure 2.4 display results for various presumptions of uncertainties. The top left panel uses raw, uncorrected weak-lensing errors and the counterpart luminosity is allowed to vary in a broad range $0.1 < L/L_{\mathrm{Edd}} < 2$. The top right panel accounts for a 20% reduction of weak-lensing errors, and the luminosity is restricted to $0.7 < L/L_{\mathrm{Edd}} < 1.3$. The bottom panel shows results for the more conservative scaling of *LISA* errors, $\delta d_{\mathrm{L}}/d_{\mathrm{L}} \propto \Delta T^{-1/2} \times SNR^{-1}$ and $\partial\Omega \propto \Delta T^{-1} \times SNR^{-2}$ if $\Delta T <$ 1yr. In all cases at $z \sim 1$, a unique counterpart may be identifiable.

One may also interpret the number of counterparts I compute, $\langle N \rangle$, together with the same simple criterion $\langle N \rangle < 1$, in a somewhat different way: as a means to *test* my hypothesis that *LISA* events are accompanied by bright quasar activity. If my hypothesis is incorrect, then the number of quasars in *LISA*'s error volume should be drawn from the random distribution of quasars on the sky, unrelated to the *LISA* event (excluding the correction due to correlations that I have included in my analysis; although I found this correction to be relatively insignificant). In many configurations, I find $\langle N \rangle \ll 1$, implying a significant probability that *no* bright quasars would be found in *LISA*'s error

[8] One could explicitly consider the probability distribution for N. For example, for a Poisson distribution, the probability for $N = 0$ would be 50/90 percent for $\langle N \rangle = 0.7/0.1$.

volume in these cases. If several *LISA* events are indeed found with no such quasar counterparts, it would, by itself, be an important new constraint on the process of binary black hole coalescence.

The identification of counterparts could be aided by a combined analysis of several GW events. Every successful identification yields a very precise direct measurement for the $L/L_{\rm Edd}$ Eddington ratio. Once a statistically significant set of Eddington ratios is acquired, the empirical distribution can be mapped. It is yet unclear whether SMBH mergers are expected to have high-luminosity quasar counterparts. Then, *in case* $L/L_{\rm Edd}$ is in a narrow range, this information can be used to greatly constrain the a priori assumptions on the counterpart's luminosity. As an example, in Figure 2.4 (middle panel) I consider $L/L_{\rm Edd} = 1 \pm 0.3$, and find $\langle N \rangle$ to decrease well under 1 in the typical case.

If cosmological uncertainties were to dominate the error budget on a counterpart's redshift, a combined analysis could further improve the robustness of the identification. Indeed, even if each GW event has, by itself, several possible counterparts, each of these counterparts would require a different set of cosmological parameters. As a result, there should be, in general, only a single set of cosmological parameters[9] that gives a consistent set of counterparts to all of the GW events (Schutz, 1986). The counterpart candidates contradicting this concordant set can be discarded. Unfortunately, the error budget is likely to be dominated by the lensing magnification uncertainty. In this case, having multiple events is going to be helpful only if a sufficient number ($\gg 100$) of events are detected to map out the full distribution of magnifications (such a large number of events is not expected; see below).

2.6 Discussion

2.6.1 Search Strategy

Different strategies for the search of an electromagnetic counterpart to a *LISA* event can be envisioned. The simplest one would be to search, in an existing survey catalog, for candidates located in the 3D *LISA* error box. I list the characteristics of several deep present and near-future surveys in Table 2.2. These surveys cover various bands

[9]This set, of course, will suffer from the usual degeneracy along the surface of constant luminosity distance $d_{\rm L}(z, \Omega_\Lambda, \Omega_m, h, w)$.

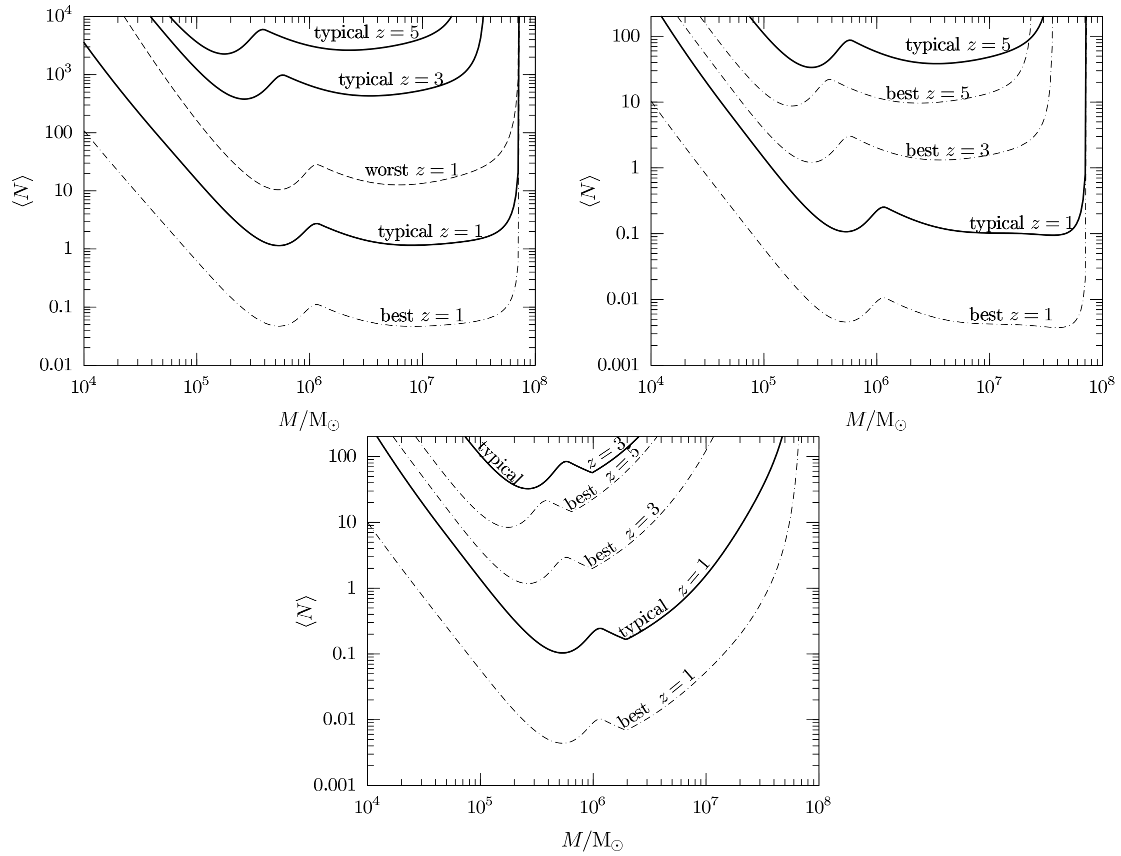

Figure 2.4 The average number of quasars in the three–dimensional *LISA* error volume. The thin dash–dotted, thick solid, and thin dashed curves trace the "best", "typical", and "worst" cases, respectively. The low–frequency noise wall for *LISA* is assumed to be at $f_{\rm min} = 0.03$mHz. *Top left*: Using raw data without any weak-lensing corrections and the counterpart's luminosity is assumed to be $0.1 < L/L_{\rm Edd} < 2$. *Top right*: The weak-lensing errors are corrected by 20%, and the luminosity is assumed to be $0.7 < L/L_{\rm Edd} < 1.3$. *Bottom*: Same as the top right panel, assuming that LISA uncertainties scale as $\delta d_{\rm L}/d_{\rm L} \propto \Delta T^{-1/2} \times SNR^{-1}$ and $\partial\Omega \propto \Delta T^{-1} \times SNR^{-2}$. In most cases at $z \lesssim 1$, a unique quasar counterpart may be identifiable.

between 400 and 1100nm. In each case, I calculate the minimum mass of the quasar corresponding to the magnitude limit of the survey, provided that the quasar is shining at the Eddington luminosity. For the quasar spectrum I use Madau et al. (1999) and follow Madau (1995) to account for the Lyman series line blanketing and photoelectric HI absorption to obtain the apparent luminosity. The portion of the sky covered and scheduled operation times are also given. The most promising (deepest and largest sky coverage) among the planned surveys is that from the LSST, scheduled for the same time as *LISA*.

A second strategy would be to design a survey specifically aimed at identifying the counterparts of well–localized *LISA* events, by observing in detail the 2D angular error box provided by *LISA* and looking for the expected counterparts. The time domain may come to play an important role in the strategy of this type of surveys. Indeed, for some of the events, one may have, from the *LISA* data-stream, a reasonably good idea of the location on the sky of the SMBH binary prior to coalescence. For instance, Holz & Hughes (2005) estimate that this knowledge may be available with reasonable accuracy about a day in advance. One would then be able to monitor any unusual photometric variability associated with the violent SMBH merger in this area somewhat before, during and after the coalescence. Surveying the area long (i.e. months or years) after the coalescence may also prove useful in discovering the counterpart and/or monitoring the viscous evolution of any gas surrounding the SMBH merger remnant (Milosavljevic & Phinney, 2005). The time domain may thus greatly facilitate the identification of a unique electromagnetic counterpart to some *LISA* events, even in cases when many counterpart candidates otherwise exist in the 3D error box.

2.6.2 Uncertainties in the Analysis

Throughout the analysis of *LISA* uncertainties, I focused on equal mass binaries. With this simplifying assumption, it was possible to derive approximate scalings as a function of total mass and relate them to the calculations of Vecchio (2004) for $m_1 = m_2 = 10^6 M_\odot$. I also find good agreement with the recent calculations of Holz & Hughes (2005) for a variety of equal-mass combinations. For unequal masses, the GW signal-power depends to leading order on the simple combination $\mathcal{M} = \mu^{3/5} M^{2/5}$, allowing a straightforward extension of my scaling arguments to more general mass ratios.

As mentioned above, my results depend on the *LISA* sensitivity curve at low frequencies. In particular, the relationship between the arrival frequency $f_{\rm a}(M_z, \Delta T)$, the final frequency $f_{\rm isco}(M_z)$, and the *LISA* minimum frequency noise wall $f_{\rm min}$ determines the maximum possible observation time for the in-spiral. The exact value of $f_{\rm min}$ is currently assumed to lie between 0.1 and 0.03mHz. Figure 2.4 assumes $f_{\rm min} = 0.03$mHz. In this case, at $z = 1$, a $\Delta T = 1$yr observation of the in-spiral phase is possible for $M < 2 \times 10^6 {\rm M}_\odot$ but for larger masses, the maximum possible observation time becomes shorter than a year. I have also computed the number of quasars in the 3D *LISA* error box for the higher value of $f_{\rm min} = 0.1$mHz. I find a significant increase in this number at the high–mass end (i.e. for $M \sim 10^7 {\rm M}_\odot$), but the results are essentially unaffected for lower mass SMBHs.

An important assumption in my analysis is the near-Eddington luminosity of the quasar counterparts associated with *LISA* events. While this assumption is difficult to justify from first principles, it is the luminosity expected if SMBH accretion occurs in a regime which is not supply-limited. Observationally, the Eddington ratio of quasars, $L/L_{\rm Edd}$, can be inferred, leading to values from 0.1 to $\gtrsim 1$, with higher values at large redshifts (e.g. Kaspi et al. 2000; Vestergaard 2004; Woo & Urry 2002). This ratio has been determined for a handful of lower mass SMBHs in AGNs and these sources have been found to cluster around $L/L_{\rm Edd} \sim 1$ as well (Greene & Ho, 2004). Recent work by Kollmeier et al. (2006) and Hopkins et al. (2006) both suggest $L/L_{\rm Edd}$ is typically around 1/3.

The restricted luminosity range $0.1 < L/L_{\rm Edd} < 2$ assumed in this analysis effectively serves as a 4th ("brightness") dimension, complementing the three-dimensional geometrical error volume provided by *LISA*. According to Table 2.1, for a given event, the mass estimate provided by *LISA* is typically very accurate. Therefore, it is through the range of acceptable Eddington ratios that the integration bounds in equation (2.15) change. Since the luminosity function decreases rapidly with L, the integral is dominated by the lower bound and is largely independent of $L_{\rm max}$. I chose $L_{\rm max} = 2L_{\rm Edd}$ for concreteness. When modifying the lower bound from $L_{\rm min} = 0.1L_{\rm Edd}$ to $L_{\rm min} = 1.0L_{\rm Edd}$ or $L_{\rm min} = 0.01L_{\rm Edd}$, for instance, I find that the number of quasars present in the 3D *LISA* error box changes by a factor of 0.1 and 5, respectively.[10] Obviously, our need to extrapolate the quasar luminosity function below the minimum value constrained by the observations is an additional important source of uncertainty in this analysis, but one that will be addressed well by future generations of surveys (Table 2.2).

In a recent study, Hennawi et al. (2006) have found a large number of small separa-

[10]The change is explained by the asymptotic form of the luminosity function $\Phi(L) \propto L^{-1.45}$ for low L.

tion quasars, implying an order-of-magnitude increase in the quasar auto-correlation on scales $\lesssim 200h^{-1}$ kpc. However, the dimensions of the error volume as I estimated it is generally much larger ($\sim$3.3 Mpc even in the best case). As a result, the average number of counterparts is changed by a negligible factor by this small–scale auto-correlation: 8.3×10^{-3}, 3.7×10^{-4}, and 3.3×10^{-5} in the best, typical, and worst case *LISA* errors. Increasing the correlation by an order of magnitude out to a scale of $500h^{-1}$ kpc would still cause at most a 6% increase in the mean number of quasars in the best case. Hennawi et al. (2006) do not find an increase in the correlation beyond $\sim 500h^{-1}$ kpc scales. I note that our inability to identify the correct counterpart from among any rare ultra-small-separation candidates would not degrade cosmological parameter estimations significantly. One may also argue that such close–separation binary quasars would better represent a 'precursor' stage in the evolution of the two black holes towards an eventual coalescence. If so, one would not expect them to be associated with GW events, and they may in fact be anti–correlated with such events.

In this work, I have focused on optical quasars as plausible counterparts to GW events. It would be interesting to repeat my analysis using other types of "electromagnetic objects" that may be associated with SMBH coalescences. For example, even if gas accretion leads to prodigious energy output in radiation, the optical light of the quasar may be obscured by the intervening gas and dust near the galactic nucleus. In these cases, the GW events may be more commonly associated with X–ray quasars (e.g. Milosavljevic & Phinney 2005), or with ultraluminous infrared galaxies (e.g. Thompson et al. 2005). As these sources are also relatively rare, unique counterparts may be identifiable if such objects typically accompany GW events.

2.6.3 Implications: Black Hole Astrophysics

A successful identification of a quasar counterpart to a *LISA* event would provide powerful diagnostics on the physics of SMBH gaseous accretion and the associated radiation. The masses and spins of the two BHs before merger can be directly determined from the GW signal, from which the mass and spin of the remnant BH follows at some precision. In some cases (e.g. Hughes & Menou 2005), the remnant BH could also be observed by *LISA* during the post-merger ring-down phase, which would constrain its mass and spin directly. The orientation of the orbital plane of the BH binary before merger would be measured as well. All of these parameters are generally unknown for quasars detected only via traditional electromagnetic techniques.

The observation and monitoring of quasar counterparts to *LISA* events may thus offer us some of the best laboratories for the study of AGN physics. First, the Eddington ratio can be measured to high accuracy (limited only by photometric errors and bolometric corrections), since *LISA* estimates for the BH masses are extremely precise by astronomical standards (see Table 2.1). Second, if the quasar accretes at or near the Eddington limit, given its Eddington ratio, one may be able to set a useful lower limit on the radiative efficiency of its accretion flow. If it is in excess of the canonical 10% value, it will provide an interesting empirical test of the physics of accretion onto a spinning BH, with a spin directly constrained by the GW measurement. Third, the counterpart could be monitored for years following the merger to follow the viscous evolution of the gaseous disk and thus clarify its role in the SMBH coalescence process. Fourth, it is expected that the gas disk will be forced in the orbital plane of the pre-merger binary by the Bardeen-Peterson effect (Milosavljevic & Phinney, 2005). Knowing the disk orientation could thus offer tests of the geometry of quasar emission and obscuration (even after the merger, given the expected spin of the remnant). It may also be possible to further develop diagnostics related to the geometry of a jet, if present.

2.6.4 Implications: Cosmology

The successful identification of an EM counterpart to a GW event could, in principle, open the way to use them as "standard sirens" to probe the background cosmology (Schutz, 1986), analogously to the Ia SNe standard candles (Holz & Hughes, 2005). The precision on the cosmological model can, however, be improved only if the $d_{\rm L}(z)$ function is determined to a higher accuracy than it can be already guessed from other data that exists when *LISA* is operational. As an example, I have assumed here to have available the uncertainty from the combined datasets from two future projects, *Planck* and LSST. I have found that the major obstacle against a dramatic improvement on cosmology is the gravitational lensing of intervening matter along the line of sight to a *LISA* source. In the weak-lensing limit, the r.m.s. magnification of a source at $z = 2$ is 12%, leading to a luminosity distance error of 6%. Dalal et al. (2003) have shown that galaxy shear maps can be used to correct weak-lensing distortion, but only a 20% relative improvement can be achieved, so that $\delta d_{\rm L}/d_{\rm L} = 5\%$. I suggest alternatively that correcting for the contribution of the known distribution of intervening matter might improve weak lensing uncertainties by another 20%. Furthermore, the weak lensing uncertainty can be overcome if a large sample of sources is available when fitting $d_{\rm L}(z)$, mapping out the magnification distribution. Using a number K of merger events along with uniquely identified counterparts, the lensing error reduces approximately as $1/\sqrt{K}$ (although the actual improvement will be less pronounced, due to a non-Gaussian tail of high magnifications; Holz & Linder 2005; Wang et al. 2002). To reach the *Planck* + LSST level of $\delta d_{\rm L}/d_{\rm L} = 10^{-3}$, I find that $K > 100$ events would be required.

Is such a large number of merger events, with uniquely determined electromagnetic counterparts, expected from the *LISA* data-stream? Monte-Carlo simulations of SMBH merger trees generally indicate *LISA* event rates from ~ 20–$0.5\mathrm{yr}^{-1}$ for masses $M_{\rm BH} \lesssim 10^7$ at $z \sim 1$ (Menou et al., 2001; Micic et al., 2007; Sesana et al., 2004, 2007). Detecting a total of $K = 100$ would be barely possible during a 3-year *LISA* mission lifetime, only allowing a marginal test of the concordance of cosmological parameters with standard sirens. In addition, most of these events may be expected to involve SMBHs at the low–mass end (i.e. $\lesssim 10^5\mathrm{M}_\odot$; Menou 2003; Sesana et al. 2004), which are not ideal for unique counterpart identifications (see Figure 2.4). However, large uncertainties remain on the expected event rate. For example, Islam et al. (2004) predict much larger rates, which could open up the possibility of a statistical analysis, folding in the expected weak lensing magnification distribution.

2.7 Conclusions

In this work, I have considered the possibility that SMBH-SMBH mergers, detected as gravitational wave sources by *LISA*, are accompanied by gas accretion and quasar activity with a luminosity approaching the Eddington limit. Under this assumption, I have computed the number of quasar counterparts that would be found in the three–dimensional error volume provided by *LISA* for a given GW event. I found that weak lensing errors exceed other sources of uncertainties on the inferred redshift of the electromagnetic counterpart and increase the effective error volume by nearly an order of magnitude. Nevertheless, I found that for mergers between $\sim (4 \times 10^5 - 10^7)\mathrm{M}_\odot$ SMBHs at $z \sim 1$, the error box may contain a single quasar with a B-band luminosity $L_B \sim (10^{10} - 10^{11})\mathrm{L}_\odot$. This would make the identification of unique electromagnetic counterparts feasible, allowing precise determinations of the Eddington ratio of distant accreting SMBHs, and providing an alternative method to constrain cosmological parameters.

Chapter 3

Pre-Merger Localization of Gravitational-Wave Standard Sirens

3.1 Introduction

One of the key objectives of the planned, low-frequency gravitational-wave (GW) detector LISA (Laser Interferometric Space Antenna) is the detection of supermassive black hole (SMBH) binary mergers at cosmological distances. The observation of these chirping GW sources would deepen our understanding of (i) general relativity, e.g. by offering unique tests of spacetime physics in the vicinity of SMBHs (Arun, 2006; Berti et al., 2006; Dreyer et al., 2004; Hughes & Menou, 2005; Miller, 2004), (ii) cosmology, by providing additional constraints on the luminosity distance–redshift relation (Holz & Hughes, 2005; Hughes, 2002a; Schutz, 1986), (iii) large-scale structure, by indirectly constraining hierarchical structure formation scenarios (Barnes & Hernquist, 1992; Begelman et al., 1980; Berti et al., 2005b; Menou et al., 2001), and (iv) black hole astrophysics (Dotti et al., 2006; Kocsis et al., 2006; Milosavljevic & Phinney, 2005), e.g. by allowing accurate determinations of Eddington ratios and other attributes of black hole accretion, in systems with SMBH mass and spin known independently from the GW measurements.

From a purely astronomical point of view, one of the most attractive features of the LISA mission design is the possibility to constrain the 3-dimensional location (i.e. sky position and distance) of GW inspiral sources to within a small enough volume that the identification of potential electromagnetic (EM) counterparts to SMBH merger events can be contemplated seriously. Indeed, the accuracy of such LISA localizations at merger are encouraging, with an error volume $\delta\Omega \times \delta z = 0.3\,\mathrm{deg}^2 \times 0.1$ for SMBH masses $m_1 = m_2 = 10^6 \mathrm{M}_\odot$ at $z = 1$, for instance (Vecchio, 2004). In Kocsis et al. (2006), I have shown that this accuracy may be sufficient to allow an unique identification of the bright quasar activity that may be associated with any such SMBH merger.

Another possibility, examined here in detail, is to monitor the sky for EM counterparts in real time, as the SMBH inspiral proceeds. This is arguably one of the most efficient ways to identify reliably (prompt) EM counterparts to SMBH merger events, since the exact nature of such counterparts is a priori unknown. Using the GW inspiral signal accumulated up to some look–back time, t_{f}, preceding the final coalescence, one already has a partial knowledge of where the source of GWs is located on the sky. Since the sky position is deduced primarily from the detector's motion around the Sun, one anticipates that angular positioning uncertainties will not change too dramatically during the last few days before merger, so that a targeted EM observation of the final stages of inspiral may be a feasible task. Here, I present an in-depth study of the potential for such pre-merger localizations with LISA, while I discuss various astrophysical concepts and observational strategies for EM counterpart identifications in a companion work (Kocsis et al., 2007).

The main purpose of the present analysis is thus to determine the accuracy of SMBH inspiral localizations with LISA, as a function of look–back time, t_{f}, prior to merger. The LISA detector is not uniformly sensitive to sources with different sky positions and angular momentum orientations. Results will thus generally depend on the fiducial values of these angles. My first objective is to calculate the time-dependence of distributions of localization errors, for randomly oriented sources, over a large range of values for the SMBH masses and source redshift. A second objective of my analysis is to estimate source parameter dependencies for these distributions of localization errors, i.e. how the 3-dimensional (sky position and distance) localization error distributions depend on the fiducial sky position of GW sources. This is useful to understand which regions of the sky may be best suited for the identification of EM counterparts to SMBH merger events. To the best of my knowledge, this angle dependence has not been explored in detail before, not even in terms of final errors at ISCO (i.e. at $t_{\mathrm{f}} = t_{\mathrm{isco}}$, when using the complete inspiral data-stream, up to the innermost stable circular orbit, or ISCO).

Parameter estimation uncertainties for LISA inspirals have been considered previously, under a variety of approximations (Cutler, 1998; Moore & Hellings, 2002; Hughes, 2002a; Barack & Cutler, 2004b; Vecchio, 2004; Berti et al., 2005b; Holz & Hughes, 2005; Arun, 2006; Lang & Hughes, 2006). These studies differ in the levels of approximation adopted for the GW waveform, using various orders of the post-Newtonian expansion. The LISA signal output for these waveforms are obtained through a linear combination of the two GW polarizations, $h_+(t)$ and $h_\times(t)$, with the beam pattern functions, F_+ and $F_\times$. The beam patterns define the detector sensitivity for the two polarizations. They are determined by the angles describing the instantaneous orientation of the LISA constellation relative to the GW polarizations. As the LISA detector constellation orbits the Sun, with a one year period, F_+ and $F_\times$ are slowly changing in time and this introduces an additional time dependence in the LISA signal. As first shown by Cutler (1998), the source sky position can be determined with LISA using this modulation. In the formalism given by Cutler (1998), this modulation couples time and angular dependencies in a complicated way, making the estimation of localization errors numerically costly for a large set of SMBH binary random orientations and parameters.

Using a different approach, Cornish & Rubbo (2003) have derived the orbital modulation in a much simpler form, in which the angular parameter dependence and the time dependence can be decoupled. Here, starting directly from the original Cutler (1998) expression, I give an independent derivation of the Cornish & Rubbo (2003) formula and write it in an equivalent form, from which decoupling is more evident. I do this by expanding the LISA response function into a discrete Fourier sum of harmonics of the fundamental frequency of LISA's orbital motion, $f_\oplus = 1\mathrm{yr}^{-1}$. Since LISA's orbit does not include high frequency features, I expect this sum to be quickly convergent. In fact, it is clear from the Cornish & Rubbo (2003) result that the expansion terminates at $4f_\oplus$ and that there are no higher order harmonics due to the detector's motion. The series coefficients in the expansion are independent of time and only depend on the relative angles at ISCO. I then develop a Fisher matrix formalism in which parameter error distributions can be mapped independently of time, while the time dependence can be computed independently of the specific SMBH binary orbital elements. A Monte Carlo simulation for random binary orientations then becomes a simple linear combination, without any integral evaluations. This greatly reduces the numerical cost of estimating parameter uncertainty distributions, even at fixed observation time (e.g. to map distributions of errors at ISCO). I use this numerical cost advantage

1. to map the distribution of localization errors for the full three dimensional grid of SMBH total mass ($M = 10^5$–$10^8 \mathrm{M}_\odot$), redshift ($z = 0.1$–7) and arbitrary look–back time (t_f) before merger,

2. to study how source localization error distributions vary systematically with sky

position, and

3. to discuss implications, in terms of advance warning times, for prompt electromagnetic counterpart searches with large field-of-view astronomical instruments.

I call this new approach the harmonic mode decomposition (HMD). The method verifies that the amplitude modulation, which is restricted to frequencies less than $4f_\oplus = 1.3 \times 10^{-7}$Hz, is indeed a very slow modulation when compared to the GW frequency of LISA SMBH inspirals (0.03mHz–1Hz). One plausibly expects that physical parameters which determine the amplitude modulation (like the source sky position and orbital inclination relative to the detector) can be estimated independently of the parameters which determine the GW frequency (like masses, orbital phase, time to ISCO). In the HMD method, the two sets of parameters are naturally separated and can be estimated independently. In particular, parameters related to the modulation can essentially be determined on a background of GW-cycle averaged signal. In the present work, I compute LISA inspiral localization errors with the approximation that high frequency signal parameters have strictly no cross-correlations with parameters related to the slow orbital modulation. In addition to the numerical advantages mentioned above, the HMD formalism offers a clear interpretation of the time evolution of uncertainties for the slow modulation parameters. This can be used to gain a better understanding of the general evolutionary properties of localization errors. The following questions, that I address in detail in this work, are particularly relevant.

(i) Under what conditions do the localization uncertainties scale simply with the measured signal–to–noise ratio, and how do these uncertainties evolve during the final stages of inspiral?

(ii) To what extent do the high and low frequency signal parameters decouple?

(iii) What are the best determined combinations of the angular parameters?

(iv) How and why does the shape of the 3D localization error ellipsoid change during the final week(s) of observation?

In this analysis, I neglect the "Doppler phase" due to LISA's orbital motion, SMBH spin precession effects and any finite SMBH binary orbital eccentricities. These approximations are advantageous for the resulting simplicity, but the use of the HMD method is not restricted to these approximations. I also outline a generalized HMD method which remains numerically much more efficient than standard methods. I leave a numerical implementation of this general HMD method to future work. It will be particularly interesting to determine how my approximate results for the evolution of LISA localization errors are modified when spin precession effects are included, since spin precession effects were shown to improve the final localization errors by factors of 3–5 at ISCO (Lang & Hughes, 2006; Vecchio, 2004).

The remainder of this paper is organized as follows. In § 3.2 I define the conventions and the assumptions made in this analysis. In § 3.3 I expand the LISA GW signal in Fourier modes and obtain the conversion from actual physical parameters to corresponding Fourier amplitudes. In § 3.4, I incorporate these results into a Fisher matrix formalism and derive the expressions necessary to estimate correlation errors for HMD signals. In § 3.5, I present results from Monte Carlo computations of the time evolution of localization errors and discuss results in terms of advance warning times for prompt electromagnetic counterpart searches. In § 3.6, I develop toy models to interpret the time-dependence of LISA localization errors and to answer questions (i)–(iv) above. I summarize the results and conclude in § 3.7.

3.2 Assumptions and Conventions

This section is divided into three parts. First, I list the definitions of physical quantities used in this paper, in particular the variables describing a SMBH inspiral. Second, I give the equations which determine the LISA inspiral signal. Third, I state all the assumptions made in this work.

3.2.1 Definitions

In general, an SMBH inspiral is described by a total of 17 parameters. These include 2 redshifted mass parameters, $(\mathcal{M}_z, \eta_z)$, 6 parameters related to the BH spin vectors, $\boldsymbol{p}_{\rm spin}$, the orbital eccentricity, e, the source luminosity distance, $d_{\rm L}$, 2 angles locating the source in the sky, (θ_N, ϕ_N), 2 angles that describe the relative orientation of the binary orbit, (θ_{NL}, ϕ_{NL}), a reference time, $t_{\rm merger}$, and a reference phase at ISCO, $\phi_{\rm ISCO}$, and the orbital phase, $\phi_{\rm orb}$. Throughout this work, I restrict ourselves to circular orbits by omitting the orbital eccentricity, e, and instead of the orbital phase, $\phi_{\rm orb}$, I use the look–back time before merger, t, as my evolutionary time parameter. The LISA signal for a

GW inspiral is determined by the above set of parameters and two additional angular parameters describing the orientation of LISA, (Ξ, Φ). I elaborate on the definitions of my mass and angular parameters below.

Mass Parameters

For component masses m_1 and m_2, the total mass is $M = m_1 + m_2$, the reduced mass is $\mu = m_1 m_2/M$, the symmetric mass ratio is $\eta = \mu/M$ and the chirp mass is defined as $\mathcal{M} = M\eta^{3/5}$ (Misner et al., 1973). Throughout this work, I use geometrical units: $\mathrm{G} \equiv \mathrm{c} \equiv 1$. In this case, the mass can be expressed in units of time: $10^6 \mathrm{M}_\odot \equiv 4.95\,\mathrm{sec}$. The measured GW waveforms are insensitive to the cosmological parameters, if they are expressed in terms of the luminosity distance and the redshifted mass parameters, e.g. $m_z = (1+z)m$ (same for redshifted chirp and reduced masses).

Time Parameters

I write a generic look–back time (or "observation time") before merger as t, and a generic redshifted GW frequency (or "observation frequency") as f[1]. I use the leading order (i.e. Newtonian) approximation for the frequency evolution. Therefore, the observed frequency at look–back time t before merger is (e.g. eq. 3.3 in Poisson & Will, 1995)

$$f_0(\mathcal{M}_z, t) = \frac{5^{3/8}}{8\pi} t^{-3/8} \mathcal{M}_z^{-5/8} = 2.7 \times 10^{-4}\mathrm{Hz} \left(\frac{t}{\mathrm{day}}\right)^{-3/8} \eta_{0.25}^{-3/8} M_{6z}^{-5/8}, \tag{3.1}$$

or equivalently

$$t_0(\mathcal{M}_z, f) = 5(8\pi f)^{-8/3} \mathcal{M}_z^{-5/3} = 6.7\,\mathrm{min} \left(\frac{f}{f_c}\right)^{-8/3} \eta_{0.25}^{-1} M_{6z}^{-5/3}, \tag{3.2}$$

where M_{6z} is the redshifted total mass in units of $4 \times 10^6 \mathrm{M}_\odot$, $\eta_{0.25} = \eta/0.25$ is the symmetric mass ratio ($\eta_{0.25} = 1$ for equal component masses, § 3.2.3), $f_c = \mathrm{c}/\mathrm{R}_\oplus = c/(1\,\mathrm{AU}) = 2.00\mathrm{mHz}$ is the inverse light-travel time across the radius of the LISA orbit, and the null index stands for the order of approximation. The inspiral phase extends

[1]Note that, contrary to my convention for redshifted mass parameters, I drop the z index for f and t because I never consider comoving frequencies or times.

until the innermost stable circular orbit (ISCO), at $6M$, is reached

$$f \leq f_{\rm ISCO} = 6^{-3/2}\pi^{-1}M_z^{-1} = 1.1{\rm mHz} \times M_{6z}^{-1}, \tag{3.3}$$
$$t \geq t_{\rm ISCO} = 5(3/2)^4\eta^{-1}M_z = 33\,{\rm min} \times \eta_{0.25}^{-1}M_{6z}. \tag{3.4}$$

where $t_{\rm ISCO}$ is the (observer-frame) look–back time before merger corresponding to the ISCO, and $f_{\rm ISCO}$ is the (observer-frame) frequency at ISCO.

In the present work, I fix the start of the observation (i.e. when the source first enters LISA's frequency band) at look–back time $t_{\rm i}$, and examine how the value of an end-of-observation time, $t_{\rm f}$, prior to merger affects the precision on source localization. I restrict ourselves to pre-ISCO inspiral signals, corresponding to $t_{\rm f} \geq t_{\rm ISCO}$. Note that any instantaneous look–back time t associated with an observation lasting from look–back times $t_{\rm i}$ to $t_{\rm f}$ must obey $t_{\rm ISCO} \leq t_{\rm f} \leq t \leq t_{\rm i}$ in my notation.

Angular Parameters

LISA is an equilateral triangle-shaped interferometer with an arm-length of 5×10^6 km, orbiting around the Sun. The constellation trails 20° behind the Earth and is tilted 60° relative to the ecliptic. The detector plane precesses around the orbital axis with the same one-year period as the orbital period (Danzmann & Rüdiger, 2003).

Following Cutler (1998) and Vecchio (2004) closely, including in notation, I define two coordinate systems. The barycentric frame is tied to the ecliptic, with $\hat{\mathbf{x}}, \hat{\mathbf{y}}$ lying in the ecliptic plane and $\hat{\mathbf{z}}$ normal to it. The detector reference frame tied to the detector, with $\hat{\mathbf{z}}'$ normal to the detector plane, while $\hat{\mathbf{x}}', \hat{\mathbf{y}}'$ are in the plane and co-rotating with the detector so that the arms are described by time-independent vectors. I refer to the barycentric frame with normal coordinates and to the detector frame with primed coordinates. The unit vectors defining the source location on the sky, $\hat{\mathbf{N}}$, and the SMBH binary orbital angular momentum, $\hat{\mathbf{L}}$, are described by polar angles (θ_N, ϕ_N) and (θ_L, ϕ_L) in the ecliptic frame, (θ'_N, ϕ'_N) and (θ'_L, ϕ'_L) in the detector frame:

$$\hat{\mathbf{N}}(\theta_N, \phi_N) = \hat{\mathbf{z}}\cos\theta_N + \hat{\mathbf{x}}\sin\theta_N\cos\phi_N + \hat{\mathbf{y}}\sin\theta_N\sin\phi_N, \tag{3.5}$$
$$\hat{\mathbf{L}}(\theta_L, \phi_L) = \hat{\mathbf{z}}\cos\theta_L + \hat{\mathbf{x}}\sin\theta_L\cos\phi_L + \hat{\mathbf{y}}\sin\theta_L\sin\phi_L. \tag{3.6}$$

Since I assume no SMBH spins, orbital angular momentum is conserved and the θ_N, ϕ_N, θ_L, and ϕ_L coordinates are time-independent properties of the sources.

Let (Ξ, Φ) be the two angles specifying the orientation of the LISA system in the ecliptic: Φ describes its orbital phase during its motion around the Sun, while Ξ describes the rotation of the triangle around its geometrical center. If their values at merger are written Ξ_0 and Φ_0, then at an arbitrary look–back time t:

$$\Xi(t) = \Xi_0 - \omega_\oplus t, \tag{3.7}$$

$$\Phi(t) = \Phi_0 - \omega_\oplus t, \tag{3.8}$$

where $\omega_\oplus \equiv 2\pi/\mathrm{yr}$ is the orbital angular velocity around the Sun.

The time dependence of the detector normal vector $\hat{\mathbf{z}}'$ can be expressed as

$$\hat{\mathbf{z}}' = \frac{1}{2}\hat{\mathbf{z}} - \frac{\sqrt{3}}{2}\hat{\mathbf{x}}\cos\Phi - \frac{\sqrt{3}}{2}\hat{\mathbf{y}}\sin\Phi. \tag{3.9}$$

The detector angles are given by

$$\cos\theta'_N = \frac{1}{2}\cos\theta_N - \frac{\sqrt{3}}{2}\sin\theta_N\cos(\Phi - \phi_N), \tag{3.10}$$

$$\phi'_N = \Xi + \tan^{-1}\left[\frac{\frac{\sqrt{3}}{2}\cos\theta_N + \frac{1}{2}\sin\theta_N\sin(\Phi-\phi_N)}{\sin\theta_N\sin(\Phi-\phi_N)}\right]. \tag{3.11}$$

Let us also define ψ', the *polarization angle* of the GW waveform, as (Vecchio, 2004)

$$\tan\psi' = \frac{\hat{\mathbf{L}}\cdot\hat{\mathbf{z}}' - (\hat{\mathbf{L}}\cdot\hat{\mathbf{N}})(\hat{\mathbf{z}}'\cdot\hat{\mathbf{N}})}{\hat{\mathbf{N}}\cdot(\hat{\mathbf{L}}\times\hat{\mathbf{z}}')}. \tag{3.12}$$

Note that there are only 6 independent angular parameters $(\theta_N, \phi_N, \theta_L, \phi_L, \Xi, \Phi)$. Other detector specific quantities like θ'_N, ϕ'_N, θ'_L, ϕ'_L, and ψ' can be expressed in terms of these 6 independent parameters using eqs. (3.5–3.12).

Let us introduce a new set of 6 independent angles,

$$\Omega = (\theta_N, \phi_N, \theta_{NL}, \phi_{NL}, \alpha, \gamma), \tag{3.13}$$

with the following definitions:

- θ_{NL} is the relative latitude of $\hat{\mathbf{L}}$ and $\hat{\mathbf{N}}$ (i.e. the inclination of the binary orbit to the line of sight),
- ϕ_{NL} is the relative longitude of $\hat{\mathbf{L}}$ and $\hat{\mathbf{N}}$,

- $\alpha \equiv \Xi - \Phi + \phi_N - \frac{3\pi}{4}$,

- $\gamma(t) \equiv \Phi(t) - \phi_N$.

The explicit definitions are given in Appendix A.2.

Let us refer to the angles at the reference time $t = t_{\rm merger} = 0$ as $\Omega(0)$. Although $\Phi \equiv \Phi(t)$ and $\Xi \equiv \Xi(t)$ are time-dependent, as given by (3.7,3.8) α is a time-independent combination, unlike the time-dependent $\gamma \equiv \gamma(t)$. The angles at $t = 0$ are thus given by $\Omega(0) = (\theta_N, \phi_N, \theta_{NL}, \phi_{NL}, \alpha, \gamma_0)$.

These angles have the interesting property that they possess isotropic *a priori* distributions, like the original $\Omega(0)$ variables, but the measured GW waveforms expressed in terms of these new variables are much simpler than when they are expressed in terms of the original set eqs. (3.5–3.12).

Two additional quantities which are useful to describe the sensitivity of the detector in various directions are the antenna beam patterns (Cutler, 1998):

$$F_{\times,+}(\Omega) = \frac{1+\cos^2\theta'_N}{2}\cos 2\phi'_N \cos 2\psi'_N \pm \cos\theta'_N \sin 2\phi'_N \sin 2\psi'_N, \tag{3.14}$$

where the sign $\pm$ is defined to be positive for $F_\times$, and negative for F_+. Equation (3.14) and the transformation rules eqs. (3.5–3.12) define the time evolution of the antenna beam patterns for a given set of final angles $\Omega(0)$ as the LISA system orbits around the Sun. Note that the LISA system is equivalent to two independent orthogonal-arm interferometers which are rotated by 45° relative to each other (Cutler, 1998). Both data-streams are given by the same equations (see eq. [3.21] below), modulo a change of one of the angles for the second detector: ${\phi'}^{\rm II}_N = {\phi'}^{\rm I}_N - \pi/4$ (or equivalently $\alpha^{\rm II} = \alpha^{\rm I} - \pi/4$ using my time-independent angular variables). Thanks to this simple relationship between the two data-streams, it is possible to carry out all the calculations for the first data-stream, and later include the second data-stream in the final expression by varying the fiducial angle α.

Grouping the Parameters

I group the most important parameters describing the inspiral as follows:

$$\begin{aligned} \boldsymbol{p}_{\rm slow} &\equiv \{d_{\rm L}, \Omega\}, && (3.15)\\ \boldsymbol{p}_{\rm fast} &\equiv \{\mathcal{M}_z, \mu_z, t_{\rm merger}, \phi_{\rm ISCO}\}, && (3.16)\\ \boldsymbol{p}_{\rm spin} &\equiv \{2 \text{ spin magnitudes}, 4 \text{ spin angles}\}. && (3.17)\end{aligned}$$

This organization of parameters has fundamental importance in my formalism. As I show in § 3.2.2, the parameters $\boldsymbol{p}_{\rm fast}$ and $\boldsymbol{p}_{\rm spin}$ relate to the high frequency GW signal, while the parameters $\boldsymbol{p}_{\rm slow}$ relate to the distinctly slow orbital modulation.

3.2.2 LISA Inspiral Signal Waveform

For a circular binary inspiral, the two polarizations of GW signal are well approximated by the restricted post-Newtonian expressions

$$\begin{aligned} h_+(t) &= 2\frac{\mathcal{M}^{5/3}(\pi f)^{2/3}}{d_{\rm L}}(1+\cos^2\theta_{NL})\cos\phi_{\rm GW}(t), && (3.18)\\ h_\times(t) &= -4\frac{\mathcal{M}^{5/3}(\pi f)^{2/3}}{d_{\rm L}}\cos\theta_{NL}\sin\phi_{\rm GW}(t). && (3.19)\end{aligned}$$

The GW phase $\phi_{\rm GW}(t) \equiv \phi_{\rm GW}(\boldsymbol{p}_{\rm fast}, \boldsymbol{p}_{\rm spin}; t)$, which is twice the orbital phase , $\phi(t) = 2\phi_{\rm orb}(t)$, can be expanded into the series

$$\begin{aligned} \phi_{\rm GW}(\boldsymbol{p}_{\rm fast}, \boldsymbol{p}_{\rm spin}; t) \approx& \phi_{\rm ISCO} + \phi_0(\mathcal{M}_z; t) + \phi_1(\mathcal{M}_z, \mu_z; t)\\ &+ \phi_2(\mathcal{M}_z, \mu_z, \boldsymbol{p}_{\rm spin}; t) + \ldots, \qquad (3.20)\end{aligned}$$

where $\phi_0(\mathcal{M}_z; t)$ is the leading order Newtonian solution to the phase evolution, successive terms correspond to small general relativistic corrections, $\phi_{\rm ISCO}$ is the reference phase at ISCO and $\phi_n(t_{\rm ISCO}) = 0$ for all $n \geq 0$. The instantaneous GW frequency is defined as the time derivative of the GW phase (3.20), i.e. $f = f(t) \equiv {\rm d}\phi_{\rm GW}/{\rm d}t$, which changes very slowly compared to the GW phase itself, $\phi_{\rm GW}(t)$. In practice I use the Newtonian approximation (3.1), $f_0(t) = {\rm d}\phi_0/{\rm d}t$. Note that equation (3.20) depends implicitly on the reference time, $t_{\rm merger}$, since my time variable t is the look–back time before $t_{\rm merger}$ (see § 3.2.1)

The signal measured by LISA is a linear combination of the two polarizations (3.18), weighted by the antenna beam patterns $F_{+}^{\mathrm{I,II}}$ and $F_{\times}^{\mathrm{I,II}}$ for each of the two equivalent interferometers, defined by (3.14), resulting in the two observable data–streams

$$h^{\mathrm{I,II}}(t) = \frac{\sqrt{3}}{2}[F_{+}^{\mathrm{I,II}}h_{+}(t) + F_{\times}^{\mathrm{I,II}}h_{\times}(t)], \tag{3.21}$$

where the factor $\sqrt{3}/2 = \sin(60^{\circ})$ comes from the opening angle of the LISA arms. The beam patterns are determined by the relative orientation of the source polarizations and the detector. Their time-dependence is due to the following three main effects: LISA changes its orientation as it orbits the Sun, LISA changes its relative distance to the source as it orbits the Sun, and the orbital plane of the SMBH binary can precess because of spin-orbit coupling effects. Substituting (3.18) in (3.21) and expressing it in complex form, I get

$$h^{\mathrm{I,II}}(t) = \frac{\mathcal{A}(\mathcal{M}_z, f)}{d_{\mathrm{L}}}G^{\mathrm{I,II}}(\Omega, f)e^{i\phi_{\mathrm{GW}}(\boldsymbol{p}_{\mathrm{fast}},\boldsymbol{p}_{\mathrm{spin}};t)}, \tag{3.22}$$

where $\mathcal{A}(\mathcal{M}_z, f)/d_{\mathrm{L}}$ defines the overall amplitude scale, with

$$\mathcal{A}(\mathcal{M}_z, f) = 2\sqrt{3}(\pi f)^{2/3}\mathcal{M}_z^{5/3}. \tag{3.23}$$

The $G(\Omega, f)$ factor defines the angular dependence of the signal,

$$G^{\mathrm{I,II}}(\Omega, f) = G_{\mathrm{A}}^{\mathrm{I,II}}(\Omega)e^{i\varphi_{\mathrm{D}}(\Omega,f)}, \tag{3.24}$$

where $G_{\mathrm{A}}(\Omega)$, the *amplitude modulation*, captures the varying detector sensitivity with direction and polarizations of the GWs,

$$G_{\mathrm{A}}^{\mathrm{I,II}}(\Omega) = \frac{1+\cos^2\theta_{NL}}{2}F_{+}^{\mathrm{I,II}}(\Omega) - i\cos\theta_{NL}F_{\times}^{\mathrm{I,II}}(\Omega). \tag{3.25}$$

The additional $\varphi_{\mathrm{D}}(\Omega, f)$ modulation is the *Doppler phase modulation*, which is the difference between the phase of the wavefront at the detector and at the barycenter (Cutler, 1998):

$$\varphi_{\mathrm{D}}(\Omega, f) = 2\pi\frac{f}{f_c}\sin\theta_N\cos\gamma. \tag{3.26}$$

There is a non-negligible number of Doppler phase cycles only for a GW frequency satisfying $f \geq f_c$ (see definition of f_c below eq. [3.2] above). However, equation (3.3) shows that $f \leq f_{\mathrm{ISCO}} < f_c$, hence the f_c frequency is reached only after ISCO for typical

SMBH component masses of $m_1 = m_2 = 10^6 \mathrm{M}_\odot$ and redshift $z = 1$. Even for smaller $10^5 \mathrm{M}_\odot$ component masses, the total number of cycles, N_{pm}, remains < 1 until the final 5 hr of inspiral. Therefore the Doppler phase (3.26) is practically negligible for SMBH inspirals. In fact, estimating localization errors without accounting for the Doppler phase affects results by less than a factor of 10^{-3} (for $m_1 = m_2 = 10^6 \mathrm{M}_\odot$ at $z = 1$; S. A. Hughes, private communication). Therefore, in eq. (3.24), I neglect $\varphi_{\mathrm{D}}(\Omega, f)$ and restrict ourselves to the approximation

$$G^{\mathrm{I,II}}(\Omega, f) \equiv G_A^{\mathrm{I,II}}(\Omega). \tag{3.27}$$

The explicit frequency-dependence dropped out, and the time evolution of the signal G_A is now fully determined by the time evolution of the angles Ω.

Note that the amplitude modulation (3.25), $G_A^{\mathrm{I,II}}(\Omega)$, is traditionally expressed in complex polar notation (e.g. Cutler, 1998), where the magnitude and argument of the complex number are called *polarization amplitude* and *phase*. As I will show, the mode decomposition is simplest in the original Cartesian complex form (3.25), which already includes both the polarization amplitude and phase; thus, I do not distinguish these two quantities in the following. The function $G^{\mathrm{I,II}}(\Omega, f)$ given in (3.24) also accounts for spin-orbit precession if the orbital orientation (θ_{NL}, ϕ_{NL}) in Ω is chosen to be time-dependent, to satisfy the equations for spin-orbit precession, and if an extra precession phase shift, $\exp(i\delta_P(\theta_{NL}, \phi_{NL}))$, is introduced (see eq. 2.14 in Lang & Hughes 2006) in addition to the Doppler phase in (3.24). In these calculations, I neglect spin precession but in Kocsis et al. (2007) I discuss how the HMD method can be extended to include that effect.

Finally, I express the measured signal (3.22) as

$$h^{\mathrm{I,II}}(\boldsymbol{p}; t) = h_{\mathrm{c}}(\boldsymbol{p}_{\mathrm{fast}}, \boldsymbol{p}_{\mathrm{spin}}; t) \times h_{\mathrm{m}}^{\mathrm{I,II}}(\boldsymbol{p}_{\mathrm{slow}}; t), \tag{3.28}$$

where h_{c} is the *high frequency carrier signal* and h_{m} is the *slow modulation*:

$$h_{\mathrm{c}}(\boldsymbol{p}_{\mathrm{fast}}, \boldsymbol{p}_{\mathrm{spin}}; t) = \mathcal{A}(\mathcal{M}_z, f(t)) e^{i\phi_{\mathrm{GW}}(\boldsymbol{p}_{\mathrm{fast}}, \boldsymbol{p}_{\mathrm{spin}}; t)} \tag{3.29}$$

$$h_{\mathrm{m}}^{\mathrm{I,II}}(\boldsymbol{p}_{\mathrm{slow}}; t) = \frac{G_A^{\mathrm{I,II}}(\Omega(t))}{d_{\mathrm{L}}}. \tag{3.30}$$

Equation (3.28) shows that the two sets of parameters $\boldsymbol{p}_{\mathrm{slow}}$ and $\{\boldsymbol{p}_{\mathrm{fast}}, \boldsymbol{p}_{\mathrm{spin}}\}$ are exclusively determined by the low frequency modulation and the high frequency carrier, respectively. For this reason, I only expect a low level of cross-correlation between these sets of parameters: parameters associated with very different timescale components should essentially decouple. In Sec. 3.6.1 and Appendix A.1, I consider several toy models which allow us to understand the necessary conditions, and the extent to which, parameters associated with high and low frequency components decorrelate in the course of an extended, continuous observation.

3.2.3 Simplifying Assumptions

In the present work, I make the following assumptions:

1. I assume that the amplitude modulation can be used to determine the luminosity distance and angular parameters, $\boldsymbol{p}_{\rm slow} = \{d_{\rm L}, \theta_N, \phi_N, \theta_{NL}, \phi_{NL}\}$, while the other parameters, $\boldsymbol{p}_{\rm fast} = \{\mathcal{M}_z, \mu_z, t_{\rm merger}, \phi_{\rm ISCO}\}$, are determined from the high frequency GW phase. I assume no cross-correlations between these two sets of parameters. This is supported by the results listed in Table 1 of Hughes (2002a), which shows the full covariance matrix of a Monte Carlo realization of 2PN waveforms. The correlation coefficients are ~ 0.1 for the above quantities, and the absolute scale of the second set of parameters is very low in the first place. Berti et al. (2005b,c) also report that the sets $\boldsymbol{p}_{\rm fast}$ and $\boldsymbol{p}_{\rm slow}$ are relatively uncorrelated for general relativity and even for alternative theories of gravity. In the latter case, the carrier $h_{\rm c}(t)$ in the signal (3.28) is modified but not the slow modulation, $h_{\rm m}(t)$, so that the general expectation of decoupling is maintained.

2. I assume that there are no additional errors on the detector orientations $\Phi(0)$ and $\Xi(0)$. These parameters are given by $t_{\rm merger}$ via eq. (3.8) and (3.7), and $t_{\rm merger}$ itself is determined by the high frequency carrier signal to high precision. Using the full data-stream up to ISCO, $\delta t_{\rm merger} \sim 2\,\rm sec$ (Arun, 2006; Hughes, 2002a). Using (3.8) and (3.7), I estimate $|\delta\Phi(0)| = |\delta\Xi(0)| \equiv \omega_\oplus \delta t_{\rm merger} = 4\times10^{-7}\,\rm rad = 0.08''$. This is so small that I expect the errors $\delta\Phi(0)$ and $\delta\Xi(0)$ to be negligible at any relevant end-of-observation times $t_{\rm f} > t_{\rm ISCO}$, even if the $t_{\rm f}$-dependence of these errors scale as steeply as $(S/N)^{-1}$ (see also Appendix A.1).

3. I use the circular, restricted post-Newtonian (PN) approximation for the GW waveform, keeping only the leading order (i.e. Newtonian) term in the signal amplitude. Higher order corrections to the GW amplitude introduce additional structure to the waveform. They improve the parameter estimation uncertainties for high mass

binaries (Van Den Broeck & Sengupta, 2007a,b) and introduce additional correlations between the parameters. It will be important to consider these corrections to the amplitude in future investigations. Arbitrary PN corrections to the GW phase only enter via h_c in the signal given by eq. (3.28). Since I neglect correlations between the sets of parameters $\boldsymbol{p}_{\rm slow}$ and $(\boldsymbol{p}_{\rm fast}, \boldsymbol{p}_{\rm spin})$, all the restricted PN corrections to the phase drop out and become irrelevant for the $\boldsymbol{p}_{\rm slow}$ parameter estimations.

4. I neglect the effects of Doppler phase modulation. This is plausible for SMBH binaries with component masses $m > 10^5 \mathrm{M}_\odot$, since the GW wavelength in this case is generally greater than LISA's orbital diameter and $N_{\rm pm} < 1$ (see eqs. [3.26] and [3.1]).

5. I neglect SMBH spins and, in particular, neglect the spin–orbit precession for angular determinations. This assumption is useful in simplifying the equations and in focusing on the behavior of pure angular modulation. Future studies can incorporate spin–orbit precession by convolving the angular modulation decomposition with spin–orbit effects.

6. I fix the start of LISA observations at a look–back time $t_{\rm i} \equiv \min\{t_0(f_{\rm min}), 1{\rm yr}\}$ prior to merger. This corresponds to the time when the GW inspiral frequency f crosses the low frequency noise wall of the detector at $f_{\rm min} = 0.03$mHz, but I limit the initial look–back time to a maximum of 1yr before merger. Note that LISA's effective mission lifetime is estimated to be 3yr. Integrated observation times longer (but also shorter) than my assumed $t_{\rm i}$ values are possible in principle, depending on source specifics. In a more elaborate treatment, one could define $t_{\rm i}$ as an a priori random variable. I fix $t_{\rm i}$ here mostly for simplicity and focus on the effects of varying the values of $t_{\rm f}$ ($< t_{\rm i}$). In § 3.6.1 I show that localization errors are primarily determined by the end-of-observation time, $t_{\rm f}$, and that values of $t_{\rm i} > 1$yr do not significantly change the evolution or final localization error estimates. If, however, $t_{\rm i} \ll 1$yr (that is, if $t_{\rm merger}$ is within a few months of the beginning of observation), then localization errors can become significantly worse than with $t_{\rm i} = 1$yr.

7. I neglect finite arm-length effects and I do not make use of the three independent observables of the time delay interferometry (Prince et al., 2002). This is a valid assumption for SMBH inspirals since here $f \ll c/L = 0.01$Hz.

8. I neglect any finite orbital eccentricities. I note that, for eccentric orbits, higher order harmonics appear in the GW phase. In principle, since these harmonics affect the high frequency GW phase, but not the slow modulation, including finite eccentricities should not significantly affect localization error estimates. For rather eccentric orbits, high-order harmonics with $f \gg f_c$ can have a non-negligible Doppler phase (3.2), which would lead to an improvement in the determination of θ_N and ϕ_N. Although eccentricity is efficiently damped by gravitational radiation reaction (Peters, 1964), the presence of gaseous circumbinary disks could lead to non-zero eccentricities for at least some LISA inspiral events (Armitage & Natarajan, 2005; Papaloizou et al., 2001).

9. I follow Barack & Cutler (2004b) in calculating the LISA root spectral noise density, $S_n(f)$, which includes the instrumental noise as well as galactic/extra-galactic backgrounds. For the instrumental noise (Berti et al., 2005b), I use the effective non-angularly averaged online LISA Sensitivity Curve Generator[2], while I use the isotropic formulae for the galactic and extra-galactic background (Barack & Cutler, 2004b).

10. My analysis focuses on statistical errors and does not account for possible systematic errors. For example, waveform templates might be inaccurate either due to the imprecision of the theory if the true waveform is not the one predicted by general relativity, or due to practical limitations from necessarily finite realizations of the large template space. Such inaccuracies can introduce new systematic errors.

3.3 Harmonic Mode Decomposition

In my formalism, the angular information of the LISA inspiral signal is contained exclusively in the periodic modulation due to the detector motion around the Sun, which adds an amplitude modulation to the high frequency waveform. This modulation has a fundamental frequency, $f_\oplus = 1/\mathrm{yr}$, along with upper harmonics $jf_\oplus$, where j is an integer. Although it is intuitively clear that the high frequency harmonics will tend to have a vanishing contribution, it is hard to establish this just by looking at eqs. (3.5–3.12), which define the time evolution. In this section I show that it is possible to derive surprisingly simple analytical expressions for the amplitude of each harmonic. I provide an outline of the derivation starting from the commonly used Cutler (1998) formulae

[2] `www.srl.caltech.edu/~shane/sensitivity/`

(3.5–3.12) and alternatively from those in Cornish & Rubbo (2003). I show that the derivation is much simpler in the latter case, in the sense that the Cornish & Rubbo (2003) expression is almost already in the desired form.

3.3.1 Derivation using Cutler (1998)

I expand the modulating signal (3.25,3.30) in a Fourier series

$$h_{\mathrm{m}}(\boldsymbol{p}_{\mathrm{slow}}(0);t) = \frac{G_A(\Omega(t))}{d_{\mathrm{L}}(z)} = \sum_{j=-\infty}^{\infty} g_j(\boldsymbol{p}_{\mathrm{slow}}(0))e^{ij\omega_\oplus t}, \tag{3.31}$$

where $g_j(\boldsymbol{p}_{\mathrm{slow}}(0))$ are the mode amplitude coefficients and $\boldsymbol{p}_{\mathrm{slow}}(0)$ are the distance and angle variables at $t=0$ (see § 3.2.1). The coefficients can be obtained as

$$g_j(\boldsymbol{p}_{\mathrm{slow}}(0)) = \frac{1}{2\pi d_{\mathrm{L}}}\int_0^{1\mathrm{yr}} \mathrm{d}t\, G_{\mathrm{A}}(\Omega(t))e^{-ij\omega_\oplus t}. \tag{3.32}$$

Substituting the definition of $G_{\mathrm{A}}(\Omega(t))$ from eq. (3.25), using the time evolution of $\Omega(t)$, eqs. (3.5–3.12), integral (3.32) can be evaluated.

Although conceptually simple, a direct analytical evaluation of integral (3.32) is overly cumbersome. Thus, for practical reasons, I follow an alternative path. I start with the original Cutler (1998) formulae, given by eqs. (3.14) and (3.25). First, using general trigonometric identities, I can express $\cos 2x$ and $\sin 2x$ with $\tan(x)$ for $x=\phi'_N$ and $x=\psi'$. In the second step, I express and substitute for $\tan\phi'_N$ and $\tan\psi'_N$ with ecliptic variables using (3.11) and (3.12). In the third step, I express the trigonometric functions in complex form. After this step, each term in the beam pattern (3.14) is of the form

$$\frac{\sum_n a_n e^{in\gamma}}{\sum_m b_m e^{im\gamma}}, \tag{3.33}$$

where the sums over n and m integers are finite, containing only a few terms, and a_n and b_n depend only on the angles $(\theta_N, \phi_{NL}, \alpha)$. In the fourth step I simplify the product of fractions. It turns out that, after combining terms, the denominators drop out exactly, leaving a formula just like (3.31), except that the largest element in the sum is $|j|=4$. In the fifth step, I substitute in (3.25), and finally, change back from complex to trigonometric notation for the coefficients, using the half-angles $\theta_N/2$ and

$\theta_{NL}/2$. Finally I arrive to the remarkably simple form:

$$h_{\mathrm{m}}(\boldsymbol{p}_{\mathrm{slow}}) = d_{\mathrm{L}}(z)^{-1}\sum_{j=0}^{4}(LN_jD_j + L^*N_j^*D_j + L^*N_jD_j^* + LN_j^*D_j^*), \tag{3.34}$$

where the functions L, N, and D depend only on the angular momentum angles, sky position angles, and detector angles, respectively:

$$\begin{aligned} L(\theta_{NL},\phi_{NL}) &\equiv \sin^4\left(\frac{\theta_{NL}}{2}\right)e^{-2i\phi_{NL}}, & (3.35)\\ N_j(\theta_N) &\equiv w_j\cos^j\left(\frac{\theta_N}{2}\right)\sin^{4-j}\left(\frac{\theta_N}{2}\right), & (3.36)\\ D_j(\alpha,\gamma) &\equiv ie^{2i\alpha}e^{ij\gamma}, & (3.37)\end{aligned}$$

where $w_j = 1/16\times(9, 12\sqrt{3}, 18, 4\sqrt{3}, 1)$ for $j = (0, 1, 2, 3, 4)$, respectively, and I have defined asterisks to refer to the following conjugates:

$$\begin{aligned} L^*(\theta_{NL},\phi_{NL}) &\equiv L(\pi-\theta_{NL},-\phi_{NL}), & (3.38)\\ N_j^*(\theta_N) &\equiv (-1)^jN_j(\pi-\theta_N), & (3.39)\\ D_j^*(\alpha,\gamma) &\equiv -D_j(-\alpha,-\gamma)\equiv\overline{D_j(\alpha,\gamma)}. & (3.40)\end{aligned}$$

Note that using these conjugate functions, only the non–negative terms $0 \le j \le 4$ remain in the sum (3.34).

Substituting the time dependence implicit in $\gamma \equiv \gamma(0)+\omega_\oplus t$, equation (3.34) becomes

$$h_{\mathrm{m}}(\boldsymbol{p}_{\mathrm{slow}}(0), t) = d_{\mathrm{L}}(z)^{-1}\sum_{j=-4}^{4} g_j(\boldsymbol{p}_{\mathrm{slow}}(0))e^{ij\omega_\oplus t}, \tag{3.41}$$

where the coefficients are

$$g_j(\boldsymbol{p}_{\mathrm{slow}}(0)) = \begin{cases} LN_jD_{|j|}(0) + L^*N_j^*D_j(0) & \text{if } j\ge 0\\ L^*N_{|j|}D_{|j|}^*(0) + LN_{|j|}^*D_{|j|}^*(0) & \text{if } j\le 0\end{cases} \tag{3.42}$$

and the detector functions $D_j(0)$ and $D_j^*(0)$ refer to their values at $t = 0$, $\gamma(0)$. (Note that L, N_j, L^*, N_j^* are all time-independent.) Since the decomposition (3.31) is unique, the coefficients (3.42) that I read off from the result also satisfy eq. (3.32).

3.3.2 Derivation using Rubbo & Cornish 2003

My result in (3.34) can also be derived from the Cornish & Rubbo (2003) formulae for the LISA response function. In their paper, these authors use a different set of angles, which relate to ours as follows: $\theta^{CR} = \theta_N$, $\phi^{CR} = \phi_N$, $\psi^{CR} \equiv \phi_{NL} - (\pi/2)$, $\lambda^{CR} \equiv -\alpha + \phi_N \equiv \Phi - \Xi - (3\pi/4)$, and $\alpha^{CR} \equiv \gamma + \phi_N \equiv \Phi$. Note that my set of angles is very similar to theirs, except that I measure the detector angles relative to the source, ϕ_N. This is advantageous given the rotational symmetry around the Earth orbital axis, making angles relative to the source the only ones that should have an effect on the measured GWs; I expect ϕ_N to drop out of the equations when using α and γ. Note, once again, that the variables $(\theta_N, \phi_N, \theta_{NL}, \phi_{NL}, \alpha)$ are time independent, while $\gamma \equiv \gamma(t)$. Writing the Cornish & Rubbo (2003) beam patterns for low frequencies, which is fully equivalent to Cutler (1998), with my angular variables[3], I get

$$\begin{aligned} F_+^{\rm I,II} &= -\frac{1}{2}[\cos(2\phi_{NL})D_+^{\rm I,II}(t) - \sin(2\phi_{NL})D_\times^{\rm I,II}(t)], &(3.43)\\ F_\times^{\rm I,II} &= -\frac{1}{2}[\sin(2\phi_{NL})D_+^{\rm I,II}(t) + \cos(2\phi_{NL})D_\times^{\rm I,II}(t)], &(3.44)\end{aligned}$$

where

$$\begin{aligned} D_+ = \ & \tfrac{1}{32} \ \{-36\sin^2\theta_N \sin(2\gamma+2\alpha) + (3+\cos 2\theta_N)\\ & \times \ \{\cos(2\phi_N)[9\sin(-2\alpha+2\phi_N) - \sin(4\gamma+2\alpha+2\phi_N)]\\ & + \ \sin(2\phi_N)[\cos(4\gamma+2\alpha-2\phi_N) - 9\cos(-2\alpha+2\phi_N)]\}\\ & - \ 4\sqrt{3}\sin(2\theta_N)[\sin(3\gamma+2\alpha) - 3\sin(\gamma+2\alpha)]\}, \qquad (3.45)\end{aligned}$$

and

$$\begin{aligned} D_\times = \ & \tfrac{1}{8\sqrt{3}} \ \{\sqrt{3}\cos\theta_N[9\cos(-2\alpha) - \cos(4\gamma+4\alpha)]\\ & - \ 6\sin\theta_N[\cos(3\gamma+2\alpha) + 3\cos(\gamma+2\alpha)]\}. \qquad (3.46)\end{aligned}$$

One notices instantly that the time dependence here is much simpler than in the original Cutler (1998) formula, as it is inscribed only in the various harmonics of γ. I can identify the highest harmonic present to be 4γ. Expanding the trigonometric

[3]Cornish & Rubbo (2003) combine the $\sqrt{3}/2$ factor with the beam patterns $F_+^{CR,\rm I,II} = \frac{\sqrt{3}}{2}F^{\rm I,II}$, but I follow the original definition, where $\sqrt{3}/2$ appears only when taking the linear combination of GW polarizations (3.21).

functions using standard identities, I obtain

$$D_+ = -\frac{1}{32}\begin{pmatrix} 9(3+\cos 2\theta_N) \\ -12\sqrt{3}\sin 2\theta_N \\ 36\sin^2\theta_N \\ 4\sqrt{3}\sin 2\theta_N \\ 3+\cos 2\theta_N \end{pmatrix} \cdot \begin{pmatrix} \sin(2\alpha) \\ \sin(2\alpha+\gamma) \\ \sin(2\alpha+2\gamma) \\ \sin(2\alpha+3\gamma) \\ \sin(2\alpha+4\gamma) \end{pmatrix}, \tag{3.47}$$

and

$$D_\times = -\frac{1}{8}\begin{pmatrix} -9\cos\theta_N \\ 6\sqrt{3}\sin\theta_N \\ 0 \\ 2\sqrt{3}\sin\theta_N \\ \cos\theta_N \end{pmatrix} \cdot \begin{pmatrix} \cos(2\alpha) \\ \cos(2\alpha+\gamma) \\ \cos(2\alpha+2\gamma) \\ \cos(2\alpha+3\gamma) \\ \cos(2\alpha+4\gamma) \end{pmatrix}, \tag{3.48}$$

where $\boldsymbol{a}\cdot\boldsymbol{b} = \sum_n a_n b_n$ is the usual dot product. Now, the second sets of elements carry the time dependence and the detector orientation information, while the first sets describe the sky position. Note that the explicit ϕ_N dependence dropped out, as expected. Next, I manipulate equations (3.47,3.48), substituting complex expressions for the trigonometric ones, and substituting these into eq. (3.25). I finally arrive at eq. (3.34) after changing to half–angles $\theta_N/2$ and $\theta_{NL}/2$.

I note that eqs. (3.34) or (3.41,3.42) are fully general expressions, equivalent to the standard LISA inspiral signal in eqns. (3.14) and (3.25). The two data-streams are obtained by substituting $\alpha = \alpha^I$ and α^{II}, corresponding to the two independent LISA-equivalent Michelson interferometers (see § 3.2.1). To verify the final result, I compare numerically the signals computed using eqs. (3.14,3.25) with the signals computed using eqs. (3.41,3.42), for a large set of random choices of angles. Agreement is achieved at machine precision levels.

The main utility of eq. (3.34), is that it can be used to "deconstruct" parameter error histograms, i.e. to understand how the errors depend on the fiducial values of the parameters. As compared to Cornish & Rubbo (2003), my result leads to an explicit decoupling of the signal angular dependence into simple products of one-dimensional functions. In particular, the dependence on sky position, angular momentum, and detector angles are separated. Using the special conjugate functions L^*, D^*, N^*, eq. (3.34) displays the symmetry properties of the signal. Finally, one angular variable, ϕ_N is eliminated exactly.

3.4 Estimating Parameter Uncertainties in the HMD formalism

Parameter estimations for LISA GW inspiral signals are possible with matched filtering and the expected uncertainties can be forecast using the Fisher matrix formalism (Cutler & Flanagan, 1994; Finn, 1992). In this section, I apply this approach to the LISA signal derived in § 3.3, with an angular dependence of the signal decomposed into harmonic modes. In § 3.4.2, I consider the simple case of a high frequency carrier signal that is modulated by a low-frequency function, without any cross-correlation between the two sets of relevant parameters. I derive a simple formula for the estimation of modulating parameter uncertainties. In Kocsis et al. (2007), I consider a more general post-Newtonian signal and show that parameters related to source localization can still be decoupled from the time evolution and the other source parameters.

3.4.1 Fisher Matrix Formalism

Let us consider a generic real signal described by the function $h(x)$, which depends on N parameters $\{p_a\}_{a\in[1,N]}$. The measured signal is $y(x) = h(x) + n(x)$, where $n(x)$ is a realization of the noise specified by a probability distribution. Let us assume that the noise is Gaussian, is statistically stationary with respect to x, has zero mean value, $\langle n(x)\rangle = 0$, where $\langle\rangle$ represents an ensemble average, and has known variance, $\sigma(x)^2 = \langle n(x)^2\rangle$. The parameter estimation errors for p_a can then be calculated using the Cramer-Rao bound (Finn, 1992)

$$\langle \delta p_a\, \delta p_b\rangle \geq \langle \Gamma^{-1}\rangle_{a\,b}, \tag{3.49}$$

where equality is approached for high S/N signals. Here $\Gamma_{a\,b}$ is the Fisher matrix defined by

$$\Gamma_{a\,b} = \int_{x_{\min}}^{x_{\max}} \frac{\partial_a h(x)\, \partial_b h(x)}{\sigma^2(x)} \mathrm{d}x, \tag{3.50}$$

where ∂_a is the partial derivative with respect to the parameter p_a. Note that $\sigma(x)$ here is defined as the noise per unit x. In eq. (3.50), x denotes time t for time-domain samples, or f for frequency-domain samples. The purpose of this work is to study how an arbitrary end of the observation, at $x_{\max}$ (or $t_{\rm f}$ below, for time samples) affects the resultant correlation errors $\langle \delta p_a \, \delta p_b \rangle$, for a fixed start-of-observation at $x_{\min}$ (or $t_{\rm i}$ below, for time samples).

An important quantity for the evolution of parameter estimation errors is the signal-to-noise ratio, S/N, defined by

$$\left(\frac{S}{N}\right)^2 = \int_{x_{\min}}^{x_{\max}} \frac{h^2(x)}{\sigma^2(x)} \mathrm{d}x. \tag{3.51}$$

For LISA, the noise varies with signal frequency. In this case, the Fisher matrix can be evaluated in Fourier space (Cutler & Flanagan, 1994; Finn, 1992),

$$\Gamma(t_{\rm f})_{a\,b} = \mathrm{Re}\left\{ 4 \int_{\rm f_{min}}^{\rm f(t_f)} \frac{\overline{\partial_{\rm a}\tilde{\rm h}({\rm f})}\, \partial_{\rm b}\tilde{\rm h}({\rm f})}{\rm S_n^2(f)} \mathrm{df} \right\}, \tag{3.52}$$

where $\tilde{h}(f)$ is the Fourier transform of $h(t)$, the GW signal (3.28), ∂_a is the partial derivative with respect to parameter p_a, bars denote complex conjugation, and $S_n^2(f)$ is the one-sided spectral noise density (§ 3.2.1).

3.4.2 Approximate solution

I seek an alternative equivalent form of eq. (3.52) specific to GW inspirals for which, as in eq. (3.28), the high frequency carrier signal is decoupled from the slow modulation. In case of SMBH inspirals, with a high frequency signal $h_{\rm c}(t)$ changing its frequency slowly as $f_0(t)$ given in eq. (3.1), and further modulated by a slowly varying function $h_{\rm m}(t)$ as given in eq. (3.28), the integral in eq. (3.52) can be evaluated in the stationary phase approximation, by substituting

$$\tilde{h}(f) = h_{\rm m}[t_0(f)] \times \tilde{h_{\rm c}}(f), \tag{3.53}$$

where $\tilde{h_{\rm c}}(f)$ is the Fourier transform of the carrier signal and $h_{\rm m}[t_0(f)]$ is the modulating function evaluated at the time when the carrier frequency is f. This can be converted to the time domain, by simply changing the integration variable to $t = t_0(f)$ using the frequency evolution in eq. (3.2):

$$\Gamma(t_{\mathrm{f}})_{a\,b} = \mathrm{Re}\left\{ 4 \int_{\mathrm{t_f}}^{\mathrm{t_i}} \frac{\overline{\partial_{\mathrm{a}}\tilde{\mathrm{h}}(\mathrm{t})}\;\partial_{\mathrm{b}}\tilde{\mathrm{h}}(\mathrm{t})}{\mathrm{S_n^2}[\mathrm{f_0(t)}]} \left| \frac{\mathrm{df_0(t)}}{\mathrm{dt}} \right| \mathrm{dt} \right\}, \tag{3.54}$$

and

$$\tilde{h}(t) = h_{\mathrm{m}}(t) \times \tilde{h_{\mathrm{c}}}[f_0(t)]. \tag{3.55}$$

I are only interested in estimating uncertainties for the $\boldsymbol{p}_{\mathrm{slow}}$ variables (§ 3.2.1), which are determined exclusively by $h_{\mathrm{m}}(t)$. Recall from eq. (3.29) that $|h_{\mathrm{c}}(t)| = \mathcal{A}$ so that, for the Fourier transform[4], I have $|h_{\mathrm{c}}(t)|^2 = 4|\tilde{h_{\mathrm{c}}}(f)|^2(\mathrm{d}f/\mathrm{d}t)$. Using these relationships, let us define the instantaneous relative noise amplitude per unit time $\sigma(t)$ as

$$\sigma^{-2}(t) = 4\frac{\tilde{h_{\mathrm{c}}}^2[f_0(t)]}{S_n^2[f_0(t)]}\left|\frac{\mathrm{d}f_0(t)}{\mathrm{d}t}\right| = \frac{\mathcal{A}^2[f_0(t)]}{S_n^2[f_0(t)]} = \frac{3\sqrt{5}}{4}\frac{\mathcal{M}_z^{5/2}t^{-1/2}}{S_n^2[f_0(\mathcal{M}_z,t)]}. \tag{3.56}$$

The last equality follows from the Newtonian waveform and frequency evolution, equations (3.23) and (3.1). I point out that the mass dependence is captured entirely by $\sigma(t)$ and does not appear anywhere else in what follows.

By combining eqs. (3.54), (3.55), and (3.56), I arrive at

$$\Gamma(t_{\mathrm{f}})_{a\,b} = \int_{t_{\mathrm{f}}}^{t_{\mathrm{i}}} \frac{\mathrm{Re}[\overline{\partial_{\mathrm{a}}\mathrm{h_m(t)}}\;\partial_{\mathrm{b}}\mathrm{h_m(t)}]}{\sigma^2(t)}\mathrm{d}t. \tag{3.57}$$

Equation (3.57) is the special case of (3.52), where the carrier signal-to-noise ratio and modulation, h_{m}, are conveniently isolated.

I are now ready to make use of the harmonic mode decomposition. Substituting eq. (3.31) into (3.57) gives

$$\Gamma(t_{\mathrm{f}})_{a\,b} = \mathrm{Re}\left\{ \sum_{\mathrm{j_1,j_2=-4}}^{4} \overline{\partial_{\mathrm{a}}\mathrm{g_{j_1}}}\;\partial_{\mathrm{b}}\mathrm{g_{j_2}}\mathrm{P_{j_2-j_1}(t_f)} \right\}, \tag{3.58}$$

[4]The reason for the factor 4 is that the mean squared of $\cos(x)$ or $\sin(x)$ is 1/2 in (3.18), and since I use one-sided signals in frequency domain ($f > 0$), responsible for another factor of 1/2 in comparison.

where

$$P_{j_2-j_1}(t_\mathrm{f}) = \int_{t_\mathrm{f}}^{t_\mathrm{i}} \frac{e^{i(j_2-j_1)\omega_\oplus t}}{\sigma^2(t)}\mathrm{d}t. \tag{3.59}$$

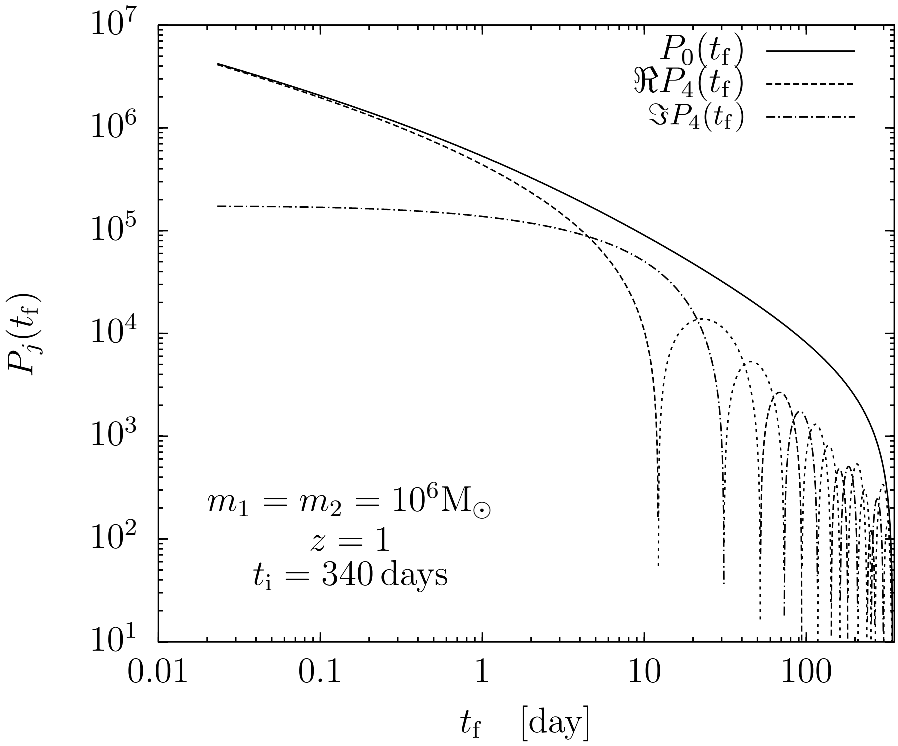

Figure 3.1 The time evolution of the fundamental functions $P_j(t_\mathrm{f})$, used to construct the Fisher matrix to forecast localization errors by LISA. The dependence of the Fisher matrix on the look–back time t_f is obtained from the 9 fundamental functions with $0 \leq j \leq 8$. The curves show $P_0(t_\mathrm{f})$, as well as the real and imaginary parts of $P_4(t_\mathrm{f})$, for $m_1 = m_2 = 10^6\mathrm{M}_\odot$ and $z = 1$. Thin dotted lines represent negative values. Note that $P_0(t_\mathrm{f}) \equiv (S/N)^2$, which is the simple scaling of inverse squared errors, neglecting correlations. The signal-to-noise ratio scales steeply, approximately as $S/N \propto t_\mathrm{f}^{-1}$. The curve $P_4(t_\mathrm{f})$ illustrates how all the other similar $P_j(t_\mathrm{f})$ functions vary, with a relative number $|j|$ of oscillations, and $P_{-j}(t_\mathrm{f}) \equiv \overline{P_j(t_\mathrm{f})}$.

The function $P_j(t_\mathrm{f})$ is shown in Figure 3.1 for $j = 0$, together with real and imaginary parts for the $j = 4$ case, for $m_1 = m_2 = 10^6\mathrm{M}_\odot$ at $z = 1$. Since the accumulated signal-to-noise ratio is $S/N = P_0(t)$, the figure shows that the instantaneous signal-to-noise ratio is $[\mathrm{d}/\mathrm{d}t](S/N) = [\mathrm{d}/\mathrm{d}t]P_0(t) \approx t^{-2}$. The extrapolated signal-to-noise blows up at "merger" ($t = 0$). Data analysis for such a non-stationary signal-to-noise ratio evolution has several interesting implications, which I study further with toy models in Appendix A.1. I find that, for such a signal-to-noise ratio evolution, specific combinations of parameters can always be measured to very high accuracy.

The time dependence in eq. (3.59) couples only to the combination $j = j_2 - j_1$. This allows to rearrange the double sum on (j_1, j_2) and evaluate one of them independent of time:

$$\Gamma(\boldsymbol{p}_{\rm slow}, t_{\rm f})_{a\,b} = \mathrm{Re}\left\{\sum_{\rm j=-8}^{8} [\mathcal{F}_{\rm j}(\mathrm{p}_{\rm slow}(0))]_{\rm a\,b} \mathrm{P}_{\rm j}(\mathrm{t}_{\rm f})\right\}, \tag{3.60}$$

$$\tag{3.61}$$

where

$$[\mathcal{F}_j(\boldsymbol{p}_{\rm slow}(0))]_{a\,b} = \sum_{j'=-8}^{8} \overline{\partial_a g_{j+j'}(\boldsymbol{p}_{\rm slow}(0))}\, \partial_b g_j(\boldsymbol{p}_{\rm slow}(0)). \tag{3.62}$$

My parameters in the correlation matrix are $p_a = (d_{\rm L}, \theta_N, \phi_N, \theta_{NL}, \phi_{NL})$ since I assume that the other parameters, i.e. $\{\mathcal{M}_z, \eta_z, \phi_{\rm ISCO}, t_{\rm merger}, \alpha, \gamma(0)\}$, are known from the high frequency carrier signal (§ 3.2.3). It is straightforward to compute the derivatives of $g_j(d_{\rm L}, \Omega)$ using eq. (3.42) for all parameters p_a, except ϕ_N. The ϕ_N dependence in g_j in eq. (3.42) is implicit in $\alpha \equiv \alpha(\Xi(0), \Phi(0), \phi_N)$ and $\gamma(0) \equiv \gamma(\Phi(0), \phi_N)$ (see § 3.2.1). Since I assume that $\Xi(0)$ and $\Phi(0)$ are measured to very high precision with the high frequency carrier (§ 3.2.3), I can use the chain rule to express the ϕ_N derivative as $\partial_{\phi_N} g_j = \partial_\alpha g_j - \partial_{\gamma_0} g_j$.

Up to this point I did not make use of the fact that the LISA signal is equivalent to two orthogonal arm interferometers rotated by $\Delta\alpha = \pi/4$ with respect to each other. To account for both data-streams being measured simultaneously, the Fisher matrix is written as the sum of the two Fisher matrices corresponding to each individual interferometer. Writing out only the α dependence, I have $\Gamma^{\rm tot}_{a\,b}(\alpha) = \Gamma_{a\,b}(\alpha) + \Gamma_{a\,b}(\alpha - \pi/4)$. Finally, according to eq. (3.49), the parameter error covariance matrix is the inverse of this total Fisher matrix:

$$\langle \delta p_a\, \delta p_b \rangle \geq [\Gamma_{a\,b}(d_{\rm L}, \theta_N, \theta_{NL}, \phi_{NL}, \alpha, \gamma(0)) + \Gamma_{a\,b}(d_{\rm L}, \theta_N, \theta_{NL}, \phi_{NL}, \alpha - \pi/4, \gamma(0))]^{-1}. \tag{3.63}$$

Equation (3.63) along with (3.60) is my final expression, describing the time evolution of parameter estimation uncertainties. I note that after combining both data-streams, the matrices $[\mathcal{F}_j(\boldsymbol{p}_{\rm slow}(0))]_{a\,b}$ for $4 < |j| \leq 8$ modes vanish exactly for all $\boldsymbol{p}_{\rm slow}(0)$.

Let me emphasize the most important features of eq. (3.60):

- The parameter dependence is separated from the time dependence. The Fisher matrix, $\Gamma_{a\,b}$, is written as a linear combination of matrices $\mathcal{F}_j(\boldsymbol{p}_{\rm slow})$ weighted by the scalars $P_j(t)$, where $\mathcal{F}_j(\boldsymbol{p}_{\rm slow})$ is independent of time and $P_j(t)$ is independent of the parameters p_a. Evaluating $\mathcal{F}_j(\boldsymbol{p}_{\rm slow})$ requires the computation of the parameter derivatives $\partial_a g_j$.

- The evaluation of all integrals $P_j(t_{{\rm f}n})$ for different $n = 1, 2, \ldots, N_{t_{\rm f}}$ can be done in the same amount of time as needed for a single integration, since the $t_{\rm f}$ dependence enters only in the integration bound in eq. (3.59),

- Large Monte Carlo (MC) simulations can easily be performed since the time evolution is given by a small number of functions, $P_j(t)$, which can be calculated a priori and pre-saved. No integrations at all are necessary during the MC simulation for calculating distributions of correlation matrices.

3.5 Results

Having described the HMD formalism in detail, I now apply it to build MC simulations aimed at studying how RMS source localization errors [5] evolve as a function of look–back time, $t_{\rm f}$, before merger. The low computational cost of the HMD method allows us to survey simultaneously the dependencies on source sky position, SMBH masses and redshifts. I carry out MC calculations with 3×10^3 random samples for the angles $\cos\theta_N, \cos\theta_{NL}, \phi_{NL}, \alpha, \gamma(0)$. Several thousands values of M and z are considered, in the range $10^5 < M/{\rm M}_\odot < 10^8$ and $0.1 \leq z \leq 7$. In addition, I ran specific MC calculations to study possible systematic effects with respect to the source sky position, by fixing θ_N and ϕ_N (on a grid of several hundred values) and varying all the other relevant angles.

In all of my computations, I calculate the error covariance matrix for $d_{\rm L}$, θ_N, ϕ_N, θ_{NL}, and ϕ_{NL}. Following Lang & Hughes (2006), I calculated the major and minor axes

[5] The Fisher matrix method yields $\sqrt{\langle \delta p_i^2 \rangle}$ RMS error for each set of fiducial angles. As an approximation, I identify the distribution of errors with the distribution of RMS errors.

of the 2D sky position uncertainty ellipsoid, $2a$ and $2b$, and the equivalent diameter, $\sqrt{4ab}$.

I have verified my HMD implementation and the general validity of my assumptions by comparing my results at ISCO with those of Lang & Hughes (2006) (for $m_1 = m_2 = 10^5, 10^6, 10^7 \mathrm{M}_\odot$ at $z = 1$ and $m_1 = m_2 = 10^5, 10^6 \mathrm{M}_\odot$ at $z = 3$, in the no spin precession case). Depending on SMBH masses and redshifts, I found agreement at the 5–30% level for the mean errors on the luminosity distance, major axis, and minor axis. The small discrepancies may be due to differences in the set of assumptions made. Lang & Hughes (2006) account for the small cross-correlations between the $\boldsymbol{p}_{\rm slow}$ and $\{\boldsymbol{p}_{\rm fast}, \boldsymbol{p}_{\rm spin}\}$ parameters and they choose $t_{\rm i}$ to be uniformly distributed between merger time and LISA's mission lifetime. Recently, Lang & Hughes (2006) reported angular errors that are a factor of 2–3 lower, which are inconsistent with my results at this level. Nevertheless, these discrepancies are still small relative to the typical width of error distributions or to the systematic variations of mean errors with t_f, M, and z (from a factor of few to orders of magnitudes, see Fig. 3.2 below). This successful comparison justifies the use of the HMD method to study the dependence of localization errors on look–back time.

3.5.1 Time dependence of source localization errors

I calculate the variation with look–back time, $t_{\rm f}$, of the distribution of marginalized parameter errors for a range of values of $M, z, \theta_N, \theta_{NL}, \phi_{NL}, \alpha, \gamma(0)$. Figure 3.2 shows results for random angles and $m_1 = m_2 = 10^6 \mathrm{M}_\odot$, at $z = 1$.

The left panel shows the luminosity distance error, $\delta d_{\rm L}$, while the right panel describes the equivalent diameter, $2\sqrt{ab}$, of the sky position error ellipsoid with minor and major axes a and b. The figure displays results for three separate cumulative probability distribution levels, $90\%, 50\%, 10\%$, so that 10% refers to the best 10% of all events, as sampled by the random distribution of angular parameters. The evolution of errors scales steeply with look–back time for $t_{\rm f} \gtrsim 40$ days. In this regime, the improvement of errors is proportional to $(S/N)^{-1}$. For smaller look–back times, errors stop improving in the "worst" (90% level) case, improve with a much shallower slope than $(S/N)^{-1}$ for the "typical" (50% level) case, and keep improving close to the $(S/N)^{-1}$ scaling in the "best" case (10% level among the realizations of fiducial angular parameters). Although Figure 3.2 shows only the equivalent diameter of the 2D sky localization error ellipsoid, I have also computed the evolution of the distribution of the minor and major axes. I

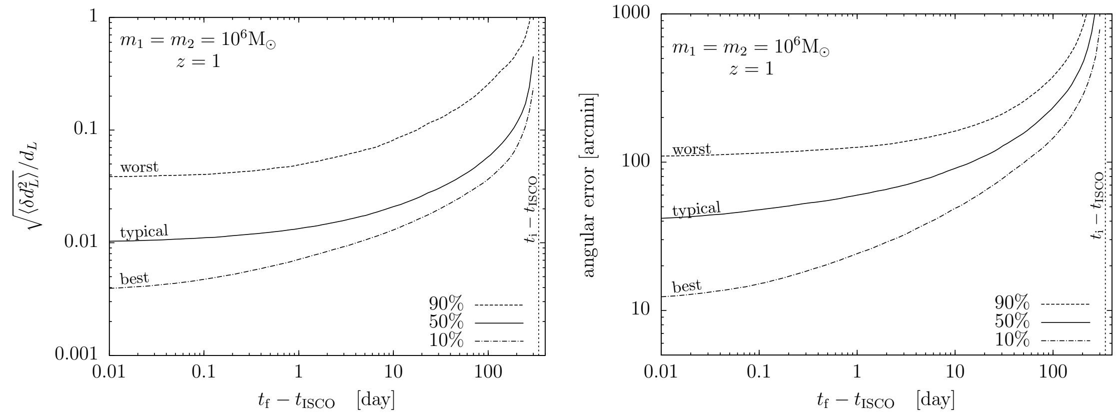

Figure 3.2 Evolution with pre-ISCO look–back time, t_f, of LISA source localization errors, for $M = 2 \times 10^6\mathrm{M}_\odot$ and $z = 1$. The left panel shows luminosity distance errors and the right panel shows sky position angular errors (equivalent diameter, $2\sqrt{ab}$, of the error ellipsoid). Best, typical, and worst cases for random orientation events represent the 10%, 50%, and 90% levels of cumulative error distributions, respectively. Errors for worst case events effectively stop improving at a finite time before ISCO, even though the signal-to-noise ratio accumulates quickly at late times. Errors for best case events (especially the minor axis) follow the signal-to-noise ratio until the final few hours before merger.

find that $a \approx b \approx \sqrt{ab}$ initially (i.e. the ellipsoid is circular), but the geometry changes significantly during the last two weeks to merger. For example, in the typical case, the major axis a stops improving at late times, while the minor axis a maintains a steep evolution. Therefore the eccentricity of the 2D angular error ellipsoid changes quickly with look–back time. This is important because large eccentricities can play a role in assessing observational strategies for EM counterpart searches (Kocsis et al., 2007).

To map possible systematic effects with respect to source sky position, I carried out MC computations with random $(\cos\theta_{NL}, \phi_{NL}, \alpha)$ angles (sample size $N_{MC} = 3 \times 10^3$) but fixed source sky latitude and longitude relative to the detector (θ_N, γ), for $m_1 = m_2 = 10^6\mathrm{M}_\odot$ and $z = 1$. I find no systematic trends with sky position for δd_L, for any value of the look–back time, t_f. Neither do I find systematic trends with sky position for the distributions of minor and major axes of the angular ellipsoid, for any value of the look–back time, t_f, as long as θ_N is not along the equator. The case of equatorial sources, with $\theta_N \approx 90°$ and a short look–back time t_f before merger, is the only nontrivial one I have identified. In that case, I find a minor systematic trend with γ longitude. The error distributions shift periodically up and down, relative to the average, when changing γ from 0 to 2π.

In addition, to map dependencies with mass–redshift–look–back time of localization errors, I carried out MC computations with arbitrary $(\cos\theta_N, \cos\theta_{NL}, \phi_{NL}, \alpha, \gamma)$ angles, with sample size $N_{MC} = 3\times10^3$, for several thousand pairs of (M, z) values. I find that the evolution with look–back time of error distributions depends sensitively, and in a complicated way, on the mass-redshift parameters. Generally, localization errors increase with redshift. Firstly, the S/N is approximately proportional to the instantaneous value $\sigma(t_{\rm ISCO}) \propto \eta^{3/4}[(1+z)M]^{5/4}/d_{\rm L}(z)S_n(f_{\rm ISCO})^{-1}$ (eq. [3.56]) and, secondly, the beginning-of-observation time scales as $t_{\rm i} \propto \eta^{-1}[(1+z)M]^{-5/3}$ (eq. [3.2]). For $(1+z)M < 4\times10^6{\rm M}_\odot$, the total observation time can exceed one year and the second effect is unimportant. I further describe mass–redshift dependencies below, in § 3.5.2, in relation to advance warning times for targeted electromagnetic counterpart searches.

The results on localization errors from my extensive exploration of the parameter space of potential LISA sources can be summarized as follows:

1. Probability distributions
   - The error distributions for $\delta d_{\rm L}$, $2a$, and $2b$ all have long tails: 1%–99% cumulative probability levels are separated by factors of ~ 100, while the 10%–90% levels are separated by factors of ~ 10.
   - The $\delta d_{\rm L}$ distribution is skewed, with a median closer to the best case, a median smaller than the mean, even on a logarithmic scale. On the other hand, sky localization error distributions are roughly symmetric on a logarithmic scale.
2. Fiducial parameter dependencies
   - The $\delta d_{\rm L}$ errors are roughly independent of fiducial angles throughout the observation.
   - For non-equatorial sources, the distribution of sky localization errors, $(2a, 2b)$, is independent of sky position, i.e. the distribution does not have a systematic dependence on θ_N and $\gamma \equiv \Phi - \phi_N$ (for random $\alpha, \theta_{NL}, \phi_{NL}$).
   - There is a small systematic trend with γ for equatorial sources.
   - There is a complicated dependence of sky localization errors on $\mathcal{M}$, z, and look–back time $t_{\rm f}$. For long observation times, errors scale with $(S/N)^{-1} \approx [(1+z)\mathcal{M}]^{5/4}d_{\rm L}(z)^{-1}S_n(f_{\rm ISCO}(M,z))^{-1}f_a(t_{\rm f})$, where $f_a(t_{\rm f})$ is the $t_{\rm f}$-scaling shown in Fig 3.2. For larger redshifted masses, the scaling has a complicated structure in the $M, z, t_{\rm f}$ space that I did not analyze in detail (but see eq. (A.10) in the Appendix for scalings in terms of $t_{\rm i}$ and $t_{\rm f}$.)

3. Time dependence

    - Luminosity distance and sky localization errors roughly scale with $(S/N)^{-1}$ until 2 weeks before ISCO.
    - For the luminosity distance $\delta d_{\rm L}$ and the major axis $2a$, there is little improvement within the last week before ISCO for the typical to worst cases (i.e. 50%–90% levels of cumulative error distributions).
    - For the minor axis $2b$, only the worst case events stop improving within the last week. The typical to best cases continuously improve until the last hour.
    - The eccentricity of the sky localization error ellipsoid changes with time during the first and last two weeks of observation. The eccentricities are smaller in between these two time intervals. For a detailed discussion of the eccentricity and its impact on counterpart searches, see Kocsis et al. (2007).
    - For the luminosity distance $\delta d_{\rm L}$, the relative width of error distributions does not change during observation and variations in the difference between the 90% and 10% levels of the cumulative distributions do not exceed 10%, except for the initial weeks, when the distribution is much more spread out.
    - For the sky localization errors, the width of error distributions increases during the final two weeks of observation, by a factor ~ 2 for the major axis and a factor ~ 4 for the minor axis.

3.5.2 Advance warning times for EM searches

From the astronomical point of view, being able to identify with confidence, prior to merger, a small enough region in the sky where any prompt electromagnetic (EM) counterpart to a LISA inspiral event would be located, is of great interest. With sufficient "warning time," it would then be possible to trigger efficient searches for EM counterparts as the merger proceeds and during the most energetic coalescence phase. In particular, an efficient strategy to catch such a prompt EM counterpart would be to continuously monitor with a wide-field instrument a single field-of-view (FOV), through coalescence and beyond. Astronomical strategies for EM counterpart searches are the focus of a second paper in this series (Kocsis et al., 2007).

Given an angular scale, $\theta_{\rm FOV}$, corresponding to the hypothetical FOV of a specific astronomical instrument, it is thus of considerable interest to determine the value of the look–back time t_f at which the major axis, minor axis or equivalent diameter of the sky localization error ellipsoid provided by LISA just reach the relevant $\theta_{\rm FOV}$ scale. This would allow one to trigger an efficient search for EM counterparts, in a well defined region of the sky that can be monitored. I will hereafter refer to this time as the *advance warning time*. Note that it is important to differentiate the sizes of the major and minor axes of the angular error ellipsoid in this context because the eccentricity can be large, and thus important in assessing optimal strategies for EM counterpart searches (Kocsis et al., 2007).

For definiteness, I evaluate advance warning times for angular diameters $\theta_{\rm FOV} = 1°$ and 3.57° here but generalizations to other $\theta_{\rm FOV}$ values are obviously possible. The choice of the latter figure is motivated by the 10 deg^2 FOV proposed for the future Large Synoptic Survey Telescope, or LSST (Tyson, 2002). Figure 3.3 shows advance warning times for a fixed source redshift at $z = 1$ and various values of the total SMBH mass, M. Figure 3.4 shows similar results for various source redshifts, at a fixed value of $M = 2 \times 10^6 {\rm M}_\odot$.

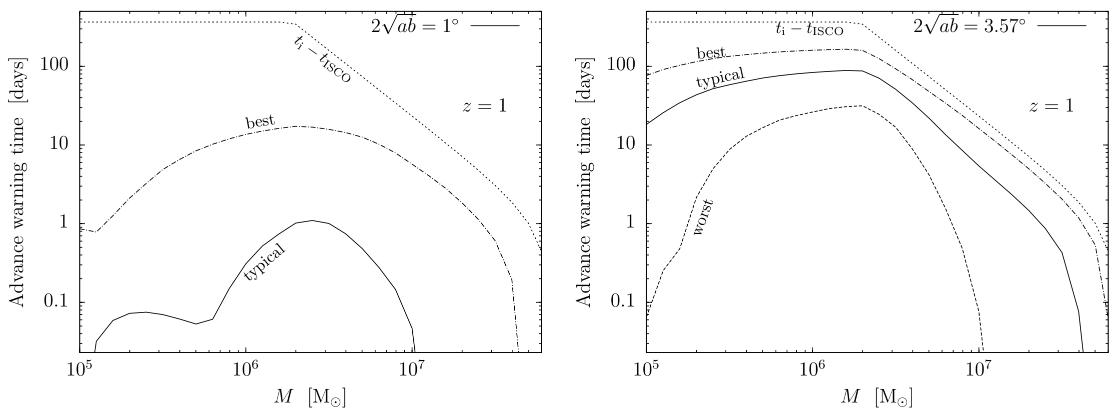

Figure 3.3 Advance warning times (in days) for equal mass binary inspirals at $z = 1$, as a function of total mass, M (in solar units). Best, typical, and worst cases refer to 10%, 50%, and 90% levels of cumulative error distributions for random orientation events, as before. The advance warning times shown correspond to the values of look–back times when the equivalent diameter, $2\sqrt{ab}$, of the error ellipsoid first reaches 1° (left panel) or an LSST-equivalent field-of-view (3.57°, right panel). In the left panel, the worst case events are not shown because angular errors are too large even at ISCO. For the largest mass SMBHs, the maximum observation time (and thus $t_{\rm i}$) is below one year.

In each case, I consider equal mass SMBH binaries and a maximum observation time of 1yr (or lower if set by the GW noise frequency wall at 0.03mHz). Each panel in Figs. 3.3 and 3.4 shows the values of advance warning times at which the equivalent

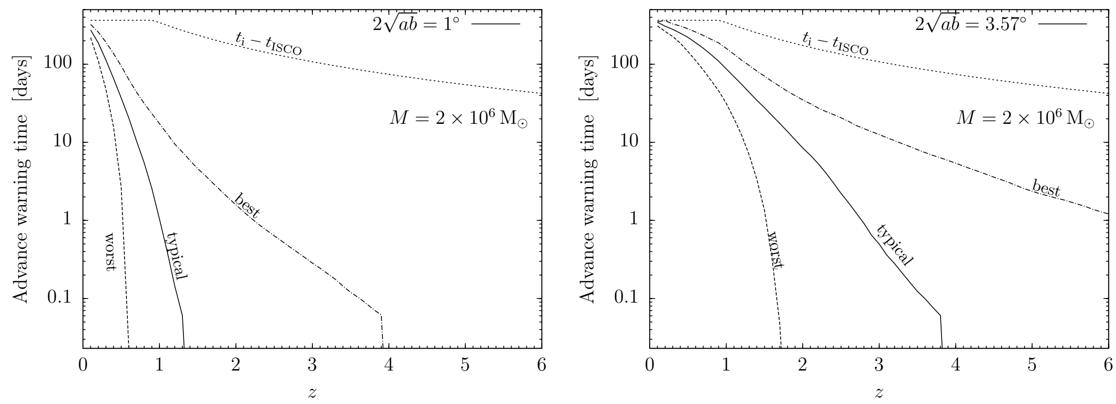

Figure 3.4 Same as Fig. 3.3, for a fixed total mass $M = 2 \times 10^6 \mathrm{M}_\odot$ but various values of the source redshift, z.

diameter $2\sqrt{ab}$ of the localization error ellipsoid drops below the reference $\theta_{\rm FOV}$ value. For each case, I show results for cumulative error distribution levels of 10%, 50%, and 90%, labeled "best", "typical," and "worst" cases, as before. Figure 3.3 shows that LISA can localize on the sky events at $z = 1$ to within an LSST FOV at least one month ahead of merger, for 50% of events with masses $2 \times 10^5 \mathrm{M}_\odot \leq M \leq 3 \times 10^6 \mathrm{M}_\odot$, and at least 4 days ahead of merger for 90% of events in the same mass range. Figure 3.4 shows that advance warning times decrease with redshift, leaving at least 1 day ahead of merger for 50% of events with $M = 2 \times 10^6 \mathrm{M}_\odot$, as long as $z \lesssim 1$ for $\theta_{\rm FOV} = 1^\circ$ and as long as $z \lesssim 3$ for an LSST FOV. For events with this mass scale and the LSST FOV, there is a 10% chance that a 1 day advance warning is possible up to $z \sim 5$–6.

Figures 3.3 and 3.4 display advance warning times for single one dimensional slices of the full (M, z) space of potential LISA events. With the HMD method, however, it is possible to explore the entire parameter space of SMBH inspirals by repeating the calculation on a dense grid of (M, z) values. I construct a uniform grid in the $(\log M, z)$ plane, with $\Delta z = 0.1$ and $\Delta \log M = 0.1$, and perform MC computations with 3×10^3 randomly oriented angles for each grid element. As a result, I obtain a complete description of the time evolution of sky localization errors in the large parameter space of potential LISA sources. Figure 3.5 displays advance warning time contours from this extensive MC calculation, for typical (50%) and best case (10%) events, adopting the LSST FOV as a reference.

Advance warning time contours are logarithmically spaced, with solid-red contours every decade and a thick red line highlighting the 10 day contour. Since advance warning times were computed on a finite mesh, contour levels for arbitrary M and z values were

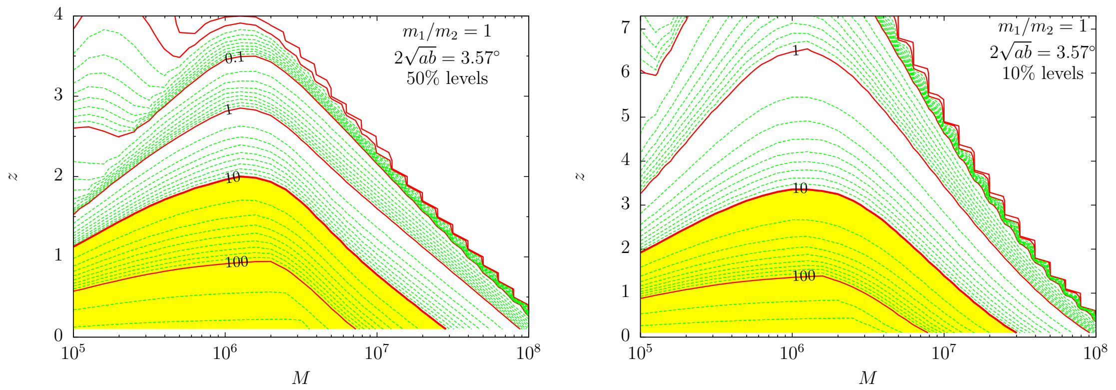

Figure 3.5 Contours of advance warning times in the total mass (M) and redshift (z) plane with SMBH mass ratio $m_1/m_2 = 1$. The contours trace the look–back times at which the equivalent radius ($2\sqrt{ab}$) of the localization error ellipsoid first reach an LSST-equivalent field-of-view (3.57°). The contours correspond to the 50% *(left)* and 10% *(right)* level of cumulative distributions for random orientation events. The contours are logarithmically spaced in days and 10 days is highlighted with a thick line.

obtained by interpolation. My interpolated mesh is smooth if $t_\mathrm{f} \sim 0.1$ day, but it gets edgy for short advance warning time approaching ISCO. Figure 3.5 shows that a 10 day advance warning is possible with a unique LSST-type pointing for a large range of masses and source redshifts, up to $M \sim 3 \times 10^7 \mathrm{M}_\odot$ and $z \sim 1.9$. The right shows how far the advance warning concept can be stretched, by focusing on the 10% best cases of random orientation events. In this case a 10 day advance warning is possible up to $z \sim 3$ for masses around $M \sim 10^6 \mathrm{M}_\odot$. Note that, in both cases, allowing for a warning of just one day would extend considerably the range of masses and redshifts for which a unique LSST-type pointing is sufficient.

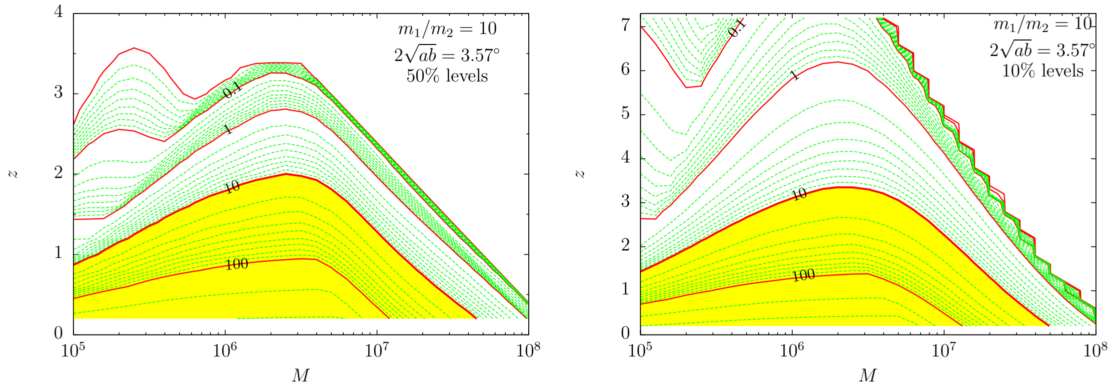

Figure 3.6 Same as Fig. 3.5, except for a SMBH mass ratio of $m_1/m_2 = 10$.

These results can also be generalized to unequal-mass SMBH binaries. At fixed total mass, M, an unequal-mass binary has an instantaneous signal-to-noise ratio that is reduced because of a lower η value, but it also has a total observation time that is potentially longer. Localization errors for unequal-mass inspiral events with total observation times longer than a month (i.e. with $\eta_{0.25}^{2/5}(1+z)\,M < 1.8\times10^7\mathrm{M}_\odot$) are degraded relative to the equal-mass cases discussed so far. For larger total mass, however, the worsening of errors is mitigated, or even reverted, relative to the equal mass case, thanks to the longer observation time. The error ellipsoid also becomes less eccentric thanks to this additional observation time. Figure 3.6 summarizes results on advance warning times from the same MC computations as in Fig. 3.5, but this time for unequal-mass SMBH binaries with mass ratio $m_1/m_2 = 10$. Despite a systematic degradation in advance warning times (especially noticeable at low M values), the main effect of introducing a mass ratio $m_1/m_2 = 10$ is to shift advance warning time contours to somewhat larger values of total mass, M. My main conclusions on advance warning times are not very strongly affected by the inequality of mass components in the population of SMBH binaries considered.

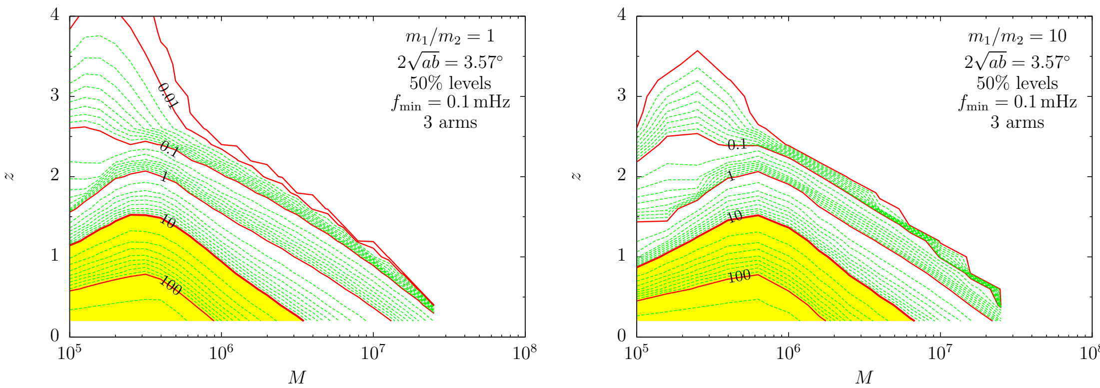

Figure 3.7 Same as the left panels of Figs. 3.5 and 3.6, except for a degraded minimum detector frequency of $f_{\rm min} = 0.1$mHz.

Finally, it is important to understand how sensitive the results are to the LISA detector characteristics. In particular, I examined how advance warning times are affected by increasing the minimum frequency noise wall or by loosing one of the arms of the 3-arm constellation. Figure 3.7 displays results for $f_{\rm min} = 10^{-4}$Hz, for $m_1/m_2 = 1$ and $m_1/m_2 = 10$. Increasing $f_{\rm min}$ mostly reduces the total observation time for high mass inspirals ($t_{\rm i} \sim f_{\rm min}^{-8/3} M_z^{-5/3}$; see eq. [3.2]) and reduces the signal-to-noise ratio by a small factor. As a result, the advance warning time contours primarily shift in the (M, z) plane in the direction of smaller total masses by a factor of ~ 7, and secondly shift moderately

(30–50%) to smaller redshifts. Loosing one LISA arm (i.e. using only one of the two interferometers) most importantly removes the ability of the second datastream to break correlations in localization errors and also reduces the signal-to-noise by a small factor. As a result errors do not improve much during the last ~ 10 days before merger. Compared to the case with two interferometers, contours representing an advance warning of less than 10 days are shifted to significantly smaller z (especially for the minor axis of the sky localization ellipsoid), close to the 10–day contour, but warning times beyond ~ 10 days worsen only moderately. I conclude that even if $f_{\rm min} = 0.1$mHz or if only one of the two interferometers is used, LISA still admits 10–day advance localizations for a broad range of masses and redshifts, between $10^5 \lesssim M \lesssim 2 \times 10^6$ and $z \lesssim 1$.

3.6 Discussion

I have introduced a novel technique, the HMD method, to compute time–dependent GW inspiral signals for LISA. The method relies on the fact that LISA's orbital motion induces a modulation on timescales that are long relative to the inspiral GW frequency. Since this modulation is periodic, with a fundamental frequency of $f_\oplus$, it can be expanded in a discrete Fourier sum. In the HMD formalism, dependencies on sky position, orbital angular momentum orientation, and detector orientation in the LISA signal are inscribed in time-independent coefficients, while time-dependent basis functions are independent of these angles. This decomposition helps to reduce the computational cost of Monte Carlo simulations exploring the time-dependence of source localization errors by orders of magnitude.

Moreover, the HMD method can be used in conjunction with plausible approximations to further decrease the computational cost of explorations of the parameter space of localization errors for LISA inspiral events. In my analysis, I identified two different characteristic frequency constituents of the signal: the high frequency restricted post-Newtonian GW inspiral waveform and the low frequency amplitude modulation resulting from the detector's orbital motion. In the HMD method, these two components separate and parameters that depend only on the low frequency modulation (such as the source position and the orbital angular momentum angle) can be estimated independently of the other source parameters determined by the high frequency carrier signal. My working assumption was that cross-correlations among these two sets of parameters must be much smaller than parameter correlations within either set. This hypothesis is valid very generally in the no spin limit for SMBHs, as shown by full Fisher matrix calculations without such approximations for general relativity (Hughes, 2002a) and alternative theories of gravity (Berti et al., 2005b).

In order to further examine the validity of my assumptions and the ultimate boundaries of my models, and to understand my results, I have constructed illustrative toy models that I now describe in some detail. These toy models show that the separation of parameters into various subsets associated with different characteristic frequencies of the signal is a rather general property, which turns out to be an efficient way of reducing the computational cost of error estimations for the LISA problem.

3.6.1 Simple toy models

In this section, I discuss very simple toy models which capture the essence of the problem posed by the time-evolution of parameter error estimations. I then use these models to answer general questions on the LISA-specific parameter estimation problem.

My harmonic decomposition technique is based on the simple intuition that the angular information can be deduced from the slow periodic modulation of the high frequency GW waveform. In § 3.3, I have shown that modulation harmonics with frequencies larger than $4f_\oplus$ vanish exactly. Here, I discuss the general properties of such a modulation. In the case of LISA, the high frequency carrier signal has an effective, cycle-averaged signal-to-noise ratio which monotonically increases with time as SMBH binaries approach merger. To mimic such events, I also assume in all of my toy models that the instantaneous signal-to-noise ratio continuously improves throughout the observation.

I seek answers to the following questions:

1. How do mean errors evolve during the final days of observation?

   On the one hand, in standard angle-averaged treatments (e.g. Berti et al., 2005b; Kocsis et al., 2006; Arun, 2006), an evolution of errors with the inverse of the signal-to-noise ratio is generally assumed. This would suggest a large improvement during the last day of inspiral. On the other hand, the slow modulation picture suggests just the contrary: not much improvement is expected at late times when there is effectively very little modulation (Finn & Larson 2005, private communication).

2. Does the introduction of additional high frequency components in the signal have any effect on the estimations of low frequency parameters?

In the GW context, it is of general interest to determine under what circumstances additional high frequency signal components, such as higher order post-Newtonian corrections or spin-induced effects, remain decoupled from the determination of angular and distance information based on the signal amplitude modulation.

3. Are there combinations of signal parameters for which errors improve rapidly in the last days of observation? If so, what are these combinations? What determines how many such rapidly–improving combinations there will be?

   If the distance $d_{\rm L}$ correlates with the angles, then in principle the volume of the 3D error box can be much smaller than the product of the marginalized errors $\delta\Omega \times \delta d_{\rm L}$ would imply. Unfortunately, in practice, this is unlikely to help to reduce the number of false counterparts, because the δz error will be dominated by weak lensing (Kocsis et al., 2006).

4. How does the width of parameter error distributions evolve with time? Are the best and worst cases approaching the typical case prior to the final days of observation? How do I expect the eccentricity of localization error ellipsoid to evolve with time for LISA?

Here, I restrict the discussion to a brief summary of my findings and direct the reader to Appendix A.1 for further details on these toy models.

The parameter estimation uncertainties are defined by the correlation error matrix. For N_p parameters, this defines an N_p-dimensional error-ellipsoid in the N_p-dimensional parameter space, where parameters are constrained at a given confidence level. Marginalized errors for a given parameter are then related to the projection of this ellipsoid on the basis vector corresponding to that parameter. Since the principal axes of this error ellipsoid are generally not aligned with the original parameters, the marginalized errors can be substantial even if the volume of the error ellipsoid is close to zero. This happens if the ellipsoid is very "thin" but has a large size in at least one direction. Diagonal elements of the correlation matrix provide marginalized squared errors on the parameters, while eigenvalues provide squared errors along the principal axes.

I consider three versions of toy signals to understand how a particular harmonic mode contributes to the time-dependence of parameter uncertainties and to find answers to Questions 1–4 above. I start with the simplest toy model and refine this model by adding more details and complexity in the successive models. In each case, I discuss general implications for the model under consideration.

Basic toy model

In my basic toy model, I assume that the true signal is comprised of a constant carrier signal, which is modulated by a single known-frequency cosine, $f_\oplus$:

$$h(t) = c_0 + c_1 \cos(2\pi f_\oplus t), \tag{3.64}$$

where c_0 and c_1 are unknown parameters to be estimated. I assume that the noise level is rapidly decreasing during the observation, mimicking the gradual increase in the instantaneous signal-to-noise ratio for LISA inspiral signals. The contradictory statements made in relation to Question 1 above can be explored with this model. I find that marginalized parameter errors scale with the signal-to-noise ratio far away from merger (i.e. $t_\mathrm{f} \gtrsim 0.1 f_\oplus^{-1}$) but they quickly converge to their final values at late times, even though the signal-to-noise ratio keeps accumulating. It is possible to derive analytical formulae for the evolution of parameter errors to fully characterize this behavior (see Appendix A.1). I find that, even though the error ellipse rapidly decreases in volume, as the inverse of the signal-to-noise ratio near merger, the error ellipse only shrinks along one of its dimensions, the semi-minor axis, so that a non-negligible residual uncertainty remains in the orthogonal subspace (e.g. along the semi-major axis). This residual uncertainty carries over to final marginalized errors for both parameters. Therefore, this first toy model verifies the second option in relation to Question 1.: there is no late improvement because there is very little effective signal modulation, making the signal-to-noise argument largely irrelevant. However, I find below that this model does not carry some essential features of the LISA signal which modify somewhat my final answer to Question 1 (see final toy model below).

Second toy model

In my second toy model, I modify the single frequency signal by postulating two pairs of unknown amplitudes and phases for two different *a priori* known frequencies, satisfying $f_2 \gg f_1$, which modulate an otherwise constant signal:

$$h(t) = c_0 + s_1 \sin(2\pi f_1 t) + c_1 \cos(2\pi f_1 t) + s_{10} \sin(2\pi f_2 t) + c_{10} \cos(2\pi f_2 t). \tag{3.65}$$

The number of unknowns in this model is five: c_0, s_1, c_1, s_{10} and c_{10} are the coefficients of the functions 1, $\sin(2\pi f_1 t)$, $\cos(2\pi f_1 t)$, $\sin(2\pi f_2 t)$, and $\cos(2\pi f_2 t)$. Again, I assume that the noise decreases quickly with time before merger, at $t = 0$. This model is designed to answer my Question 2 above. In this case, I find that parameter errors are correlated only with unique frequency components and the constant signal, all the way to $t_\mathrm{f} \gtrsim 0.1 f_2^{-1}$. The model thus demonstrates how components associated with very different variation timescales can decouple from each other. Moreover, as for the first toy model, I find that marginalized parameter errors effectively stop improving past a finite time before merger (Question 1), which is simply related to their respective frequencies. As a result, a nonzero residual error remains again, even though the signal-to-noise ratio continuously increases near merger.

Final toy model

In my final toy model, I insert a few additional features essential to a realistic LISA data-stream. Firstly, I assume 5 low-frequency harmonics, 1, $\sin(2\pi f_1 t)$, $\cos(2\pi f_1 t)$, $\sin(4\pi f_1 t)$, $(\sin 4\pi f_1 t)$, with unknown amplitudes. I also include a high frequency carrier signal with known frequency, $f_2 \gg f_1$, but unknown amplitudes in $\sin(2\pi f_2 t)$ and $\cos(2\pi f_2 t)$, for a total of seven free parameters. Secondly, I note that the LISA system is equivalent to two orthogonal arm interferometers with both detectors measuring polarization phases simultaneously (which correspond to the real and imaginary parts of the amplitude modulation, § 3.4). Therefore, the signal is comprised of 4 simultaneous data-streams. I incorporate this feature by assuming 4 measurements (i.e. 4 corresponding Fisher matrices) of the signal with 4 given phase shifts $(\varphi_i^{s1}, \varphi_i^{c1}, \varphi_i^{s2}, \varphi_i^{c2}; 1 \leq i \leq 4)$ so that

$$\begin{aligned} h(t) \quad = \quad & c_0 + s_1 \sin(2\pi f_1 t + \varphi_i^{s1}) + c_1 \cos(2\pi f_1 t + \varphi_i^{c1}) \\ & + s_2 \sin(2\pi f_1 t + \varphi_i^{s2}) + c_2 \cos(2\pi f_1 t + \varphi_i^{c2}) \\ & + s_{10} \sin(2\pi f_2 t) + c_{10} \cos(2\pi f_2 t), \end{aligned} \tag{3.66}$$

In this case, I find that 4 principal components improve quickly at late times. As in my second toy model, the high frequency parameters decouple from the slow frequency ones, except at very late times when $t_\mathrm{f} \gtrsim 0.1 f_2^{-1}$.

This final toy model allows us to answers all of Questions 1-4 as follows.

- Answer 1: Four out of 5 slow principal components of the error ellipsoid are quickly improving with time, while one of them stops improving at $t_\mathrm{f} \lesssim 0.1 f_1^{-1}$. Therefore, any parameter with a large projection along this one poor principal component will stop improving, while parameters nearly orthogonal to it will keep improving quickly. Thus, both statements made in relation to Question 1 above can in fact be correct, depending on the connection between a given parameter and the poor principal component. Typically, I expect marginalized parameter uncertainties to evolve as $(S/N)^{-1}$ for $t_{\rm f} \gtrsim 0.1 f_1^{-1}$. For smaller $t_{\rm f}$ values, closer to merger, they would continue to improve, albeit with a shallower slope.

- Answer 2: I find that the introduction of additional high frequency components does not change the evolution of original parameter estimations as long as the time-to-merger is larger than a fraction of the time period of the additional high frequency components.

- Answer 3: As the signal-to-noise ratio increases quickly at late times, rapidly evolving parameter error combinations are given by the principal components of the error ellipsoid corresponding to the final situation at merger. With 4 data-streams, there are 4 such best principal components. Analogously, for the LISA amplitude modulation given by eq. (3.25), I expect that the 2 polarization phases for the 2 beam patterns at ISCO can be best determined: $(1+\cos^2\theta_{NL})F_+^{I,II}(\Omega_{\rm ISCO})$ and $\cos\theta_{NL}F_\times^{I,II}(\Omega_{\rm ISCO})$. (In terms of ecliptic angular variables, these are the real and imaginary parts of the combination given by eq. (3.34).)

- Answer 4: The widths of error distributions for slow parameters do not change significantly as long as $t_{\rm f} \gtrsim 0.1 f_1^{-1}$. During this final stretch of time before merger, however, one of the principal components stops improving and the major axis of the error ellipsoid freezes. Since the physical parameters can be considered to be randomly oriented with respect to the ellipsoid axes, distributions of marginalized errors suddenly start broadening for $t_{\rm f} \lesssim 0.1 f_1^{-1}$, with a worst case relative orientation leading to very little improvement and a best case relative orientation corresponding to a scaling with $(S/N)^{-1}$.

3.6.2 Implications for LISA

These simple toy models offer a general interpretation of the time dependence of LISA's parameter estimation errors for source localization. The LISA data stream is described by $N_{p1} = 5$ physical parameters, $\boldsymbol{p}_{\rm slow}$, which are not the harmonic coefficients themselves but determine these coefficients, g_j (or conversely, the mode expansion coefficients g_j

determine the physical parameters $\boldsymbol{p}_{\rm slow}$; see § 3.3). Neglecting Doppler phase and spin precession effects, $2J_{\max}+1=9$ modes determine the signal by eqs. (3.41,3.42). In principle, any $N_{p1}=5$ of the g_j mode amplitudes uniquely determine the physical parameters, $\boldsymbol{p}_{\rm slow}$. However, in the presence of noise, each of these modes are uncertain and the combination of all modes helps in reducing the estimation errors of the $\boldsymbol{p}_{\rm slow}$ variables.

The key implication of my toy models for LISA is that the estimation of low frequency g_j modes with low $|j|$ are effectively decoupled from the high frequency signal, unless the merger is within ~ 0.1 times the cycle time of the fast-oscillating signal. I have shown that the HMD of the orbital modulation consists purely of low-order harmonics, with $|j|\leq 4$. In comparison, the high frequency GW phase has a much higher frequency, corresponding to $j>1000$, and this high frequency signal's cycle time is greater than the time to merger throughout $t\gtrsim t_{\rm ISCO}$. Hence, physical parameters $\boldsymbol{p}_{\rm slow}$ will remain decoupled from parameters $\boldsymbol{p}_{\rm fast}$, all the way to ISCO. This finding is independent of details of the waveform and the modulation, in agreement with the results of Berti et al. (2005b) which show that decoupling occurs independently of the details of the $h_{\rm c}(t)$ signals, including the modified inspiral waveforms of alternative theories of gravity. In terms of post-Newtonian expansions, only terms above second order have cycle times as large as the cycle time of the amplitude modulation. These terms are responsible for the small cross-correlations of the two sets of parameters found by Hughes (2002a).

In this work, I have not considered spin precession effects, but Vecchio (2004) and Lang & Hughes (2006) find that spin precession effects can help improve the final localization errors by a factor of ~ 3. Spin precession cycle times decrease continuously, become of order a few days or less during the last week prior to merger, and of order hours during the last day of inspiral. Therefore, according to my simple models, I expect spin precession effects to improve the source parameter estimation errors especially during the final two weeks before ISCO. During that period of time, in the absence of spin effects, parameter uncertainties (especially the sky position major axis and the luminosity distance) cease to improve when using only the amplitude modulation.

The best-determined parameters at ISCO are, approximately, the independent detector outputs at ISCO. These are the real and imaginary parts of $h_1^{\rm I,II}(p_1)$, i.e. $d_{\rm L}^{-1}(1+\cos^2\theta_{NL})F_+^{I,II}(\Omega)$ and $d_{\rm L}^{-1}\cos\theta_{NL}F_\times^{I,II}(\Omega)$ (see Appendix A.1.4). These are the 4 independent combinations of 5 physical parameters p_1 which correspond to the eigenvectors of the error covariance matrix following the steep evolution $\propto (S/N)^{-1}$ all the way to ISCO. I refer to the fifth independent combination, which is orthogonal to these best eigenvectors, the "worst" eigenvector, since for this combination, the evolution ceases to improve as $(S/N)^{-1}$ within $\sim 0.1\times$ (amplitude modulation cycle time) of merger. It is straightforward to obtain this worst combination explicitly by using the 4 other eigenvectors and Gram-Schmidt orthogonalization (but I have not done this in practice). Since the highest frequency harmonic of the slow modulation is for $j = 4$, the corresponding cycle time is yr/4. Thus, I expect errors will stop improving roughly 1–2 weeks prior to merger. Distributions of errors will quickly broaden during these final stages of observation before ISCO. Simply scaling errors with $(S/N)^{-1}$, as in the angle-averaged formalism (e.g. Berti et al., 2005b; Kocsis et al., 2006), is acceptable if one studies the evolution of parameter errors at $t_{\rm f} \gtrsim 2$ weeks, or if one only focuses on the best case parameter combinations. In general, the exponent in the (S/N) scaling decreases as one approaches merger time depending on how close the particular combination of angles considered is to the worst combination.

My findings for the eccentricity evolution of LISA's sky localization error ellipsoid can also be understood with the simple toy models. In fact, I found this behavior to be expected for any model signal with relative instantaneous signal amplitude increasing quickly with time, e.g. $t^{-\alpha}$, $\alpha \gtrsim 2$. In this case, the principal axes of the general parameter error ellipsoid separate near $t_{\rm f} = 0$. There are a limited number of principal errors which rapidly decrease to zero near $t_{\rm f} = 0$, while others "freeze out" at a time related to a fraction of the cycle time of the particular waveform ($\sim 0.1 T_{\rm cycle}$ if $t_{\rm i} > T_{\rm cycle}$). For LISA, there are 5 variable parameters, $\boldsymbol{p}_{\rm slow} = (d_{\rm L}, \theta_N, \phi_N, \theta_L, \phi_L)$, and estimation uncertainties of 4 combinations of these parameters, $d_{\rm L}^{-1}(1+\cos^2\theta_{NL})F_{+}^{I,II}(\Omega), d_{\rm L}^{-1}\cos\theta_{NL}F_{\times}^{I,II}(\Omega)$, improve quickly with $(S/N)^{-1}$. These combinations correspond to the best 4 principal axes of the 5-dimensional error ellipsoid. The remaining $5^{\rm th}$ principal axis does not improve as $(S/N)^{-1}$, but rather stops improving at a fraction of the last modulation cycle time. The two dimensional sky position error ellipsoid is the projection of the general 5-dimensional error ellipsoid on the (θ_N, ϕ_N) plane. This plane will generally not be aligned with the principal axes of the 5-dimensional ellipsoid. In a typical case, therefore, there will be a nonzero projection on the worst principal component and the sky position ellipsoid will stop shrinking along the worst principal component. This explains why the major axis, $2a$, ceases to improve and the eccentricity increases close to merger.

According to this argument, it is somewhat surprising to find that the minor axis, $2b$, can stop improving much before ISCO. Figure 3.2 shows that this happens in the worst 10% of all cases for randomly chosen source angular parameters. The reason for this is that, in some cases, not all rapidly improving "best" principal components have a small absolute error at ISCO. For example, consider an edge-on binary inspiral ($\cos\theta_{NL} \approx 0$). Since two of the quickly improving parameters are simply proportional to $\cos\theta_{NL}$, the errors will be very large for these parameters. Thus, depending on the relative orientation of the detector and the source at ISCO, there can be large absolute errors in some cases even for the best combinations of parameters. In short, both axes of the sky position error ellipsoid can stop improving at late times in those cases when LISA is oriented in its least favorable direction at ISCO.

3.7 Conclusions

I have developed a new harmonic mode decomposition (HMD) method to study the feasibility of using LISA inspiral signals to locate coalescing SMBH binaries in the sky, as the mergers proceed. According to my extensive HMD survey of potential LISA sources, it will be possible to trigger large field-of-view searches for prompt electromagnetic counterparts during the final stages of inspiral and coalescence. My results indicate, for instance, that for a typical $z \sim 1$ merger event with total mass $M \sim 10^5 - 10^7 \mathrm{M}_\odot$, a 10-day advance notice will be available to localize the source to within a $10\,\mathrm{deg}^2$ region of the sky. The advance notice to localize the source to a 10 times smaller area of $1\,\mathrm{deg}^2$ is < 1 day for the typical event, suggesting that a wide–field instrument of the LSST class, with a $10\,\mathrm{deg}^2$ field-of-view, may offer significant advantages over a smaller, $1\,\mathrm{deg}^2$ field-of-view instrument for observational efforts to catch prompt electromagnetic counterparts to SMBH binary inspirals.

The robust identification of such electromagnetic counterparts would have multiple applications (Holz & Hughes, 2005; Kocsis et al., 2006), from an alternative method to measure cosmological parameters to precise measurements of merger geometries in relation to host galaxy properties. If such electromagnetic counterpart searches can be implemented effectively and successfully, LISA could become an extremely valuable instrument for astrophysics and cosmology, beyond the original general relativistic measurement goals. Given the advance warning time capabilities established here, effective strategies for electromagnetic counterpart searches, including the concept of partially dedicating a $\gtrsim 10\,\mathrm{deg}^2$ field-of-view fast survey instrument of the LSST class, are considered in detail in a separate investigation (Kocsis et al., 2007).

Chapter 4

Detection Rate Estimates of Parabolic Encounters

4.1 Introduction

Interferometric gravitational-wave (GW) detectors LIGO, GEO, TAMA, and VIRGO are searching for GW signals with unprecedented sensitivity (Abbott et al., 2005a,b,d; Acernese et al., 2005; Ando, 2005; Grote et al., 2005; Hughes et al., 2001). For LIGO, the noise levels are already reaching the goal level necessary for the detection of the strongest signals. It is very important to analyze the detection capabilities of these detectors and to estimate the rates of potentially detectable GW signals. There is already a considerable list of possible detection candidates (for a review see Cutler & Thorne, 2002): the inspiral of neutron star (NS) or black hole (BH) binaries, the tidal disruption of NS by BH in NS–BH binaries, BH–BH merger and ringdown, low-mass X-ray binaries, pulsars, centrifugally hung-up proto neutron stars in white dwarf accretion-induced collapse, supernova core collapse, gamma ray bursts, and the stochastic background. Here, I consider an additional possibility, GWs produced by unbound orbits. As I will show, among unbound orbits near-parabolic encounters (PEs) produce gravitational radiation with typical frequencies appropriate for detection with terrestrial facilities. For close PEs the gravitational radiation is short and intensive, that is observable to large distances. Here, I estimate the expected event rate of detections for specific current and near-future GW detectors.

Initial order-of-magnitude estimates on the detectability of GWs emitted during scattering and near collisions of stellar mass compact objects in active galactic nuclei and globular clusters (GCs) were made by Dymnikova et al. (1982). Although their study primarily focused on BH–star, star–star encounters, and did not provide numbers for BH–BH encounters, they identified these encounters to be "quite rare". However, Dymnikova et al. (1982) used an overly simplified GC model in which the velocities and masses of all objects were identical, and the spatial distribution was assumed to be homogeneous. I extend the detection rate estimates to account for the stellar BH mass function, mass segregation, and mass-dependent relative velocities. I show that this improvement significantly increases the event rate, by approximately a factor of 10^2. In addition, interferometric GW detector technology has improved greatly and detailed sensitivity curves are now available. Dymnikova et al. (1982) estimated a maximum visible distance of $D_{\max} = 20$Mpc, which is a factor of ~ 100 less than Advanced LIGO's (AdLIGO) capabilities (see Figure 4.4 below), i.e. a factor of $\sim 10^6$ less in the accessible volume of sources. Combining these factors, my detection rate estimates yield $\sim 10^8$ times larger results for AdLIGO.

Gravity waves emitted during PEs are also important for creating relativistic orbits by gravitational radiation reaction around the supermassive black holes (SMBH) in the centers of galaxies. The GWs emitted by the later inspiral of the star or compact object around the SMBH are possibly detectable by the future space detector *LISA* (Freitag, 2003; Gair et al., 2004; Sigurdsson & Rees, 1997) and also by ground-based detectors for highly eccentric orbits (Hopman & Alexander, 2005). Here, I do not consider encounters with SMBHs, but focus on the direct detection of GWs from unbound orbits of two stellar mass compact objects (COs).

Stellar mass unbound orbit encounters are expected to be most likely from dense star clusters with a large fraction of COs. Among regular star systems, these features are carried by galactic nuclei and GCs, where central densities reach $10^4 - 10^7\,\mathrm{pc}^{-3}$ within a region of $0.5 - 3\,\mathrm{pc}$ (Pryor & Meylan, 1993), the inner regions contain a CO fraction of $q \gtrsim 1/2$ (Sigurdsson & Phinney, 1995). Here, I estimate PE event rates for GCs.

As compared to other GW burst sources, the big advantage in detecting PE events is that the possible signal waveforms are much more reliable as the physics behind them is well understood. The waveforms are known analytically for the case of arbitrary masses moving with arbitrary velocities but at small deflection angles (often referred to as gravitational bremsstrahlung, see Kovacs & Thorne 1978), arbitrary unbound orbits but low velocities in the Newtonian approximation (Turner, 1977), in the post-Newtonian approximation (PN, Blanchet & Schafer, 1989, including corrections $\mathcal{O}(v^2)$), in the 2PN approximation ($\mathcal{O}(v^4)$ Blanchet et al., 1995; Mikoczi et al., 2005), and most recently, in the 3PN approximation (Blanchet et al., 2005, $\mathcal{O}(v^6)$), and the exact numerical solution is available for extreme mass ratios using a Schwarzschild background approximation (Martel, 2004), and finally, for head-on collisions with large velocities (D'eath & Payne, 1992). Thus, PE waveforms are available for a very large portion of the parameter space. Waveform templates can be constructed a priori, similar to inspirals. The prior knowledge of the possible waveforms allows the method of matched filtering detection, which helps to reduce the minimum signal-to-noise ratio necessary for a confirmed detection (Flanagan & Hughes, 1998).

This chapter is organized as follows. In Section 4.2, I summarize the relevant characteristics of interferometric GW detectors. In Section 4.3, I review the PE waveforms that I adopt. In Section 4.4, I describe the population models that are necessary to estimate the scalings of parameters and the overall PE event rates. In Section 4.5, I derive the expected number of PE event rates, calculate their maximum distance of detection, and estimate the implied rates of successful detections. Finally, in Section 4.6 I summarize the conclusions and in Section 4.7 discuss the limitations and the implications of this work.

4.2 Overview of Gravitational-wave Detectors

The new generation of GW detectors rely on interferometric monitoring of the relative (differential) separation of mirrors, which play the role of test masses, responding to space-time distortions induced by the GWs as they traverse the detectors. The effect of a GW is to produce a strain in space, which displaces the mirrors at the ends of the arms by an amount proportional to the effective arm length and GW strain. For GWs incident normal to the plane of the detector, and polarized along the arms of the detector, the mirrors at the ends of the two arms experience differential motion. Waves incident from other directions and/or polarizations also induce differential motion, albeit at a smaller level.

Presently, there is an operational international network of first generation interferometric GW detectors: InLIGO, VIRGO, TAMA, and GEO (see Section 4.1 for references). The design of advanced terrestrial GW detector AdLIGO and space detector *LISA* is well on the way. There are also plans for a new generation of low-frequency underground detectors especially sensitive for lower frequencies (DeSalvo, 2004), which might be especially sensitive to PEs, which I will discuss in a followup work in detail. Finally, there are plans for possible future improvements of space detectors: *Decihertz Interferometric Gravitational-wave Observatory (DECIGO)* (Seto et al., 2001), *Advanced Laser Interferometer Antenna (ALIA)* and the *Big Bang Observer (BBO)* (Crowder & Cornish, 2005). Their sensitivities, detection frequency bands and capabilities are quite different. For my purposes, a good approximation is to use: (1.) the InLIGO and VIRGO sensitivity goal (nearly reached) to assess present capabilities; (2.) the AdLIGO sensitivity goal to assess future capabilities of ground based detectors; (3.) the *LISA* sensitivity goal to assess future capabilities of initial space based detectors; and (4.) the *Next Generation LISA* sensitivity goal to assess the capabilities of possible further extensions to space detectors.

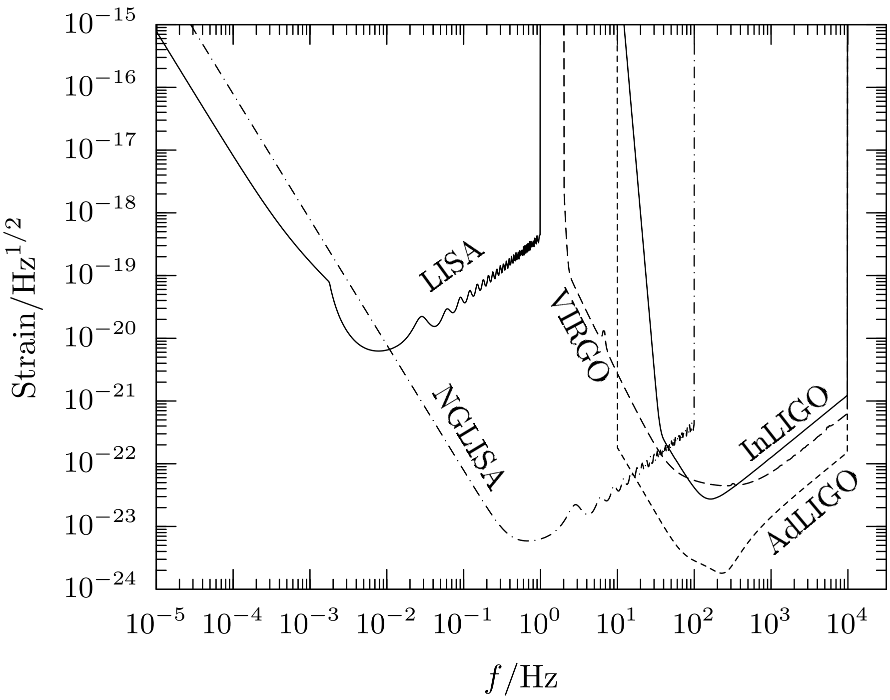

Figure 4.1 Goal sensitivity curves for interferometric GW detector facilities: InLIGO, VIRGO, AdLIGO, *LISA*, and *NGLISA*.

The goal RMS noise density per frequency interval for the various detectors, including instrumental and confusion noise, is plotted on Figure 4.1. For LIGO I adopt Abbott (2004), for VIRGO I adopt Acernese et al. (2005) but for simplicity discard the narrow features[1], for AdLIGO I adopt the noise estimates from its website[2], and for *LISA*, I

[1]http : //www.virgo.infn.it/senscurve/
[2]http : //www.ligo.caltech.edu/advLIGO/scripts/ref_des.shtml

utilize the online sensitivity curve generator [3] for the instrumental noise, and adopt the confusion noise estimate from Barack & Cutler (2004b). The noise levels of possible extensions to *LISA* named the "Next Generation *LISA*" (*NGLISA*) are also provided by the sensitivity curve generator, which I also include in all of my calculations. This is very similar to the planned sensitivity curve of *DECIGO* (Seto et al., 2001, see the more conservative case therein) and is just halfway between *ALIA* and *BBO* (Crowder & Cornish, 2005, a factor of 3 difference in sensitivity from both).

4.3 Parabolic Encounter Waveforms

The GW signal waveform for PE is available in a wide range of approximations (see Section 4.1). I adopt Turner (1977) for the angular averaged waveforms, for which the interacting masses travel on classical Newtonian trajectories and emit quadrupole radiation. Other features such as spin-spin, spin-orbit interactions, and gravitational recoil, etc., are higher order perturbations which carry only a small total signal power in typical cases. Therefore for the sake of calculating the signal-to-noise ratio, it is a sufficient first-order approximation to use these waveforms.

Illustrative examples of PE waveforms can be found in Turner (1977) (see Fig. 4 and 7 therein). The waveforms are generally constituted of a large amplitude single peak or a jump in the time domain with characteristic time scale t_0, related to the relative angular velocity at the minimum separation $\omega_0 = v_0/b_0 = 1/t_0$. Here v_0 is the relative velocity at the closest point, and b_0 is the corresponding minimum separation. Turner (1977) provides a closed analytical formula for the total GW radiation energy spectrum $\mathrm{d}E/\mathrm{d}f$. The spectrum is wide-band, for parabolic orbits it is zero at $f = 0$, it has a maximum near $f_0 = \omega_0/2\pi$ and a half-width $\sim 1.5 f_0$.

The characteristic signal amplitude is obtained from the GW energy spectrum as (Flanagan & Hughes, 1998; Thorne, 1987)

$$h(f) = \frac{\sqrt{3}}{2\pi}\frac{\mathrm{G}^{1/2}}{\mathrm{c}^{3/2}}\frac{1+z}{d_{\mathrm{L}}(z)}\frac{1}{f}\sqrt{\frac{\mathrm{d}E}{\mathrm{d}f}[(1+z)f]}, \tag{4.1}$$

where z is the redshift, $d_{\mathrm{L}}(z)$ is the cosmological luminosity distance (Eisenstein, 1997), and $\mathrm{d}E/\mathrm{d}f\ [(1+z)f]$ is the total GW emitted energy of the source at the emitted

[3] http : //www.srl.caltech.edu/ ∼ shane/sensitivity/

frequency. The orientation averaged signal-to-noise ratio is

$$\left\langle \frac{S}{N} \right\rangle = \sqrt{\frac{4}{5} \int_0^\infty \frac{|h(f)|^2}{S_\mathrm{n}(f)^2} \,\mathrm{d}f} \tag{4.2}$$

where $h(f)$ is the characteristic signal amplitude, equation (4.1) and $S_\mathrm{n}(f)$ is the one-sided spectral noise density (see Section 4.2 for references for the particular detectors). Note that equation (4.2) refers to an angle-averaged SNR obtained from the cube-root of an average of cubed signal amplitudes over different possible orientations of the source and interferometer. Since event rates roughly scale with volume, i.e. distance cubed or $(S/N)^{-3}$, this prescription is useful for estimating event rates (Thorne, 1987). For signals with optimal orientations, the coefficient $4/5$ in equation (4.2) is changed to 4. Note furthermore, that the $4/5$ factor is applicable for the detection rate using a single interferometric GW detector. There are already 4 interferometric GW detectors on Earth (see Section 4.2), and it is possible that there will be a lot more in the future. A coincident analysis with multiple detectors can be used to improve the efficiency by increasing the total signal-to-noise ratio and also by insuring that at least one detector is close to the optimal orientation (Jaranowski et al., 1996). For this reason, the coefficient $4/5$ in equation (4.2) is most likely pessimistic. For 1 detector in the optimal orientation and $K-1$ identical detectors in random orientations a quick scaling of the coefficient is $\sim 4 + (4/5)(K-1)^{1/2}$. On the other hand, a relatively large SNR might be required to keep the false alarm rate at a sufficiently low level. For a conservative estimate on the PE rate I do not modify the $4/5$ factor in the definition of SNR and evaluate results for $\mathrm{SNR} = 5$.

The PE waveforms can be obtained from equation (4.1) by substituting the $E(f)$ relationship specific for PEs using Turner (1977):

$$h(f, f_0) = \frac{\sqrt{85}\,\pi^{2/3}}{2^{5/3}} \frac{\mathrm{G}^{5/3}}{\mathrm{c}^4} \frac{\mathcal{M}_z{}^{5/3}}{d_\mathrm{L}} \frac{f_{0z}^{2/3}}{f} \sqrt{F(f/f_{0z})} \tag{4.3}$$

where $\mathcal{M}_z = (1+z)(m_1 m_2)^{3/5}/(m_1+m_2)^{1/5}$ is the redshifted chirp mass if m_1 and m_2 are the masses of the interacting objects, $f_{0z} = f_0/(1+z)$ is the redshifted characteristic frequency, f denotes the observed GW frequency, and $F(x)$ is the Turner (1977) normalized dimensionless energy spectrum for dimensionless frequency $x = f/f_{0z}$, for which $\int_0^\infty F(x)\,\mathrm{d}x = 1$.

Equation (4.3) is the leading order (i.e. Newtonian) approximation to the GW waveform, $h(f, f_0)$. A remarkably advantageous feature of the waveform in this approximation is that it depends on only a single combination of the orbital parameters, f_{0z}. Although I need only utilize this form, equation (4.3), I briefly note that it is also possible to express the waveform with the separation at closest point b_0 in the center of mass frame (Turner, 1977):

$$h(f, b_0) = \frac{\sqrt{85}}{4} \frac{\mathrm{G}^2}{\mathrm{c}^4} \frac{(1+z)\, m_1 m_2}{d_\mathrm{L}\, b_0} \frac{1}{f} \sqrt{F[f/f_{0z}(b_0)]}. \tag{4.4}$$

Here $f_{0z}(b_0)$ is the redshifted characteristic frequency for fixed initial velocity as a function of b_0. The GW amplitude spectrum $h(f, b_0)$ is roughly flat at low frequencies $f < f_{0z}$, and decreases for higher frequencies. Equation (4.4) shows that $h(f, b_0)$ scales with b_0^{-1} for frequencies larger than the cutoff at $\sim f_{0z}$.

Modifications are necessary for relativistic encounters. The relativistic gravitational radiation waveforms and energy output has been calculated by Martel (2004) in the quadrupole approximation for a test particle approaching a Schwarzschild black hole from infinity on a quasi-parabolic geodesic[4]. In case the periastron distance b_0 is close to the unstable circular orbit, the GW energy is significantly increased (it has a logarithmic singularity at $\lambda = 2$, where $\lambda \equiv b_0/R_\mathrm{SH}$ and R_SH is the total Schwarzschild radius, and a factor of ~ 10 increase for $\lambda = 2.01$ or a factor of 2 for $\lambda = 3$). I adopt the fitting formula of Gair et al. (2005), which is correct within 0.1% for orbits that avoid a collision, and scale the amplitudes of the Turner (1977) waveforms equation (4.3) according to the increase of the GW energy, $E_\mathrm{rel}(\lambda)/E_\mathrm{nr}(\lambda)$.

$$h(f, f_0) = \frac{\sqrt{85}\, \pi^{2/3}}{2^{5/3}} \frac{\mathrm{G}^{5/3}}{\mathrm{c}^4} \frac{\mathcal{M}_z{}^{5/3}}{d_\mathrm{L}} \frac{f_{0z}^{2/3}}{f} \sqrt{F\left(\frac{f}{f_{0z}}\right)} \sqrt{\frac{E_\mathrm{rel}(\lambda)}{E_\mathrm{nr}(\lambda)}} \tag{4.5}$$

Note once again, that the dimensionless periastron distance, λ, is uniquely specified by the characteristic frequency, f_0. I derive explicit formulae for $f_0(\lambda)$ in the non-relativistic Newtonian and relativistic geodesic approximations, when considering the dynamics of PEs in Section 4.5.1 and Section 4.5.2 below. Quite remarkably, the characteristic frequency of the waveform is unchanged for relativistic orbits. Therefore, I do not explore the effects of relativistic modifications in the shape of the GW signal waveform, I restrict only to correcting the amplitude.

[4]I continue to denote as "quasi-parabolic" or simply "parabolic" encounters that have asymptotically zero velocity at infinity. Note that the trajectories are generally quite different from parabolas in the highly relativistic regime (for illustration, see Martel, 2004).

4.4 Population Models

The major contribution to the PE event rate is expected from dense star clusters with a large CO fraction. The most important systems carrying these properties are possibly GCs and galactic nuclei. Here, I focus on GCs, but simple analytical scaling of the results allows a straightforward extension to galactic nuclei or any other population of spherical star systems.

The spatial distribution of GCs exactly traces the distribution of galactic halos (Chandar et al., 2004) in the local universe. In this section I summarize the galaxy distribution and the GC abundance per galaxy, and describe the GC models which I adopt.

4.4.1 Galaxy Distribution

I utilize the local distribution of galaxies (Tully, 1988). The accumulated number of galaxies to distance D can be well approximated by

$$N^{\rm gal}(D) = \begin{cases} N_1\ (D/{\rm Mpc})^{0.9} & \text{for}\ \ D \leq 3{\rm Mpc} \\ N_2\ (D/3{\rm Mpc})^{1.5} & \text{for}\ \ 3{\rm Mpc} < D < 16{\rm Mpc} \\ N_3\ (D/16{\rm Mpc})^{2.4} & \text{for}\ \ 16{\rm Mpc} < D < 60{\rm Mpc} \\ N_4\ (D/60{\rm Mpc})^{3} & \text{for}\ \ D > 60{\rm Mpc} \end{cases}, \tag{4.6}$$

where N_1, N_2, N_3, and N_4 are 23, 62, 1100, and 26000, respectively. The average density of faraway galaxies is $0.03{\rm Mpc}^{-3}$, but the local galaxy abundance is much denser than average. In equation (4.6) $N^{\rm gal}(D)$ has a 45% jump at the Virgo cluster at $D = 16{\rm Mpc}$.

4.4.2 Globular Cluster Abundance

Following Portegies Zwart & McMillan (2000), I adopt $\bar{n}^{\rm gc} = 2.9{\rm Mpc}^{-3}$ for the average GC abundance in the universe. I roughly account for the clustering of GCs in the local universe by assuming that the distribution of GCs follow the abundance of galaxies. This assumption is consistent with observations (Chandar et al., 2004; Goudfrooij et al., 2003) suggesting that the population of GCs represent a universal, old halo population that is present around all galaxies. The number of GCs within a distance D is then

$$N^{\rm gc}(D) = y^{\rm gc} N^{\rm gal}(D), \tag{4.7}$$

where $y^{\rm gc}$ is a scaling constant relating the abundance of GCs and galaxies. Using the large scale average $\bar{n}^{\rm gc} = 2.9{\rm Mpc}^{-3}$ (Portegies Zwart & McMillan, 2000) and $\bar{n}^{\rm gal} = 0.029{\rm Mpc}^{-3}$ equation (4.6) for $D > 60{\rm Mpc}$ I get $y^{\rm gc} = 100$. Alternatively, $y^{\rm gc}$ can be interpreted as the number of GCs per galaxy averaged over all morphological types. Concerning PE detection rates, I shall show in Section 4.5.3 that typical observation distances for terrestrial detectors are larger than the clustering scale given by equation (4.6). Therefore, the results are sensitive to mainly the average abundance and are only slightly increased by the local clustering of GCs.

The value $\bar{n}^{\rm gc} = 2.9{\rm Mpc}^{-3}$ for the average abundance is a conservative assumption. In their quick estimate Portegies Zwart & McMillan (2000) derived this value by adding up the contribution of galaxies of morphological types Sab, E-S0, and blue ellipticals. Recently, 12 nearby edge on spiral galaxies were examined, resulting in much larger numbers, reaching $\sim 1000 - 1300$ GCs for these particular galaxies (Chandar et al., 2004; Goudfrooij et al., 2003). In addition to the morphological types considered in Portegies Zwart & McMillan (2000), dwarf elliptical (dE) galaxies also contribute to the overall GC numbers (van den Bergh, 2006). The GC content of 69 dwarf elliptical (dE) galaxies have been estimated to host about a dozen GCs per dE galaxy (Lotz et al., 2004). Therefore, my results on detection rates correspond only to lower limits, which has to be scaled linearly with $\bar{n}^{\rm gc}$ when more detailed estimates become available.

The GC distribution given by equations (4.6–4.7) is only valid for sub-cosmological scales. Assuming that D denotes the luminosity distance, $d_{\rm L}$, in equations (4.6–4.7) which is a direct observable using the GW amplitude, the change in the cosmological volume element decreases the average density.

$$N^{\rm gc}(d_{\rm L}) = 4\pi \int_0^{z(d_{\rm L})} \frac{\partial V}{\partial z\, \partial\Omega} y^{\rm gc} \bar{n}^{\rm gal}\, {\rm d}z \tag{4.8}$$

I adopt the cosmological volume element (Eisenstein, 1997) for a ΛCDM cosmology with $(\Omega_m, \Omega_\Lambda, h) = (0.3, 0.7, 0.7)$ consistent with recent observations of the *Wilkinson Microwave Anisotropy Probe* and the Sloan Digital Sky Survey (Tegmark et al., 2004b). I find that the uncorrected volume element $d_{\rm L}^2 {\rm d}\Omega {\rm d}d_{\rm L}$ is reduced by a factor of 0.7 for $z = 0.1$ ($d_{\rm L} = 0.5\,{\rm Gpc}$) and by a factor of 0.053 for $z = 1$ ($d_{\rm L} = 7\,{\rm Gpc}$). Since GCs are believed to represent an old halo population in galaxies, I do not account for additional possible cosmological evolution of the comoving GC abundance.

4.4.3 Globular Cluster Models

Here I define the GC models that I use to obtain typical PE parameters and event rates. First I define the common features that are the same for both of my models. I assume a total of $N^{\rm tot}$ stellar mass stars, $m_{\rm star} = \mathrm{M}_\odot$, spherically distributed within a typical radius $R_{\rm gc}$. Also within the cluster, is a CO population consisting of $N_{\rm CO} \equiv qN^{\rm tot}$ objects with $q \ll 1$ that move in the background gravitational potential of the stars. I define the "typical CO mass" as $\langle m_{\rm CO}\rangle = 10\mathrm{M}_\odot$. I adopt typical values of $N^{\rm tot} = 10^6$, $R_{\rm gc} = 1\,\mathrm{pc}$, $N_{\rm CO} = 10^3$, with $q = 10^{-3}$, and $\langle m\rangle \simeq \mathrm{M}_\odot$ (Djorgovski & Meylan, 1994; Miller, 2002; Portegies Zwart & McMillan, 2000).

I construct two different models for the distribution of mass, spatial coordinate, and velocities of stars. Model I is a simple plausible model to get the scaling of PE event rates on different cluster parameters. Here I assume a homogeneous spherical distribution, and the COs within the cluster have the same mass and magnitudes of velocities. In Model II, I refine the assumptions to account for the distributions of masses, mass segregation, and relative velocity distributions.

By comparing Models I and II, I find that while Model I gives the correct $R_{\rm gc}$, $N^{\rm tot}$, $N_{\rm CO}$, and f_0 scalings, it underestimates the total event rate of a single GC by 2 orders of magnitudes. The comparison of Models I and II is necessary (i) to understand the origin of the large increase in PE event rates as compared to Dymnikova et al. (1982), and (ii) to understand the impact on the BH mass function of GCs on PE event rates. It is therefore emphasized that the GC model assumptions have a crucial importance when determining the PE event rate. I believe that my Model II includes all of the essential features of GCs for the assessment of PE rates, and uncertainties are comprised of the uncertainties in the model parameters rather than additional fundamental processes[5].

[5] For example, details like bound binary populations and interactions are not essential for PEs, and Spitzer instability and core collapse can be accounted for by choosing my model parameters accordingly (see Section 4.7.3 for a discussion).

Model I

For the most simple model, the spatial distribution is assumed to be uniform within a characteristic radius R_{gc}, and it is assumed that all COs have the same mass $m_{\mathrm{CO}} = 10\mathrm{M}_\odot$ and magnitude of velocity v_{vir}. The orientation of velocities is isotropic, implying a velocity dispersion of $\sigma \simeq v_{\mathrm{vir}}$. For this simple model, I estimate the relative velocity distribution of COs to be the same as the individual velocities $v_{\mathrm{rel}} \simeq v_{\mathrm{vir}}$. The characteristic velocities can be obtained from the virial theorem for a uniform distribution of mass[6]:

$$v_{\mathrm{vir}} = \sqrt{\frac{3}{5}\frac{\mathrm{G}N^{\mathrm{tot}}\langle m\rangle}{R_{\mathrm{gc}}}} \tag{4.9}$$

The PE event rate is calculated as the rate of scattering on a fixed target lattice, with incident velocity v_{vir}.

Model II

I improve Model I with the following factors. The validity and motivation of these assumptions is discussed below the list.

1. I assume an equal number of NSs and BHs $N_{\mathrm{NS}} = N_{\mathrm{BH}}$. I introduce $g_{\mathrm{BH}}(m) = 0.5[\ln(m_{\mathrm{max}}/m_{\mathrm{min}})]^{-1}\, m^{-1}$ for the fractional distribution of BH masses among COs with mass m per mass interval dm, in the range $m_{\mathrm{min}} < m < m_{\mathrm{max}}$, with $\int g_{\mathrm{BH}}(m)\mathrm{d}m = 0.5$. I define the NS mass distribution $g_{\mathrm{NS}}(m)$ as a Gaussian distribution with norm 0.5, mean $1.35\mathrm{M}_\odot$, and variance $0.1\mathrm{M}_\odot$. Finally I define the CO distribution by $g_{\mathrm{CO}}(m) = g_{\mathrm{BH}}(m) + g_{\mathrm{NS}}(m)$, which has a unit norm. For definiteness, I take $N_{\mathrm{BH}} = 500$, $m_{\mathrm{min}} = 5\mathrm{M}_\odot$, and $m_{\mathrm{max}} = 60\mathrm{M}_\odot$, implying that $\langle m_{\mathrm{BH}}\rangle \simeq 20\mathrm{M}_\odot$ and $\langle m_{\mathrm{CO}}\rangle \simeq 10\mathrm{M}_\odot$, but also calculate detection rates for more general BH mass distributions. The PE detection rates are practically independent of the actual total number and distribution of NSs.

2. I account for the mass segregation by assuming thermal equipartition among COs, objects with mass m have a velocity $v_m = (m/\langle m\rangle)^{-1/2} v_{\mathrm{vir}}$, and are confined

[6] There is a similar result for a spherical star system of polytropic distribution with a root mean square radius R. The only difference is in the 3/5 factor of Eq. 4.9, which becomes 1/2 in that case (e.g. Saslaw 1985).

within a radius, $R_m = (m/\langle m\rangle)^{-1/2} R_{\rm gc}$, while regular stars are distributed uniformly within a sphere of radius $R_{\rm gc}$, as in Model I. Since $N \gg N_{\rm CO}$, the background gravitational potential is determined by regular stars. See Figure 4.2 for an illustration. For core collapsed models a modified scaling is necessary (see text below).

3. The relative velocity for COs with masses m_1 and m_2 is assumed to be $v_{\rm rel} \equiv v_{12} = [(m_1^{-1} + m_2^{-1})\langle m\rangle]^{1/2} v_{\rm vir}$.

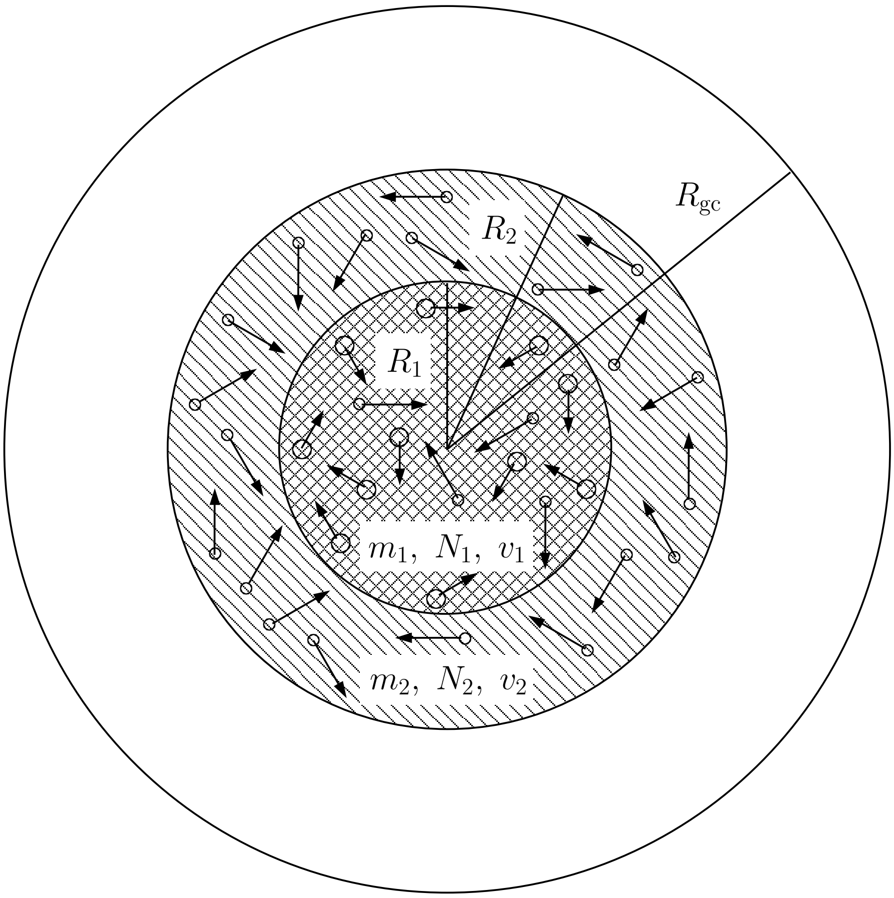

Figure 4.2 Encounters for Model II. More massive COs $m_1 > m_2$ are distributed uniformly within a sphere of smaller radius $R_1 < R_2$ and have smaller velocities. PEs between COs with m_1 and m_2 can take place within R_1. The relative velocity before the interaction is $v_\infty = v_{12}(m_1, m_2)$. Note that Model II assumes a continuous mass function, for which N_1 and N_2 are in fact infinitesimal.

The BH mass distribution is crucial for the analysis, since signal rates scale with $m^{19/3}$ (see Section 4.5 and the appendix below). Unfortunately, the analysis of BH mass functions have not yet converged. Recent X-ray observations display evidence for 20 galactic BHs with masses between $4 \lesssim m/\mathrm{M}_\odot \lesssim 14$ (Casares, 2006), and ~ 45 ultra-luminous X-ray sources are identified with intermediate-mass black holes (IMBHs) with masses $m = 10^2 - 10^4\mathrm{M}_\odot$ (Blecha et al., 2006; Gebhardt et al., 2005; Miller & Colbert, 2004; Ptak & Colbert, 2004). Theoretical predictions from two-dimensional simulations of stellar core collapse (Fryer & Kalogera, 2001) lead to masses smaller than $20\mathrm{M}_\odot$ with very different distributions depending on the assumptions (fraction of explosion energy used to unbind the star, stellar winds, mass transfer after helium ignition). Sophisticated simulations of the initial phase of rapid star evolution assuming a lower metallicity for the progenitor stars (weaker stellar winds) appropriate for GCs and including a large fraction of binaries, collisions, and accretion leading to the mass buildup of BHs imply an initial smooth decreasing distribution of stellar-mass BHs with masses up to $\sim 60 - 100\mathrm{M}_\odot$ (Belczynski et al., 2006) depending on model assumptions and cluster environments. Results are valid for timescales short compared to later dynamical evolution of the cluster. However, the final fate of the cluster remains highly uncertain. In small GCs, dynamical interactions of binaries might eject a significant portion of the stellar-mass BH population (O'Leary et al., 2006; Portegies Zwart & McMillan, 2000; Sigurdsson & Hernquist, 1993). Following Miller (2002) and Will (2004) I adopt $g_{\mathrm{BH}}(m) \propto m^{-1}$ leaving the minimum and maximum masses free parameters. However, most recent population synthesis simulations (Belczynski et al., 2006) typically yield steeper BH mass functions. For this reason I felt it important to compute results for other distributions $g_{\mathrm{BH}}(m) \propto m^{-p}$ with $p = 0$, 1, and 2, as well. Concerning the other parameters, in my standard model I take $m_{\min} = 5\mathrm{M}_\odot$ and $m_{\max} = 60\mathrm{M}_\odot$, for which $\langle m_{\mathrm{BH}}\rangle \simeq 20\mathrm{M}_\odot$ and $\langle m_{\mathrm{CO}}\rangle \simeq 10\mathrm{M}_\odot$, and assume $N_{\mathrm{BH}} = 500$, but also calculate results for other N_{BH}, $m_{\min}$, and $m_{\max}$ values.

The NS mass distribution that I utilize is supported by observations of 26 radio pulsars and 4 X-ray binaries (Postnov & Prokhorov, 2001, and references therein). The distribution is sharply peaked around $1.35\mathrm{M}_\odot$. My assumption on the total number of NSs ($N_{\mathrm{NS}} = 500$) is somewhat arbitrary, values could be higher or lower depending on what fraction of NSs are ejected by kicks during their formation. My detection rate estimates can be scaled to the appropriate value using $\nu_{\mathrm{NS-NS}} \propto N_{\mathrm{NS}}^2$ and $\nu_{\mathrm{BH-NS}} \propto N_{\mathrm{NS}} N_{\mathrm{BH}}$ (see Section 4.5 below). Note however, that in Section 4.5 I show that NS interactions contribute a negligible fraction of the PE event rate (see Figures 4.6 and 4.7 below).

Note that I do not consider encounters between white dwarfs (WDs). The detection of PEs between WDs are even worse than for NSs, since WD masses are even smaller

(Binney & Tremaine, 1987). My final results show that the PE detection rates roughly scale with $\sim m^{8.33}$, implying that rates are enormously suppressed for WDs: by a factor of $\sim 10^{15}$ relative to $50\mathrm{M}_{\odot}$ BHs, which are typical for detection (see Figure 4.6). Moreover, WDs are disrupted by tidal torques for close encounters, at sub-Hz frequencies. Therefore, PEs of WDs are completely invisible for terrestrial detectors.

The second improvement is to account for mass segregation. The differentiation of the stellar population with mass within the cluster core is a consequence of thermal equilibrium (Binney & Tremaine, 1987). Objects with masses larger than $10\mathrm{M}_{\odot}$ had enough time to relax to thermal equilibrium within the lifetime of the GCs (Farouki & Salpeter, 1982). This means that the kinetic energies of each of the component stars are drawn from the same distribution, implying that the typical speed of an object of mass m is $v_m = (m/\langle m\rangle)^{-1/2} v_{\rm vir}$, causing the object to sink to the core of the cluster. For a nearly homogeneous distribution of background stars, this implies that the maximum radius available to a given mass is $R_m = (m/\langle m\rangle)^{-1/2} R_{\rm gc}$ (Binney & Tremaine, 1987). For the BH distribution given by $g_{\rm BH}(m)$ I get that BHs with mass $\sim 50\mathrm{M}_{\odot}$ (which make the dominant contribution to PE rates, see Figures 4.6 and 4.7 below) are confined to a radius $\sim 0.14 R_{\rm gc}$. Note that my scalings based on thermal equipartition might not hold in case Spitzer instability leads to core collapse, creating a dynamically decoupled core of high mass BHs (typically $R_{\rm core} \sim 0.01$–$0.10 R_{\rm gc}$ depending on the fraction of primordial binaries, Heggie et al. 2006). I account for core collapse by simply scaling my final results on detection rates appropriately with $N_{\rm BH}^2 R_{\rm core}^{-3} v_{\rm core}^{-1}$ (see Section 4.7.3 for a discussion).

Finally, I discuss the assumption on the relative velocity. The velocity distribution of stars in GCs is well described by the King-Michie (KM) model (Meylan, 1987), which is roughly a Maxwell-Boltzmann (MB) distribution with a maximum velocity cutoff. It is well-known that the relative velocity distribution for MB individual velocity distributions is also MB for the reduced mass $\mu = m_1 m_2/(m_1+m_2)$ (Binney & Tremaine, 1987). Thus $\langle v_{12}\rangle_{\rm RMS} = (m_1/\mu)^{1/2} \langle v_{m_1}\rangle_{\rm RMS} = [(m_1^{-1} + m_2^{-1})\langle m\rangle]^{1/2} v_{\rm vir}$.

Note that I do not utilize the exact velocity distribution, but associate the same fixed velocity value for every object with identical masses. Relaxing this approximation and accounting for MB velocity distributions leads to a change of only a few percent in the encounter rate results (the correction is $(3/\pi)^{1/2}$ for Model I in the range of GW detector frequencies, see Kocsis & Gáspár 2004 for the derivation). Thus, the velocity distribution can be safely approximated with the mean value. A simple explanation is the fact that GW detector frequencies correspond to unbound encounters with nearly parabolic trajectories, for which the exact value of the initial velocity is negligible (see

Section 4.5.1 below).

The PE event rate for component masses m_1 and m_2 is calculated as the rate of scattering with incident velocity equal to the initial relative velocity $v_{\rm rel} \equiv v_{12}(m_1, m_2)$.

4.5 Parabolic Encounter Event Rate

I now derive the event rate for the successful detection of PE signals using the two models of GCs. This section is divided in five parts. In Section 4.5.1 I derive the comoving event rate per comoving characteristic frequency bins for individual GCs for the two population models. In Section 4.5.2 I derive the modifications necessary for relativistic encounters. In Section 4.5.3 I determine the signal-to-noise ratio using the specific detector sensitivity curves and determine the maximum observable distance of PEs. In Section 4.5.4, I add up the contributions of all possible GCs within the visible distance and estimate the PE detection rates. Finally in Section 4.5.5 I conclude the results of the analysis.

4.5.1 Contributions of Individual Globular Clusters

Outline

When calculating the detectable event rates for specific GW detectors, it is desirable to express the encounter cross section for particular f_0 frequency bins. To achieve this I first compute the interaction cross-sections for given masses and initial orbital parameters. Then, the Newtonian equations of motion relate the initial orbital parameters to f_0. Changing to the f_0 variable leads to the partial event rate for the given masses and characteristic encounter frequencies. Then, for Model I, it is very simple to add up the individual contributions of all objects within the cluster. For Model II, I utilize the specific radial and relative velocity distributions, R_m and v_{12}, and average over the CO mass distribution.

Derivation of Event Rates

The typical minimum distance between COs in these systems is $R_{\rm gc}/\sqrt[3]{N} \simeq 10^{11}$km, a value several orders of magnitudes larger than the typical minimum separation of an encounter (10km $< b_0 \lesssim 10^7$km for detectable frequencies, see equation (4.14) below). Therefore, a sufficient approximation is to consider short-time two-body interactions during encounters[7], and constant velocities in between events. The PE event rate can then be simply estimated by a scattering of particles with incident initial velocities $v_\infty = v_{\rm rel}$ on a still target lattice.

Since the velocities are assumed to be locally isotropic everywhere in the cluster, the cross section of a particle with an impact parameter between b_∞ and $b_\infty + {\rm d}b_\infty$ is ${\rm d}\sigma = 2\pi b_\infty {\rm d}b_\infty$. I proceed to express the infinitesimal cross section for ${\rm d}f_0$ bins.

I derive encounter parameters with a non-relativistic Newtonian description. The separation, b_0, and relative velocity, v_0, at periastron can be computed from the initial conditions of the interacting bodies. The initial parameters are the impact parameter b_∞ and the velocity, $v_\infty \equiv v_{\rm rel} \equiv v_{12}(m_1, m_2)$, of the scattered particle (see Section 4.4.3 for the definition). Using the conservation of mechanical energy and angular momentum I get

$$b_\infty = \frac{b_0}{\sqrt{1-2\gamma}}, \qquad \text{and} \qquad v_\infty = v_0\sqrt{1-2\gamma}, \tag{4.10}$$

where $\gamma = ({\rm G}M)/(b_0 {v_0}^2)$ is the ratio of potential energy and double kinetic energy at the closest point[8], with $M = m_1 + m_2$. Although equation (4.10) is strictly only valid in the comoving reference frame of the center-of-mass, it is an adequate approximation for the realistic parameters as long as $v_\infty \ll v_0$. Again, I point out that the relevant encounters are nearly parabolic, so that the initial velocity distributions have a negligible impact on the result.

Let us express the cross section with variables b_0 and v_∞ using equation (4.10) and make use of my simplifying assumption that v_∞ is a constant for fixed masses (see Section 4.4.3). The result is

$${\rm d}\sigma = \left(\frac{{\rm G}M}{v_\infty^2 b_0} + 1\right) 2\pi b_0 {\rm d}b_0. \tag{4.11}$$

Here, the first term dominates the parenthesis for typical v_∞ and b_0 values (see Eq. 4.14. below). This term is responsible for the deflection of trajectories due to gravity.

The characteristic GW frequency is directly related to the minimum separation, b_0,

[7] I shall discuss below that the PE event rate is not sensitive on whether the interacting participants are elements of regular bound binaries or if they are single objects.

[8] $\gamma < 1/2$ for hyperbolic Newtonian trajectories.

and the relative velocity v_0 at b_0 by

$$\omega_0 = 2\pi f_0 = \frac{v_0}{b_0}. \tag{4.12}$$

Using equation (4.10),

$$\omega_0 = (2\mathrm{G}M)^{1/2} b_0^{-3/2} \left(1 + \frac{v_\infty^2 b_0}{2\mathrm{G}M}\right)^{1/2}. \tag{4.13}$$

The correction on the RHS is $v_\infty^2 b_0/(2\mathrm{G}M_{\mathrm{CO}}) \lesssim 10^{-8}$ (10^{-4}) for typical frequency bands of InLIGO (*LISA*). In order to get the event rate per frequency bin, I need the inverse relationship $b_0(\omega_0, v_\infty)$. This can be obtained recursively, as a power series in ω_0. To the second non-vanishing order, I get

$$b_0 = (2\mathrm{G}M)^{1/3} \omega_0^{-2/3} \left(1 + \frac{1}{3} \frac{v_\infty^2}{(2\mathrm{G}M)^{2/3}} \omega_0^{-2/3}\right). \tag{4.14}$$

Substituting in equation (4.11) yields

$$\mathrm{d}\sigma = \frac{2\pi}{3} \frac{(2\mathrm{G}M)^{4/3}}{v_\infty^2} \omega_0^{-2/3} \left(1 + \frac{8}{3} \frac{v_\infty^2}{(2\mathrm{G}M)^{2/3}} \omega_0^{-2/3}\right) \frac{\mathrm{d}\omega_0}{\omega_0}. \tag{4.15}$$

For Model I, the scattering rate for a single particle is $n_{\mathrm{CO}} v_\infty \mathrm{d}\sigma$, where n_{CO} is the number density of COs. Since there are a total of N_{CO} particles, the contribution of all COs is $1/2 \times N_{\mathrm{CO}} n_{\mathrm{CO}} v_\infty \mathrm{d}\sigma$, where the 1/2 factor comes from the fact that the same ensemble of particles constitute both the targets and the injection. Thus equation (4.15) becomes

$$\mathrm{d}\nu^{\mathrm{I}} = \nu_1^{\mathrm{I}} \left(\frac{f_0}{f_{100}}\right)^{-2/3} \left(1 + \left(\frac{f_0}{f_1^{\mathrm{I}}}\right)^{-2/3}\right) \frac{\mathrm{d}f_0}{f_0}. \tag{4.16}$$

where $f_{100} = 100\mathrm{Hz}$ and

$$\nu_1^{\mathrm{I}} = (2\pi)^{-2/3} \frac{N_{\mathrm{CO}}^2}{4} \frac{(4\mathrm{G}M_{\mathrm{CO}})^{4/3}}{R_{\mathrm{gc}}^3 v_\infty} f_{100}^{-2/3} = 6.7 \times 10^{-15} \mathrm{yr}^{-1} \tag{4.17}$$

$$f_1^{\mathrm{I}} = \frac{1}{2\pi} \left(\frac{8}{3}\right)^{3/2} \frac{v_{\mathrm{vir}}^3}{4\mathrm{G}M_{\mathrm{CO}}} = 1.7 \times 10^{-8} \mathrm{Hz}. \tag{4.18}$$

For Model II, the interacting objects with masses m_1 and m_2 are distributed uniformly within radii R_1 and R_2 and have mass-dependent relative velocities $v_\infty = v_{12}$ (see Figure 4.2). Let N_1 and N_2 denote the number of particles with mass m_1 and m_2, respectively. Let us assume $m_1 > m_2$, for which $R_1 < R_2$. In this case the interactions between masses m_1 and m_2 take place only within a radius R_1, where the density of particles with mass m_2 is $n_2 = N_2/(R_2^3 4\pi/3)$. For a smooth distribution, N_1 is the infinitesimal number of particles with masses between m_1 and $m_1 + \mathrm{d}m_1$, i.e. $N_1 = N_{\mathrm{CO}} g_{\mathrm{CO}}(m_1)\mathrm{d}m_1$ (and N_2 defined similarly). The scattering rate for an injection of N_1 particles with v_∞ velocities on a target density n_2 is is $N_1 n_2 v_\infty \mathrm{d}\sigma$. To get the total event rate for the cluster for ω_0 bins I need to integrate over the mass distributions

$$\begin{aligned}\mathrm{d}\nu^{\mathrm{II}} = &\int_0^\infty \mathrm{d}m_1 g_{\mathrm{CO}}(m_1) \int_0^\infty \mathrm{d}m_2 g_{\mathrm{CO}}(m_2) \; \times \\ &\left[\nu_1^{\mathrm{II}}(m_1, m_2)\left(\frac{f_0}{f_{100}}\right)^{-2/3} + \nu_2^{\mathrm{II}}(m_1, m_2)\left(\frac{f_0}{f_{100}}\right)^{-4/3}\right]\frac{\mathrm{d}f_0}{f_0},\end{aligned} \tag{4.19}$$

where $\nu_1^{\mathrm{II}}(m_1, m_2)$ and $\nu_2^{\mathrm{II}}(m_1, m_2)$ are given by

$$\nu_1^{\mathrm{II}}(m_1, m_2) = (2\pi)^{-2/3}\frac{N_{\mathrm{CO}}^2}{4}\frac{(2\mathrm{G}M)^{4/3}}{R_>^3 v_\infty} f_{100}^{-2/3} \tag{4.20}$$

$$\nu_2^{\mathrm{II}}(m_1, m_2) = (2\pi)^{-4/3}\frac{2N_{\mathrm{CO}}^2}{3}\frac{(2\mathrm{G}M)^{2/3} v_\infty}{R_>^3} f_{100}^{-4/3} \tag{4.21}$$

where $R_> = \max(R_1, R_2)$ and the mass dependence is implicit in the total mass M, $v_\infty = v_{12}$, R_1, and R_2 (see the Appendix for explicit formulae).

The mass integrals in equation (4.19) can be evaluated independent of the frequency, resulting in the same functional form as for Model I equation (4.16). The constants for Model II are

$$\nu_1^{\mathrm{II}} = 1.9 \times 10^{-12}\mathrm{yr}^{-1} \tag{4.22}$$

$$f_1^{\mathrm{II}} = 1.0 \times 10^{-10}\mathrm{Hz}. \tag{4.23}$$

(see the Appendix for parametric formulae).

For Model II, it is also interesting to get the relative encounter rates for BH – BH, BH – NS, and NS – NS interactions. Integrating equation (4.19) over the corresponding mass intervals, I get

$$\nu^{\rm II}_{1,{\rm BH-BH}} = 0.996\,\nu^{\rm II}_1 = 286\,\nu^{\rm I}_1, \tag{4.24}$$
$$\nu^{\rm II}_{1,{\rm BH-NS}} = 4.14\times10^{-3}\nu^{\rm II}_1 = 1.19\,\nu^{\rm I}_1, \tag{4.25}$$
$$\nu^{\rm II}_{1,{\rm NS-NS}} = 7.04\times10^{-5}\nu^{\rm II}_1 = 0.02\,\nu^{\rm I}_1. \tag{4.26}$$

The corresponding analytical formulas are given in the Appendix. It is clear that BH – BH encounters dominate the event rates. The event rates of NS – NS encounters are more than four orders of magnitude lower!

Discussion

Therefore I conclude that Model II has a much larger event rate than Model I. By inspection of equations (4.19) and (4.20) the main factors responsible for this increase can be identified. First, the CO density is increased by the CO confinement in the core: $n \propto {R_m}^{-3} \propto m^{3/2}$. Second, the typical CO relative velocity inverse is increased: $v_\infty^{-1} \propto m^{1/2}$. Third, the gravitational focusing is proportional to $m^{4/3}$. Thus, $\nu_1 \propto \left(R^3_{\rm gc}/R^3_{\rm CO}\right) \times \left(\langle m^{10/3}\rangle/m^{10/3}_{\rm CO}\right)$. The PE event rate is thus highly inclined towards the high-mass end of the BH distribution in the cluster. For a more precise treatment, the exact contributions of the component mass parameters are given in the Appendix. Note, that Dymnikova et al. (1982) obtained results equivalent to my equation (4.17) of Model I, but they focus on star – star encounters and use $m = 4{\rm M}_\odot$ instead of $m_{\rm CO} = 10{\rm M}_\odot$. (Another difference is that they do not discuss f_0-dependent differential rates, but derive the total PE rate based on a typical minimum separation. Using $m = 4{\rm M}_\odot$ in Model I, the results are a factor of 10^3 lower than the rates for Model II.)

Equations (4.16-4.18) and (4.22-4.23) give the resulting PE event rate per GC of all Newtonian trajectories between point masses for the two GC models considered. A significant shortcoming is that COs have finite radii and collide for sufficiently small minimum separations. Moreover the Newtonian approximation breaks down for large velocities or strong gravitational fields. These effects are considered in Section 4.5.2 below.

Notice how small is the correction proportional to $f_0^{-4/3}$ in equation (4.16) for GW detector frequencies $f \gg f_1^{\rm I,II}$. Recall that in equations (4.13,4.14) the expansion coefficient is proportional to v_∞. Hence the leading order term is exact for $v_\infty = 0$, thus it corresponds to parabolic trajectories. This proves my conjecture that the unbound orbit encounter rate is dominated by near-PEs.

In equation (4.16) the leading-order terms are proportional to $1/v_{\rm vir}$. The result is slightly counterintuitive if one identifies the star system with an ideal gas, since for ideal gases, the rate of collisions is directly proportional to v_∞. In this perspective it seems reasonable to expect the encounter rate to be a growing function of v_∞ for fixed frequency bins. The confusion arises from the fact that my GC models are using the opposite limit. For star systems the typical velocities are so small that the gravitational interaction dominates the motion of the stars.[9] Increasing the velocities decreases the gravitational focusing, thereby decreasing the encounter likelihood.

The expected rate of PE events for a single GC is plotted in Figure 4.3 for logarithmic frequency bins for the two GC models. The non-relativistic results presented in this section are plotted with dotted lines, which overlap with the relativistic calculation below $\sim$10Hz. For higher frequency the minimum separation drops below $\sim$6 Schwarzschild radii for the largest BHs and relativistic corrections become important. Figure 4.3 displays that event rates are higher for lower characteristic frequencies, e.g. for model II for $f_0 = 0.1\,\mathrm{mHz}$ (the minimum frequency for space detectors), I get $1.9\times10^{-8}\mathrm{yr}^{-1}\mathrm{GC}^{-1}$ events, whereas for terrestrial detectors $f_0 = 100\mathrm{Hz}$ it is only $1.9\times10^{-12}\mathrm{yr}^{-1}\mathrm{GC}^{-1}$.

4.5.2 Relativistic Orbits

Up to this point the PE event rates have been estimated for fixed characteristic frequencies but independent of the minimum separation b_0 and relative velocity v_0. In addition to non-relativistic parabolic encounters, these events also include head-on collisions, relativistic captures, relativistic flybys, and zoom-whirl orbits. Since I have used a Newtonian analysis in the derivation, my results presented in Section 4.5.1 are valid for the non-relativistic parabolic encounters only. Here, I improve the classical calculation to account for general relativistic encounters of test particles moving along geodesics in the Schwarzschild space-time. This treatment is exact for extreme mass ratios, but as an approximation I extrapolate these formulas for general mass-ratios as well.

To classify the orbits, I introduce a parameter $\lambda \equiv b_0/R_{\rm SH}$, where b_0 is the distance

[9] The ideal gas model is sufficient only for extremely small characteristic frequencies $f_0 \ll f_1$ (see equations (4.18,4.23)), which is below the lower frequency limit of GW detectors. In this regime the stars' trajectories are only slightly deflected, implying that gravity, in terms of encounter likelihood, is negligible.

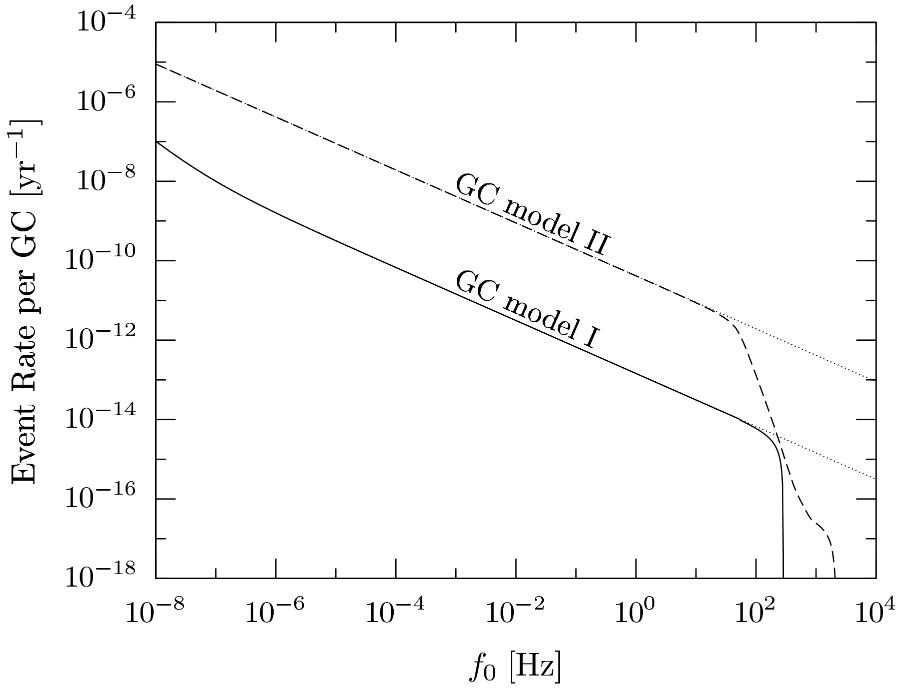

Figure 4.3 The expected total rate of PEs produced in a single GC per logarithmic frequency bin. GC Model I (solid) and Model II (dashed) results are shown including relativistic corrections for geodesics avoiding head-on collisions (see Section 4.5.2). The dotted lines represent PE event rates in the non-relativistic approximation. The non-relativistic treatment is adequate for low frequencies for which the trajectories avoid collisions with minimum separations of several Schwarzschild radii. Only a fraction of these events can be detected, depending on the distance of the GC.

at periastron, and $R_{\rm SH} = 2{\rm G}M/{\rm c}^2$ is the Schwarzschild radius of the total mass[10]. For Newtonian parabolic encounters, I get $\lambda = {\rm c}^2/v_0^2$. I distinguish (i) non-relativistic parabolic encounters for $\lambda \geq 6$, (ii) general relativistic flybys for $2.1 < \lambda < 6$, (iii) zoom-whirl orbits for $2 \leq \lambda \leq 2.1$, and (iv) head-on collisions for $2 < \lambda$. I restrict my calculations to $\lambda \geq 2$, since this is the regime in which matched filtering can be carried out using the waveforms of Section 4.3.

In this section, I improve Section 4.5.1 to account for the relativistic deviations in the trajectories. In practice, I repeat the derivation of Section 4.5.1 to get the cross-section using the orbital parameters of the geodesics of a test particle moving in a Schwarzschild space-time (Gair et al., 2005).

For parabolic encounters the specific orbital angular momentum is

$$\widetilde{L} = \sqrt{2{\rm G}Mb_0}\,\left(1-\lambda^{-1}\right)^{-1/2}, \tag{4.27}$$

where $\lambda = \lambda(b_0)$ defined above. The non-relativistic result is retained for $\lambda \to \infty$. Equating equation (4.27) to the angular momentum before the encounter $\widetilde{L} = b_\infty v_\infty$, solving for b_∞, and substituting in ${\rm d}\sigma = 2\pi b_\infty {\rm d}b_\infty$ I get

$${\rm d}\sigma = \frac{{\rm G}M}{v_\infty^2 b_0^2}\frac{1-2\lambda^{-1}}{(1-\lambda^{-1})^2}\,2\pi b_0 {\rm d}b_0. \tag{4.28}$$

This is to be compared to the non-relativistic analogue equation (4.11). The first term is the non-relativistic term for near-parabolic orbits and the λ-dependent fraction describes the relativistic correction. The latter decreases the cross section per unit b_0. For $\lambda \to 2$ the cross section becomes 0. For smaller impact parameters a head-on collision takes place, for which the periastron distance and λ is undefined.

Repeating Section 4.5.1, the next step is to change to the f_0 characteristic frequency variable. Since $\widetilde{L} = b_0^2\ {\rm d}\phi/{\rm d}\tau$, where ${\rm d}\tau = (1-\lambda^{-1})^{1/2}\,{\rm d}t$ is the infinitesimal proper time element along the geodesic at the closest approach (e.g. Misner et al., 1973), from equation (4.27) I get

$$\frac{{\rm d}\phi}{{\rm d}t} \equiv \omega_0 \equiv 2\pi f_0 = (2{\rm G}M)^{1/2} b_0^{-3/2}. \tag{4.29}$$

Quite remarkably, this is identical to the result of the non-relativistic calculation for parabolic orbits, equation (4.13). The GW waveforms have a peak at an angular fre-

[10]Here I restrict to BH-BH encounters which dominate event rates, see equations. (4.24-4.26).

quency ω_0 for the non-relativistic encounters (Turner, 1977, and see Section 4.3 above). For relativistic zoom-whirl orbits with several revolutions around the central BH, the most intensive GWs are radiated at twice the orbital frequency. It is also useful to get the inverse relationship from equation (4.29):

$$\lambda(M, f_0) = \left(\frac{\mathrm{c}^3}{4\pi\mathrm{G}}\frac{1}{Mf_0}\right)^{2/3}. \tag{4.30}$$

According to equation (4.29), the non-relativistic result for ω_0 is adequate even in this regime. Using equation (4.13) I get

$$\mathrm{d}\sigma = \frac{2\pi}{3}\frac{(2\mathrm{G}M)^{4/3}}{v_\infty^2}\omega_0^{-2/3}\frac{1-(\omega_0/\omega_{M,\mathrm{max}})^{2/3}}{\left[1-\frac{1}{2}(\omega_0/\omega_{M,\mathrm{max}})^{2/3}\right]^2}\frac{\mathrm{d}\omega_0}{\omega_0}, \tag{4.31}$$

analogous to equation (4.15) for parabolic orbits, where

$$\omega_{M,\mathrm{max}} \equiv 2\pi f_{M,\mathrm{max}} \equiv \frac{2\pi\mathrm{c}^3}{\sqrt{32}\mathrm{G}M} \tag{4.32}$$

is the maximum angular frequency, corresponding to $\lambda = 2$.

It is desirable to calculate the partial event rates of PEs with minimum separations b_0 exceeding λR_{SH}, I substitute in equation (4.13), and impose the resulting constraint on the characteristic frequency:

$$f_0 \leq f_{M,\lambda} = 2\pi\frac{\mathrm{c}^3}{2\mathrm{G}M}\lambda^{-3/2}. \tag{4.33}$$

For marginally plunging orbits, $\lambda = 2$, I get $f_{M,\lambda} = f_{M,\mathrm{max}}$.

When adding up the total event rates for a particular f_0 using equations (4.16) and (4.19) only the masses satisfying the constraint equation (4.33) have to be included in the mass integrals. Repeating Section 4.5.1 with these modification, I get for Model I

$$\mathrm{d}\nu^I = \nu_1^I\left(\frac{f_0}{f_{100}}\right)^{-2/3}\frac{1-2(f_0/f_{M,\mathrm{max}})^{2/3}}{\left[1-(f_0/f_{M,\mathrm{max}})^{2/3}\right]^2}\frac{\mathrm{d}f_0}{f_0}. \tag{4.34}$$

for $f_0 \le f_{M_{\rm CO},\lambda}$, and $\mathrm{d}\nu^I = 0$ otherwise. For Model II, I get

$$\mathrm{d}\nu^{\rm II} = \iint_{f_0 \le f_{M,\lambda}} \mathrm{d}m_1 \mathrm{d}m_2 g_{\rm CO}(m_1) g_{\rm CO}(m_2) \nu_1^{\rm II}(m_1, m_2) \times \frac{1 - 2(f_0/f_{M,\rm max})^{2/3}}{[1-(f_0/f_{M,\rm max})^{2/3}]^2} \left(\frac{f_0}{f_{100}}\right)^{-2/3} \frac{\mathrm{d}f_0}{f_0}, \tag{4.35}$$

In equations (4.34) and (4.35), $\nu_1^{\rm I}$ and $\nu_1^{\rm II}(m_1, m_2)$ are the non-relativistic terms given by equations (4.17) and (4.20).

Figure 4.3 shows the resulting total event rates for $\mathrm{d}\ln f_0$ intervals. The solid and dashed lines represent the total event rates of PEs for Models I and II, respectively, including the relativistic correction for encounters that avoid collisions. As a comparison, dotted lines display non-relativistic results. Compared to the non-relativistic results, event rates decrease for two reasons: first the gravitational focusing decreases the cross sections of relativistic orbits, for $2100\text{Hz} = f_{0,\rm max}[2m_{\rm NS}, (\lambda = 2)] \gtrsim f_0 \gtrsim f_{0,\rm max}[2m_{\rm max}, (\lambda = 6)] = 10\text{Hz}$, and second, the plunging orbits with $\lambda < 2$ are excluded from my estimate. The latter effect kicks in at $f_{0,\rm max}(2m_{\rm max}, 2) > 47\text{Hz}$ where the highest mass BHs suffer head-on collisions. At $f_{0,\rm max}(2m_{\rm min}, 2) = 570\text{Hz}$ even the smallest BHs are captured, and only the NS–NS PE event rate contributions remain. The NS–NS partial event rates can be visualized for lower frequencies by extrapolating the total event rates shown in Figure 4.3 between $570\text{Hz} < f_0 < 2100\text{Hz}$. The NS–NS event rates are clearly negligible compared to the total rates including BHs. Note, that my calculations use point masses valid for BHs only. For $f_0 \gtrsim 1500\text{Hz}$ the minimum separation of $1.35\mathrm{M}_\odot$ NSs decreases under ~ 20km, for which my approximation breaks down.

Figure 4.3 is useful to visualize the total PE event rate per GC. However, only a fraction of these events can be detected, and this fraction depends on both the differential encounter event rates $\partial^3\nu/\partial m_1 \partial m_2 \partial \ln f_0$ and also the observable distance of the encounter. For the detection rates I shall make use of the infinitesimal encounter event rate for infinitesimal mass and f_0 bins. From equation (4.35) I get[11]

$$\frac{\partial^3 \nu}{\partial m_1 \partial m_2 \partial \ln f_0} = \nu_1^{\rm II}(m_1, m_2) \frac{1 - 2(f_0/f_{M,\rm max})^{2/3}}{[1-(f_0/f_{M,\rm max})^{2/3}]^2} \left(\frac{f_0}{f_{100}}\right)^{-2/3}. \tag{4.36}$$

[11] I follow to notation of Miller (2002) and Will (2004) for the definition of partial event rates by not including the mass distribution $g_{CO}(m)$. The mass distributions enter only when integrating for the total event rates equation (4.42).

The *total event rate* for one GC depends only on $\partial^3\nu/\partial m_1 \partial m_2 \partial \ln f_0$, thus in equation (4.35) equation (4.36) was directly integrated over f_0, and the m_1, and m_2 distributions. However for the *detection rate*, the observation distance of the encounter depends on f_0, m_1, and m_2 differently. Therefore the differential *detection rate* has a modified parameter dependence, implying that the integration can be carried out only after the observation distance had been included in the differential rate.

4.5.3 Maximum Distance of Detection

I now derive the maximum detectable distance of an encounter for fixed masses m_1, m_2, and characteristic frequency f_0, for a given signal-to-noise ratio S/N. The luminosity distance can be expressed with the redshifted parameters, $m_{iz} = (1+z)m_i$ for $i = \{1, 2\}$ and $f_{0z} = f_0/(1+z)$, using the angular averaged signal-to-noise ratio, equation (4.2), and signal waveform, equation (4.5):

$$d_{\mathrm{L}}(m_{1z}, m_{2z}, f_{0z}) = \frac{\sqrt{85}\,\pi^{2/3}}{2^{5/3}} \frac{\mathrm{G}^{5/3}}{\mathrm{c}^4} \frac{\mathcal{M}_z{}^{5/3}}{S/N} \sqrt{\frac{E_{\mathrm{rel}}(\lambda)}{E_{\mathrm{nr}}(\lambda)}} W(f, f_{0z}), \tag{4.37}$$

where $E_{\mathrm{rel}}(\lambda)/E_{\mathrm{nr}}(\lambda)$ is the enhancement of the GW energy for general relativistic orbits (Gair et al., 2005, and see Section 4.3 above), where $\lambda = \lambda(M, f_0) = \lambda(M_z, f_{0z})$ is given by equation (4.30), and $W(f, f_{0z})$ is a factor depending on only the frequencies

$$W(f, f_{0z}) = \sqrt{\frac{4}{5} \int_{f_{\min}}^{f_{\max}} \frac{f_{0z}^{4/3}}{f^2} \frac{F(f/f_{0z})}{S_n(f)}\, \mathrm{d}f} \tag{4.38}$$

$F(x)$ is the dimensionless, normed GW energy spectrum defined in Section 4.3, $f_{\min}$ and $f_{\max}$ are the minimum and maximum frequencies specific for GW detectors (see Section 4.2). Henceforth I shall fix $S/N = 5$, but other values can be roughly obtained by scaling the final result on detection rates with $(S/N)^{-3}$ (assuming that the number of sources increases with $d_{\mathrm{L}\max}^{3}$).

Note that equation (4.37) formally depends on redshifted parameters. However, since both the differential encounter event rate, equation (4.36), and the GC model mass distribution depend on the comoving parameters, it is useful to revert to the comoving parameters in equation (4.37) and get $d_{\mathrm{L}}(m_1, m_2, f_0)$. This can be achieved by writing $m_{iz} = (1+z)m_i$ for $i = \{1, 2\}$ and $f_{0z} = f_0/(1+z)$ in equation (4.37) and making this equal to the standard formula $d_{\mathrm{Lcos}}(z)$ connecting the luminosity distance and redshift in a specific cosmology Eisenstein (e.g 1997, the index "cos" refers to the cosmological luminosity distance–redshift formula in order to distinguish this from the maximum distance, equation (4.37), specific for PE encounters). Now both sides depend on z. Numerically solving for z gives $z(m_1, m_2, f_0)$. Finally substituting the result back in $d_{\mathrm{Lcos}}(z)$ gives $d_{\mathrm{L}}(m_1, m_2, f_0)$.

This procedure is however cumbersome in practice. It becomes numerically very time-consuming when computing the total detection rates, which includes the evaluation of integrals over the parameters. Therefore I make the following essential approximations when solving for the luminosity distance in equation (4.37):

$$d_{\mathrm{L}}(m_1, m_2, f_0) \equiv \begin{cases} \text{using } z = 0 & \text{if } z_1 \leq 0.01 \\ \text{using } z = \mathrm{H}_0 d_{\mathrm{L}}/\mathrm{c} & \text{if } z_1 \leq 0.1 \\ \text{no approximations} & \text{if } 0.1 < z_1 < 6 \\ \text{using } z = 6 & \text{if } S/N > 5 \text{ for } z = 6 \end{cases} \tag{4.39}$$

On the RHS of equation (4.39), z_1 is the first approximation of the redshift, which is obtained by calculating d_{L} from the RHS of equation (4.37) with no redshift, and making this equal to $d_{\mathrm{Lcos}}(z_1)$, and solving for z_1. I neglect cosmology for $z_1 < 0.01$ and take a Hubble constant $\mathrm{H}_0 = 70\mathrm{km/s/Mpc}$ for $0.01 < z_1 < 0.1$. Next, whenever $z_1 > 0.1$, I substitute $z = 6$ for the RHS of equation (4.37) and in case this is already larger than $d_{\mathrm{Lcos}}(6)$, then I conclude that the source is observable at $z = 6$ for $S/N > 5$ and take $d_{\mathrm{L}} = d_{\mathrm{Lcos}}(6)$ as the maximum distance of observation. I do not explore detection rates at larger redshifts, since then the BH mass and radial distribution might not have relaxed to the final state. If $S/N < 5$ for $z = 6$ then I execute the exact procedure without approximations for $z_1 > 0.1$

Changing to the non-redshifted variables in equation (4.37) is even ambiguous in some cases. For *NGLISA* the signal-to-noise ratio is occasionally not a decreasing but an increasing function of the redshift. This happens when the signal is redshifted to the more sensitive range of frequencies of the detector, and the enhancement in sensitivity is more substantial than the attenuation from increasing the distance. In these cases a certain encounter can be observed within a certain distance, then increasing the distance, the encounter first becomes invisible (i.e. $S/N < 5$), then again visible (i.e. $S/N \geq 5$) within a second maximum distance. This phenomenon occurs for *NGLISA* for large BH masses and near-maximum characteristic frequencies.

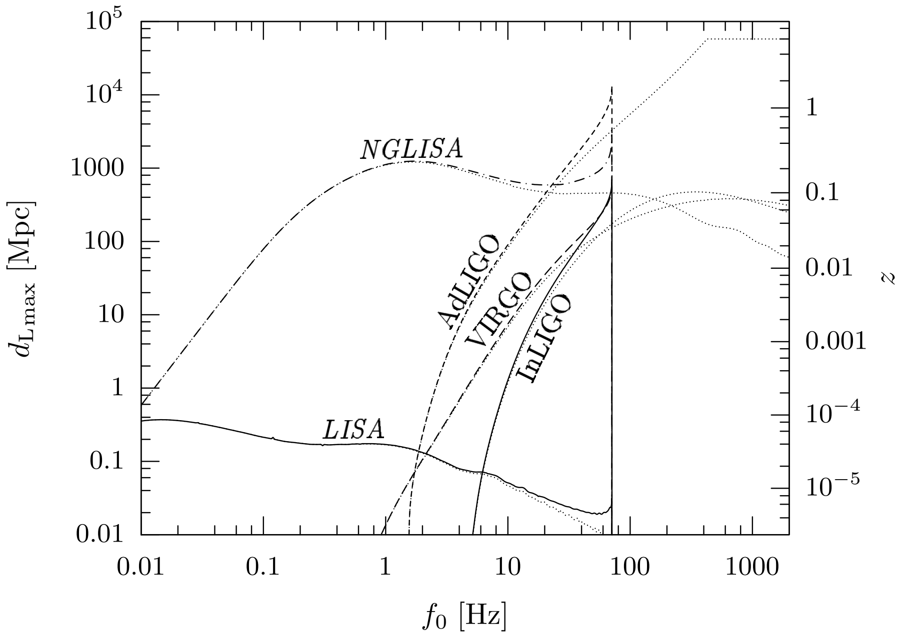

Figure 4.4 Maximum luminosity distance, $d_{\rm Lmax}$, of two BHs with $m_1 = m_2 = 40\mathrm{M}_\odot$ masses undergoing a PE, and emitting GWs that are detected on average with $S/N = 5$. The x-axis shows the emitted f_0 characteristic frequency of the flyby comoving with the host GC. The curves correspond to InLIGO, VIRGO, AdLIGO, *LISA*, and *NGLISA*, respectively. Thin dotted lines show the result for Newtonian waveforms (Turner, 1977), thick lines account for general relativistic corrections to the GW amplitudes for close encounters. For frequencies larger than $f_{M,\max} = 71$Hz the minimum distance is under $\lambda = 2$ Schwarzschild radii, for which a head-on collision takes place. I did not impose any restrictions on λ for the non-relativistic curves. All curves account for the redshifting z, which is shown on the right border. I restrict to $z \leq 6$. For different masses, $d_{\rm L}$ scales with roughly $\mathcal{M}^{5/3}$ and the cutoff frequency scales with M^{-1}. Since signals are broadband, the detectors have a chance to observe a broad range of f_0.

Figure 4.4 shows the maximum distance of sources with $S/N = 5$ for $m_1 = m_2 = 40\mathrm{M}_\odot$ BH masses. The thick curves account for the relativistic corrections with minimum separations larger than $\lambda = 2$, the thin dotted lines represent the non-relativistic results with no bound on λ. The maximum frequency equation (4.32) corresponding to marginally colliding orbits ($\lambda = 2$) is 71Hz and scales with M^{-1} for other masses. For other masses d_{Lmax} scales with $\mathcal{M}^{3/5}$. All curves account for the cosmological redshifting. The plot shows, that the non-relativistic approximation is adequate for small frequencies, but it implies a luminosity distance a factor of $2-3$ lower than the relativistic calculation near the maximum f_0 frequency. Therefore, the dotted lines are useful to approximately visualize d_{Lmax} for lower M, when the cutoff frequency shifts to higher values.

The enclosed volume and the observable sources are given by equation (4.8). If neglecting relativistic and cosmological effects, I get $V \propto D^3 \propto \mathcal{M}^5$.

4.5.4 Detection Rates

In the previous sections I calculated the differential event rates of PEs for single GCs per infinitesimal mass and frequency bins, and computed the maximum distance of their detection. Here I combine these results to calculate the total detection rate of PEs.

For fixed m_1, m_2, and f_0, the rate of GW detections of the corresponding encounters is the observed rate for a single GC times the number of observable GCs. Since there is a cosmological redshift between the source GC and the observation, the single-GC rate is reduced by $1 + z$:

$$\frac{\partial^2 \nu^{\mathrm{total}}}{\partial m_1 \partial m_2 \partial \ln f_0} = \frac{1}{1+z} \frac{\partial^2 \nu^{\mathrm{single}}}{\partial m_1 \partial m_2 \partial \ln f_0} N^{gc}(m_1, m_2, f_0). \tag{4.40}$$

The first term is the redshifted event rate expressed with the comoving event rate equation (4.36) and the second is simply

$$N^{\mathrm{gc}}(m_1, m_2, f_0) = N^{\mathrm{gc}}[d_{\mathrm{Lmax}}(f_0, m_1, m_2)], \tag{4.41}$$

where $N^{\mathrm{gc}}(d_{\mathrm{L}})$ is the number of GCs within a given maximum luminosity distance. In practice d_{Lmax} is given by equation (4.39) which I substitute in equation (4.8).

The total detection rate is then simply the integral of the differential detection rate, equation (4.40), using the CO mass distribution. After substituting, I get

$$\nu^{\rm tot}(f_0) = \int_0^{f_{0\,\max}} \frac{\mathrm{d}f_0}{f_0} \iint_{f_0 \le f_{M,\max}} \mathrm{d}m_1 \mathrm{d}m_2 g_{\rm CO}(m_1)\, g_{\rm CO}(m_2)\, \frac{\partial^2 \nu^{\rm total}}{\partial m_1 \partial m_2 \partial \ln f_0} \tag{4.42}$$

where $g_{\rm CO}(m)$ is the CO mass distribution for Model II, defined in Section 4.4.3. The mass integrals are evaluated over the (m_1, m_2) domain for which the encounter avoids a collision (i.e. $f_0 \le f_{M,\max}$, see equation (4.32)) and the f_0 integral extends to a maximum possible frequency independent of masses ($\sim f_{2m_{\rm NS},\max}$). The result of equation (4.42) is one number, the expected rate of detection for the specific detector.

4.5.5 Results

The estimated total number of successful detections from equation (4.42) is $\nu^{\rm tot} = 5.5 \times 10^{-5}\mathrm{yr}^{-1}$ for InLIGO, $7.2 \times 10^{-5}\mathrm{yr}^{-1}$ for VIRGO, $6.3 \times 10^{-2}\mathrm{yr}^{-1}$ for AdLIGO, $2.9 \times 10^{-6}\mathrm{yr}^{-1}$ for *LISA* and $1.0\mathrm{yr}^{-1}$ for *NGLISA*.

It is interesting to see the differential event rate per logarithmic f_0 bin independent of masses, which is obtained by carrying out only the mass integrals in equation (4.42). The result is shown in Figure 4.5. The figure shows that both AdLIGO and *NGLISA* could have some chance to detect PE events, if observing for one year; AdLIGO mainly sensitive to f_0 frequencies between 30 and 80Hz, and *NGLISA* sensitive between 0.2Hz and 10Hz. There is a sharp cutoff in the PE detection rate for high frequencies. In this regime, the encounters among the relatively higher mass BHs are not parabolic, but result in direct captures, and only the lower mass BHs contribute to the PE detection rate. show the differential event rate for logarithmic total mass bins, $\mathrm{d}\ln M$, and for logarithmic mass ratio bins, $\mathrm{d}\ln q$. Here I define the mass ratio as $q = m_</m_>$ for which $q \le 1$. (Recall the definitions $m_< = \min(m_1, m_2)$ and $m_> = \max(m_1, m_2)$.) The M dependent partial PE detection rate can be obtained from equation (4.42) by changing the m_1, m_2 integrals to M and m_2 variables, rearranging the order of integrals, and evaluating the f_0 and m_2 integrals only. The partial PE rates for fixed q can be obtained similarly, by changing to $m_>$ and q variables, and evaluating the f_0 and $m_>$ integrals only. In Section 4.5.1 I demonstrated that the event rates of GCs are sensitive to $\langle m^{10/3} \rangle$, and are inclined towards the high-mass end of the CO distribution, in particular PEs of NSs have a relatively negligible event rate. The detectable volume entails an even stronger mass dependence m^5. Therefore, for a mass distribution of m^{-1}, I expect a scaling with $\sim m^{22/3}$ for logarithmic total mass bins, implying that the highest mass

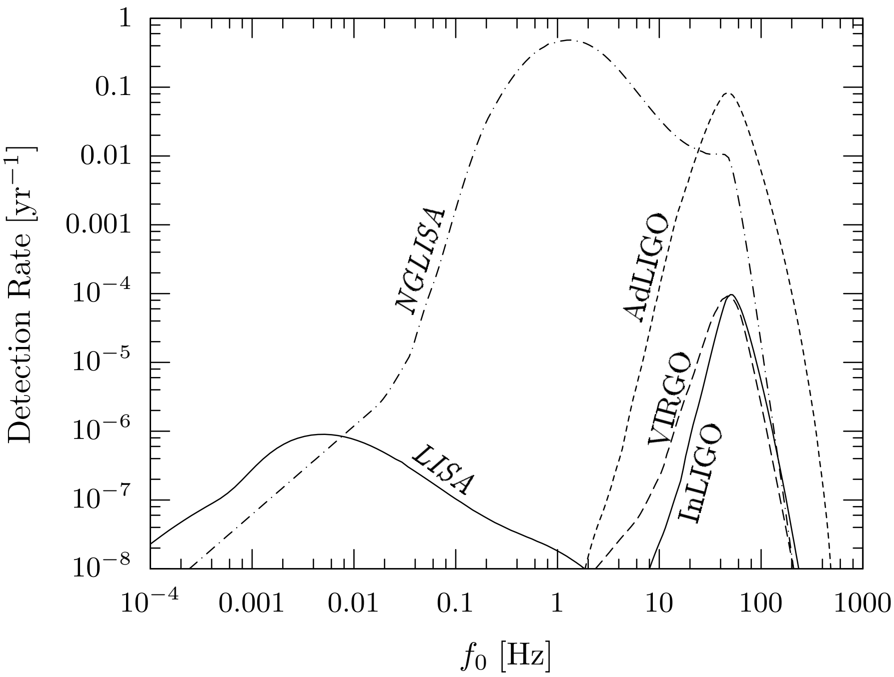

Figure 4.5 The expected PE detection rate per logarithmic emitted characteristic frequency bin. Results are shown for the specific detectors. All curves account for general relativistic encounters and cosmology. The units on the y-axis is simply yr^{-1}, since it is a rate per $\mathrm{d}\ln f_0 = \mathrm{d}f_0/f_0$ bins for which the units of f_0 drops out. For large f_0, there is an abrupt cutoff in the detection rate as the larger mass BHs suffer head-on collisions, leaving only the contribution of low-mass BHs in the PE rate.

BHs will dominate the PE event rates. However, increasing the BH masses decreases the maximum f_0 frequency of an encounter avoiding a collision. Figure 4.6 verifies that all of the detectors are indeed much more sensitive to large total masses, even though my model GC (i.e. Model II) contains a small relative number of these objects. Note, that the BH mass distribution $g_{\rm BH}(m)$ is constant for $\mathrm{d}\ln m$ bins. With Figure 4.6 the partial detection rates of BH–BH and NS–NS encounters can be visualized. For $M > 2m_{\rm min} = 10\mathrm{M}_\odot$ the BH–BH encounters dominate, while $M \approx 2m_{\rm NS}$ correspond exclusively to NS–NS encounters. PE detections of NS–NS encounters are practically impossible, they are suppressed by at least 9 orders of magnitudes. Similarly, Figure 4.7 shows that BH–NS encounters are also suppressed by 6 orders of magnitudes!

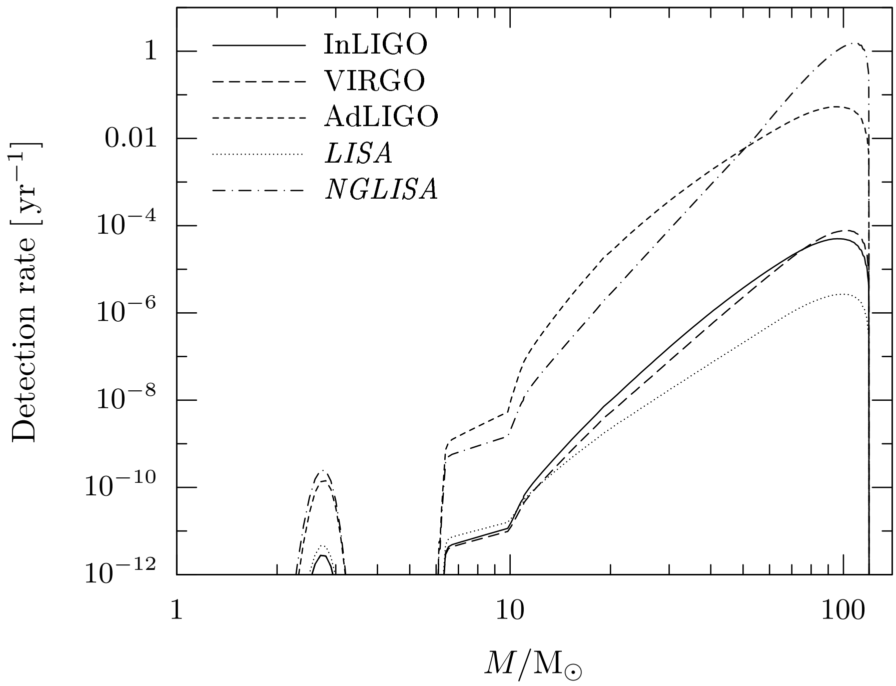

Figure 4.6 The expected PE detection rate per logarithmic total mass bins, $\mathrm{d}\ln M$, for the various detectors. Note that the mass function of my GC model is constant for $\mathrm{d}\ln m$ intervals for BHs $120\mathrm{M}_\odot > 2m > 10\mathrm{M}_\odot$, and is Gaussian type for NSs $2m \sim 2.7\mathrm{M}_\odot$. BH–NS encounters dominate for $6.35\mathrm{M}_\odot < M < 10\mathrm{M}_\odot$. The dominant PE contribution is expected from $m_{1,2} = 40 - 60\mathrm{M}_\odot$ component masses.

Figure 4.8 shows the detection rate as a function of minimum distance, $\lambda_{\rm min}$ of the encounters. Recall that for a given total mass M, λ determines the characteristic frequency f_0 by equation (4.33), and marginally plunging orbits correspond to $\lambda_{\rm min} = 2$. Figure 4.8 was obtained by changing the domain of integration of f_0 to $f_0 \lesssim f_{M,\lambda}$

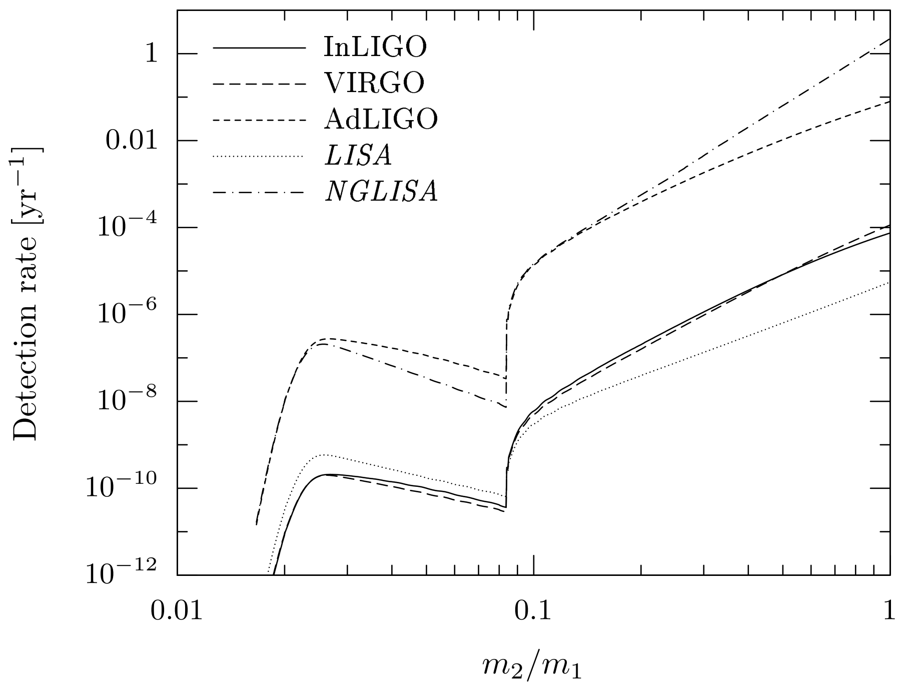

Figure 4.7 The expected PE detection rate as a function of the mass ratio $q = m_2/m_1$ of the interacting masses, where $m_1 \geq m_2$ is assumed. The partial PE detections are plotted per logarithmic mass ratio bins, $\mathrm{d}\ln q$, for the various detectors. Note that the assumed smallest and largest CO masses of my GC model implies a cutoff below $1.35\mathrm{M}_{\odot}/60\mathrm{M}_{\odot}$. The detection rate is dominated by equal mass encounters. PEs with $q > 5\mathrm{M}_{\odot}/60\mathrm{M}_{\odot}$ are dominated by BH–BH encounters, while $1.35\mathrm{M}_{\odot}/60\mathrm{M}_{\odot} \lesssim q < 5\mathrm{M}_{\odot}/60\mathrm{M}_{\odot}$ correspond to BH–NS events.

in equation (4.42). The curves show that terrestrial detectors are more sensitive to close approaches than space detectors. The $\lambda_{\min} = 2$ case corresponds to all of the PE detections. It is interesting to note, that terrestrial detectors display a different λ dependence: AdLIGO rates show a weaker increase for marginally colliding orbits $\lambda \sim 2$. This is a consequence of cosmology: the observation distance is so large (Figure 4.4) that the cosmological comoving volume element is significantly smaller, and the GW frequency is redshifted outside the sensitive domain of the detector for these events.

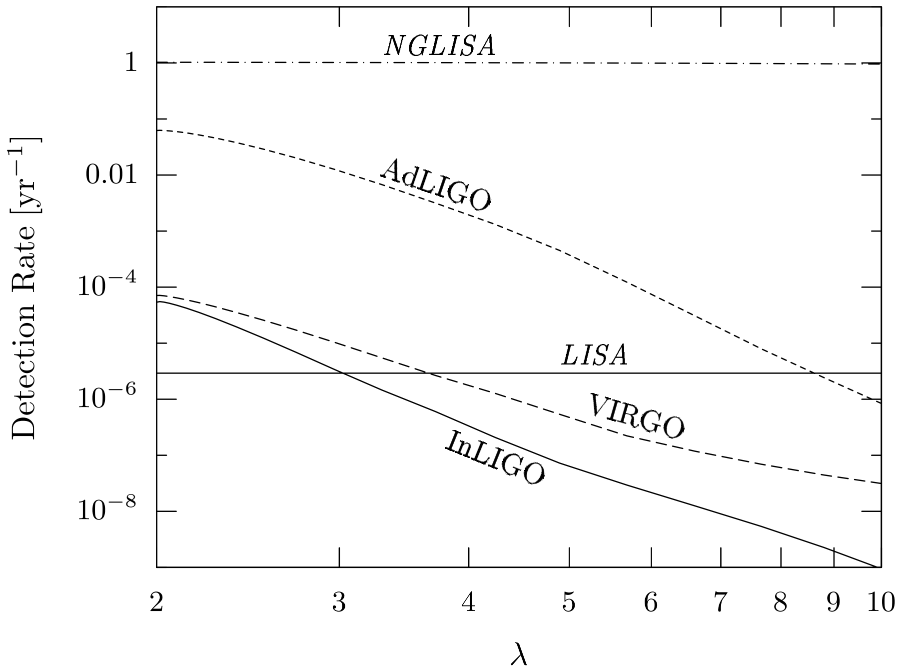

Figure 4.8 The total cumulative expected detection rate of PEs subject to the constraint that the minimum separation exceeds λ times the total Schwarzschild radius. For $\lambda < 2$ a head-on collision occurs, which I are not considering here (see Section 4.7.1 for a discussion).

4.6 Conclusions

PEs of solar BHs are possible sources of gravitational radiation. My results suggest that current and near future GW detectors are potentially capable of detecting these signals in the local universe and up to cosmological distances for the higher masses. I anticipate $S/N \gtrsim 5$ matched-filtering detection rates for quasi-parabolic trajectories avoiding collisions, $\nu^{\rm tot} = 5.5\times10^{-5}{\rm yr}^{-1}$ for InLIGO, $7.2\times10^{-5}{\rm yr}^{-1}$ for VIRGO, $0.063{\rm yr}^{-1}$ for AdLIGO, $2.9\times10^{-6}{\rm yr}^{-1}$ for *LISA*, and $1.0{\rm yr}^{-1}$ for *NGLISA*. For different signal-to-noise ratios, detection rates scale by approximately $(S/N)^{-3}$. These results correspond to a BH mass function $g_{\rm BH}(m)\propto m^{-1}$ with minimum and maximum masses of 5 and $60{\rm M}_{\odot}$. For comparison I ran calculations for more general distributions $g_{\rm BH}(m)\propto m^{-p}$, and different $m_{\rm min}$ and $m_{\rm max}$ values. Table 4.1 lists the results for these models. Here, I have fixed $N_{\rm BH}=500$ for models with $m_{\rm min}=5{\rm M}_{\odot}$. For larger $m_{\rm min}$, I reduce N_{BH} by assuming that BHs with masses $5{\rm M}_{\odot}\le m<m_{\rm min}$ have escaped the cluster. Results are very different for various choices of parameters (see Section 4.7.3 for a detailed discussion below).

I constructed two different GC models. I conclude that a uniform mass and density distribution (Model I) is inadequate since the contribution of the GC core consisting of the more massive BHs are significantly underestimated. After accounting for mass distribution and mass segregation, as well as the relative velocity distribution of the sources (Model II) I obtained event rates two orders of magnitudes higher than Model I per GC. Moreover, more massive BHs in GCs are visible to significantly larger distances, and supply the most prominent sources of PEs for detection (Figure 4.6).

In Section 4.7, I include a critical review of my assumptions and their influence on the results. To point out just one thing, note that compared to my previous estimates above, the PE detection rates might have been underestimated by four orders of magnitudes for core-collapsed GCs (depending on the final core radius and population, see Section 4.7.3 below)!

4.7 Discussion

4.7.1 Comparison with Other Orbits

How do PE event rates compare to the event rates of binary inspirals, mergers, and head-on collisions? What are the main factors for the difference? I briefly discuss these questions in this section.

Basic Features of Parabolic Encounters

Let us quickly summarize the main properties of PE sources.

Table 4.1. Detection rates for alternative models

p	$m_{\max}$ [$M_\odot$]	$m_{\min}$ [$M_\odot$]	$\nu_{\rm InLIGO}$ [yr^{-1}]	$\nu_{\rm VIRGO}$ [yr^{-1}]	$\nu_{\rm AdLIGO}$ [yr^{-1}]	ν_{LISA} [yr^{-1}]	ν_{NGLISA} [yr^{-1}]
0	20	5	1.0 (−6)	5.2 (−7)	2.2 (−3)	8.7 (−8)	6.3 (−4)
0	60	5	2.2 (−4)	3.1 (−4)	2.4 (−1)	1.2 (−5)	5.2
0	60	40	1.3 (−4)	2.1 (−4)	1.3 (−1)	7.2 (−6)	4.3
0	100	5	1.0 (−3)	3.6 (−3)	1.3	1.3 (−4)	
0	100	40	9.5 (−4)	3.4 (−3)	1.2	1.2 (−4)	
0	100	80	2.4 (−4)	1.2 (−3)	3.4 (−1)	4.3 (−5)	
1	20	5	4.8 (−7)	2.4 (−7)	1.0 (−3)	4.5 (−8)	2.7 (−4)
1	**60**	**5**	**5.5 (−5)**	**7.2 (−5)**	**6.3 (−2)**	**2.9 (−6)**	**1.0**
1	60	40	2.5 (−5)	3.9 (−5)	2.6 (−2)	1.3 (−6)	7.6 (−1)
1	100	5	2.2 (−4)	6.4 (−4)	2.8 (−1)	2.4 (−5)	
1	100	40	1.8 (−4)	5.7 (−4)	2.2 (−1)	2.0 (−5)	
1	100	80	2.9 (−5)	1.4 (−4)	4.2 (−2)	5.2 (−6)	
2	20	5	1.8 (−7)	9.1 (−8)	4.1 (−4)	2.1 (−8)	9.5 (−5)
2	60	5	6.6 (−6)	7.2 (−6)	8.3 (−3)	3.7 (−7)	8.4 (−2)
2	60	40	1.8 (−6)	2.8 (−6)	1.9 (−3)	1.0 (−7)	5.0 (−2)
2	100	5	1.7 (−5)	3.6 (−5)	2.1 (−2)	1.5 (−6)	
2	100	40	9.7 (−6)	2.7 (−5)	1.1 (−2)	9.6 (−7)	
2	100	80	8.9 (−7)	4.3 (−6)	1.3 (−3)	1.6 (−7)	

Note. — The number of BHs per GC is normalized to $N_{\rm BH} = 500$ for $m_{\min} = 5{\rm M}_\odot$ for all choices of $m_{\max}$. For larger $m_{\min}$, all BHs with $5{\rm M}_\odot \leq m < m_{\min}$ are assumed to have escaped from the cluster. Detection rates are given in normal form, where the exponent is shown in parenthesis. Some fields left blank correspond to cases where the S/N is not a monotonically decreasing function of distance (see Section 4.5.3).

- The event rates for $\mathrm{d}\ln f_0$ intervals scale with $f_0^{-2/3}$ for trajectories avoiding collisions. Collisions decrease PE event rates quickly for large frequencies, $f \gtrsim 50$Hz, rates drop four orders of magnitudes between 50 and 500Hz.

- The f_0-scaling of the amplitude of the signal is $f_0^{-1/3}$ for GW frequencies $f \sim f_0$. The integrated RSS signal amplitude scales with $f_0^{1/6}$.

- The signal energy-spectrum is broadband, has a maximum at $f \sim f_0$, and a relatively shallow cutoff for larger frequencies. The half-maximum of the signal is $\Delta f \sim 1.5 f_0$, and the spectral energy density drops to 1% at $f \sim 5 f_0$ (Turner, 1977).

- In terms of detections for $\mathrm{d}\ln f_0$ intervals, the maximum distance of PE detections for a band-pass detector is roughly independent of frequencies between $f_{\min} \lesssim f_0 \leq f_{0\,\max}$, where $f_{\min}$ is the minimum detectable frequency of the detector and $f_{0\,\max}$ is the maximum characteristic frequency of a PE avoiding collisions.

- The detection rates of equal-mass PEs scale with $\langle m^{22/3} \rangle$ for $\mathrm{d}\ln m$ intervals, the higher mass BHs dominate PE detections.

- Space detectors will possibly detect more PE events in the local universe, but terrestrial detectors see further.

- Typical event rates at $f_0 = 50$Hz are $1.6 \times 10^{-12}\mathrm{yr}^{-1}\mathrm{GC}^{-1}$ which corresponds to $\mathcal{R} = 1.4 \times 10^{-11} h^3 \mathrm{yr}^{-1}\mathrm{Mpc}^{-3}(\Delta \ln f_0)^{-1}$.

- Typical maximum distance of detection for PEs *with appropriate* f_0 is ~ 300Mpc for InLIGO and VIRGO, $z \sim 1$ for AdLIGO, ~ 0.4Mpc for *LISA*, and $z \sim 0.2$ for *NGLISA*.

- Typical overall rate of PE detections per year is $\sim 10^{-4}$ for InLIGO and VIRGO, ~ 0.1 for AdLIGO, $\sim 10^{-6}$ for *LISA*, and ~ 1 for *NGLISA*.

Parabolic Encounters vs. Inspirals

The event rates of PEs depend on the characteristic frequency. Without any specifications PEs are more regular than e.g. BH–BH inspirals. However, *within the sensitive range* of GW terrestrial detectors PEs are rather rare by a factor of $\sim 10^{-4}$. Event rates are higher for space detector frequencies, however space detectors have a smaller distance of maximum observation.

Kocsis et al. (2006) suggests that the detectable distance of PEs is comparable to inspirals. However, this is somewhat deceptive since PE results correspond to larger BH masses, $50M_\odot$ rather than $10M_\odot$ which is regular for BH–BH inspirals in the literature. For $10M_\odot$ component masses, the maximum distance of observation is less for PEs than for inspirals (Figure 4.4), the PE event rates are suppressed by a factor of $\sim 10^3$ (Figure 4.6). However for larger masses the comparison changes with the following factors. First, although the GW signal amplitude is proportional to $\mathcal{M}^{5/3}$ for inspirals, increasing the masses reduces the signal frequency (which in turn reduces the detector sensitivity) and also reduces the observation time (which also decreases the effective signal amplitude). Another important difference is in the binary separation λ which determines the signal frequency. It is restricted to $\lambda > 3$ for inspirals, the innermost stable circular orbit, a more stringent constraint than the condition $\lambda > 2$ for PEs (see Section 4.5.2). Finally opposed to the PE signal waveforms, the inspiral signals are narrow band, implying that the high mass, i.e. low frequency, inspiral waveforms are much harder to detect as much smaller signal power accumulates at the more sensitive range of frequencies. When combining all of these effects I expect that low mass BH inspirals are detectable further with terrestrial detectors, while for large masses where the observation is limited to at most a few orbits, marginally collisional PEs are better detected. Therefore, detectors can observe the higher mass encounters for PEs. This is exactly analogous to the comparison of the inspiral and plunge phases of binary coalescence, for which the detection of plunge dominates for large masses (Flanagan & Hughes, 1998).

Among the GW detection candidate sources in GCs, PEs are very infrequent compared to stellar BH–BH inspiral rate estimates of Portegies Zwart & McMillan (2000) or Miller (2002) within GCs, but are comparable to the recent results of O'Leary et al. (2006). Observations of radio pulsars and gamma ray bursts suggest several orders of magnitude larger numbers for NS–NS or BH–NS inspiral detections (Kalogera et al., 2004; Nakar et al., 2006).

Parabolic Encounters vs. Head-on Collisions

As a second example, let us consider the event rates of head-on collisions for unbound encounters. Head-on collisions are related to PEs, by extending the parameter λ to values less than 2, the unstable circular orbit. Thus it would be relatively straightforward to extend the analysis to these events, by examining the event rates for small initial impact parameters, and computing the detectability as a function of this parameter. However, the exact shapes of gravity waveforms are presently not available for collisions (see Baker et al. 2006 for current progress), therefore maximum likelihood detections are not possible, and the detection of these bursts requires much higher signal-to-noise levels. I shall argue that direct head-on collision detections are potentially less frequent than PEs.

The rate of head-on collisions between BHs is well known, (see e.g. Hills & Day, 1976; Cutler et al., 1994; Sigurdsson & Rees, 1997) however the detection rates of the resultant GW signals is subject to the uncertainty of the GW signals (Flanagan & Hughes, 1998). Direct collisions produce potentially less intensive GW signals than close PEs even if neglecting the relativistic amplitude enhancement for PEs. To see this, let us compare GW signal strengths that I adopt for PEs (see Section 4.3, and Gair et al., 2005; Martel, 2004; Turner, 1977), with general relativistic calculations for head-on collisions. To my best knowledge, off-axis collisions of BHs have not been calculated as a function of impact parameter. For radial head-on collision of Schwarzschild BHs $\Delta E \simeq 0.01\,(\mu^2/M)\,\mathrm{c}^2$ (Anninos et al., 1993; Davis et al., 1971; Moreschi, 1999; Sperhake et al., 2005). Sasaki & Nakamura (1982) derived GW energies for the radial infall of a test particle into a Kerr BH, and Mino et al. (1996) accounted for the spin of the infalling particle in addition. Results are in the range of $\Delta E = 0.03 - 0.01\,(\mu^2/M)\,\mathrm{c}^2$ according to the magnitude and alignment of spins and the relative direction of the approach. For high-velocity head-on collisions, there are significantly larger results: $\Delta E = 0.328\,\mu\mathrm{c}^2$ for non-rotating BHs (D'eath & Payne, 1992), and up to $\Delta E = 0.70\,\mu\mathrm{c}^2$ for extreme Kerr-BHs (Cardoso & Lemos, 2003). However, in GCs the initial velocities are typically non-relativistic, therefore I do not expect a significant relative contribution of relativistic head-on collisions. Once the BHs are so near that a common surrounding horizon envelope forms the space-time relaxes to a Kerr-BH. The energy output of this process is between $\Delta E = 6 \times 10^{-6} M\,\mathrm{c}^2$ (Price & Pullin, 1994) for axisymmetric encounters and $\lesssim 0.01 M\,\mathrm{c}^2$ for quasi-circular initial conditions (Khanna et al., 1999). In comparison, the energy output in GWs for non-relativistic PEs is $\Delta E_{\mathrm{PE}} = 0.01\,(\lambda/4.1)^{-7/2}\,(\mu^2/M)\,\mathrm{c}^2$ (Turner, 1977). Using the low-velocity case, the GW amplitudes of BH collisions are overestimated by the Newtonian results by a factor between $(\lambda/3)^{-7/2}$ and $(\lambda/4)^{-7/2}$, depending on spins. Therefore, the extapolation of the Newtonian treatment to the regime where the minimum separation is $\lambda \ll 3$ leads to significant overestimates of the true head-on collision GW energies. In conclusion, the extrapolation of event rates as a function of λ (for $\lambda < 2$ in Figure 4.8) or as a function of the logarithmic characteristic frequency (for $f_0 > f_{\lambda=2}$ in Figure 4.4, dotted lines) is possibly overly optimistic and therefore inadequate for the estimation of the detection rates of head-on collisions with the particular GW detectors.

4.7.2 Approximations in the Analysis

My event rate estimates rely on several approximations. The most important caveat in my analysis is possibly neglecting GW recoil capture in bound eccentric orbits. The GW radiation reaction is substantial for strong gravitational fields, for low λ. For initially nearly parabolic orbits, the periastron distance and the eccentricity is decreased[12] (Cutler et al., 1994). The first consequence is a minor decrease in the PE event rate, because of the increase of the cross-section of direct capture. On the other hand, GW recoil produces bound orbits from initially unbound trajectories (Lee, 1993). The periastron distance is then further decreased during each subsequent close approach inducing successively stronger GW radiation. Therefore PE events are potential precursors of multiple subsequent more intense highly eccentric bound encounters, analogous to the captures of stellar compact objects by supermassive black holes (Hopman & Alexander, 2005). The GW detection rate of the resultant orbits is likely to be significantly higher than PE detections. As a result, I anticipate several successful detections for AdLIGO per year for a wide range of BH mass-distribution models (see Tab. 4.1 for PEs without GW recoil capture). I leave a detailed quantitative study for future work.

There is a second independent reason suggesting that higher detection rates will be more likely. Throughout this work, I estimated matched filtering detection signal-to-noise amplitudes with the angular averaged formula which is valid for an analysis using only a single GW detector. However, a coincident analysis incorporating several detectors allows much more optimistic detection limits (see Jaranowski et al., 1996, and Section 4.3 above). If lowering the angular averaged minimum detection limit to $S/N = 3/\sqrt{5}$ (equivalent to an optimal-orientation single-detector observation at $S/N = 3$) yields $\nu^{\rm tot} = 1.7 \times 10^{-3}{\rm yr}^{-1}$ for InLIGO, $2.7 \times 10^{-3}{\rm yr}^{-1}$ for VIRGO, $0.46{\rm yr}^{-1}$ for AdLIGO, and $9.5 \times 10^{-6}{\rm yr}^{-1}$ for *LISA* for my standard GC Model II with $N_{\rm BH} = 500$, $p = 1$, $m_{\rm min} = 5{\rm M}_\odot$, and $m_{\rm max} = 60{\rm M}_\odot$. For models with larger $m_{\rm max}$ detection rates are even higher (see Tab. 4.1), implying several successful detections per year for advanced terrestrial detectors.

I have also neglected the bound binary interactions in the scattering dynamics and

[12]unless $\lambda \gtrsim 2.05$, in which case the eccentricity is increased by GW recoil

restricted only to single-single encounters. Depending on the angle of injection this could increase or decrease event rates. However my analysis of single–single interaction shows (Section 4.5.1), that the typical numerical values for PE cross-sections are extremely small, so that the injection has to have an initial velocity very accurately pointed towards the target CO in order to produce a detectable signal. For typical encounters with $m_1 = m_2 = 50\mathrm{M}_\odot$ and $f_0 = 50\mathrm{Hz}$, the minimum separation is $b_0 \sim 10^{-6}\,\mathrm{AU}$, and the impact parameter is $b_\infty \sim 10^{-2}\,\mathrm{AU}$. As a result, for single–binary interactions I speculate that the separation of scales is possible to distinguish three independent phases of the interaction: (i) the faraway zone $r \gg a_{\rm bin}$, (ii) the intermediate zone $r \sim a_{\rm bin}$, and (iii) the PE zone $r \sim b_0 \ll a_{\rm bin}$. In (iii) the binary companion can be discarded. Moreover, note that the velocity during (ii) is still negligible compared to (iii). Therefore in practice, the beginning of phase (iii) is exactly analogous to the initial conditions of a single–single encounter. The only difference is the distribution of velocities is not isotropic, but after phase (i) it is beamed toward the center of mass, and phase (ii) adds a random deflection due to the companion. Plugging in the numbers for binary separations of $a_{\rm bin} \gg 10^{-2}\,\mathrm{AU}$ I conclude, binary focusing is not likely to significantly modify my PE rate estimates. Numerical simulations would be needed to determine the exact modifications in the estimates.

Binary interactions also alter the total number and mass distribution of BHs in the cluster. However in my calculations the total number and mass function of BHs are input parameters, which can be chosen consistently with the most sophisticated simulations.

Throughout this analysis I assumed simplified GC models. While my most sophisticated model accounts for the mass distribution, mass segregation, and relative velocities (see Section 4.4.3) it does not consider the nonuniform radial distribution of density of regular stars in the cluster core, nor does it consider variations around the characteristic GC model parameters (e.g. virial radius, total mass, etc). However, the final results are simple powers of the characteristic parameters ($\nu \propto q^2 N_{\rm tot}^{1.5} R^{-2.5}$). My treatment allows upper and lower bounds to be made on the exact GC model detection rates. These bounds are still much tighter than other sources of uncertainties, which justifies the simplifying model assumptions in this analysis.

Another major approximation was to adopt the angular averaged signal waveforms in the Newtonian approximation (Turner, 1977), and corrected for the relativistic enhancement of the amplitude, substantial for close-encounters. I adopted the relativistic correction for the quadrupole radiation of a test particle geodesics (Gair et al., 2005; Martel, 2004) and extrapolated results for other masses. These estimates do not account for GW recoil. However, Figure 4.8 shows that the contribution of extreme zoom-whirl orbits $\lambda \approx 2$ does not ruin my estimates, since the detection rate does not increase substantially for marginally plunging orbits. GW recoil reduces PE signal-power by driving the interacting masses to collisions, thereby terminating extreme zoom-whirl orbits much sooner than the no-recoil encounter time (Gair et al., 2006). I conclude that neglecting GW recoil did not lead to a large overestimate, implying that my results are acceptable approximations in this respect.

An exact treatment would have to utilize the more exact post-newtonian waveforms of the general problem using arbitrary masses and spins, and should take into account the forward peaking of GWs for high velocities, Doppler shift of GW frequencies, spin-orbit, and spin-spin interactions, etc. Although it is clear that a real data analysis matched filtering would have to be carried out with exact signal templates, the leading-order (i.e. Newtonian) term dominates the angular averaged signal power, which is therefore an adequate first estimate for the detection rates.

4.7.3 Uncertainties in the Result

Model Parameters

There are several theoretical uncertainties in my estimate. Among the most important uncertainties are the values of the GC model parameters, like the number of BHs in the cluster $N_{\rm BH}$. Portegies Zwart & McMillan (2000) derives $q_{\rm BH} = N_{\rm BH}/N_{\rm tot} = 6 \times 10^{-4}$ by using Scalo (1986) initial mass function (IMF) and assumed that every object more massive than $20{\rm M}_\odot$ up to $100{\rm M}_\odot$ had evolved to a BH. When using a Salpeter IMF, the result is $q_{\rm BH} = 10^{-3}$ (Miller, 2002), and Kroupa & Weidner (2003) IMF gives $q_{\rm BH} = 1.5 \times 10^{-3}$ (O'Leary et al., 2006). I adopt the most conservative result of Portegies Zwart & McMillan (2000). However there is a chance that a non-negligible fraction of the stars have been ejected from the cluster or have undergone subsequent mergers. Both processes increase the estimate on the final BH fraction (Miller, 2002). On the other hand dynamical binary interactions, binary recoil kicks, or GW recoil of BH mergers can eject BHs, thereby reducing their overall numbers and possibly also modify the mass-distribution. In fact, a significant portion of the stellar-mass BH population might be ejected, especially in small clusters (O'Leary et al., 2006; Portegies Zwart & McMillan, 2000; Sigurdsson & Hernquist, 1993). Belczynski et al. (2006) find that for an initial binary fraction of 50%, the retained fraction of BHs varies between 0.4 and 0.7. In my fiducial calculations I adopted $q_{\mathrm{BH}} = 5 \times 10^{-4}$ and $N^{\mathrm{tot}} = 10^6$. To see the effects of BH ejection, Tab. 4.1 shows results for other models. For the general case, I provide analytical scalings which can be readily used in case these parameters are better determined in the future. For example since $\nu^{\mathrm{tot}} \propto N_{\mathrm{BH}}^2$, for $N_{\mathrm{BH}} = 5000$ (50) detection rates increase (decrease) by a factor of 100.

Black Hole Mass Distribution

An even more significant source of uncertainty is the mass distribution of BHs in the clusters. I have calculated detection rates for several distributions (Tab. 4.1). Increasing the p exponent of the distribution, $g_{\mathrm{BH}} \propto m^{-p}$, decreases the detection rate by a factor of ~ 5 for a unit change in p. Changing the maximum mass of the distribution varies the results even more significantly. Compared to the detection rate corresponding to $m_{\mathrm{max}} = 60\mathrm{M}_{\odot}$, for $m_{\mathrm{max}} = 100\mathrm{M}_{\odot}$ ($20\mathrm{M}_{\odot}$) I get a $\sim 1-3$ order of magnitude increase (decrease) depending on the detectors. I have also tried changing the minimum mass m_{min}, by assuming that the BHs with masses $m < m_{\mathrm{min}}$ have escaped from the cluster. Compared to $m_{\mathrm{min}} = 5\mathrm{M}_{\odot}$, a value of $m_{\mathrm{min}} = 40\mathrm{M}_{\odot}$ reduces detection rates by a factor of ~ 2. In the appendix, I provide ready-to-use formulas for calculating detection rates for other parameter values.

From the theoretical point of view, simulations of the initial stellar BH mass function (Fryer & Kalogera, 2001) result in a maximum mass limit of $\sim 20\mathrm{M}_{\odot}$, but the particular form of the mass function is very different for various assumptions (fraction of explosion energy used to unbind the star, stellar winds, mass transfer after helium ignition, etc). Recent simulations of rapid star evolution assuming a lower metallicity for the progenitor stars (weaker stellar winds) appropriate for GCs and including a large fraction of binaries, collisions, and accretion leading to the mass buildup of BHs imply a stellar-mass BH distribution with maximum BH masses around $M_{\mathrm{max}} = 60 - 100\mathrm{M}_{\odot}$ (Belczynski et al., 2006). Simulations of the subsequent long-term dynamical evolution has been shown to be sensitive to BH binary and triple interactions (O'Leary et al., 2006). Binary-single body interactions, BH-star collisions, and GW recoil kick can possibly significantly reduce the low mass BH population but enhance the mass of the most massive BHs in the cluster. From the observational point of view, there is yet lacking evidence for stellar mass BHs with $m > 20\mathrm{M}_{\odot}$, but this might be accounted for the low number statistics (a total of 20 X-ray stellar-mass BH candidates have been identified to date, Casares, 2006).

Core Collapse

Finally, a considerable uncertainty in the PE detection rates results from the actual scaling of the mass segregation relationships. Even in my complicated model I have assumed a simple mass segregation, based on thermal equipartition among the specific CO components. This assumption is in fact valid only among the decoupled high mass components within the core. Spitzer (1969) has shown that in simple two-component systems consisting of masses m_1 and m_2, with $m_1 \ll m_2$, global equipartition cannot be attained if the low-mass component determines the potential everywhere in the cluster. In this case, the high mass components become dynamically decoupled from the rest of the cluster, and the cluster core collapses to a much smaller radius, $R_{\rm core}$. This picture has been confirmed by numerical simulations for more general mass functions (Watters et al., 2000, and references therein). Atakan Gurkan et al. (2004) showed that approximate local thermal equipartition is attained within the core, and velocities follow $v_m = (Km/m_{\rm BH})^{-1/2} v_{\rm core}$, where $v_{\rm core}$ is the velocity dispersion, $m_{\rm BH}$ is the mass of components in the core, K describes the departure from equipartition, it is a number of order 1. The total time of the collapse and the final magnitude of core velocities or core radius, depends sensitively on the initial fraction of binaries. For a single mass cluster Heggie et al. (2006) found that $0.01 \lesssim R_{\rm core}/R_{\rm gc} \lesssim 0.1$, larger values valid for a large fraction of binaries (here $R_{\rm gc}$ is the half-mass radius). In contrast my simple mass segregation led to $R_{50{\rm M}_\odot} = 0.14 R_{gc}$, which is a factor 1.4–14 higher. Note, that the virial theorem implies $v_m \propto R_m$ for a homogeneous mass distribution. Detection rates scale with $R_m^{-3} v_m^{-1}$, and the contribution of $m \sim 50{\rm M}_\odot$ dominated the final results (see Figures 4.6 and 4.7). Therefore post-core collapse mass segregation implies detection rates increased by $(1.4)^4$–$(14)^4$. Thus, in the most optimistic case, I get a substantial increase in the detection rates, i.e. $2.1{\rm yr}^{-1}$ for InLIGO, $2.8{\rm yr}^{-1}$ for VIRGO, $6.6\,{\rm day}^{-1}$ for AdLIGO, $0.1{\rm yr}^{-1}$ for *LISA*, and $4.4\,{\rm hr}^{-1}$ for *NGLISA*!

On the other hand, if core collapse leads to runaway collisions and the buildup of a single intermediate mass black hole, while stellar mass BHs are ejected from the cluster (Freitag et al., 2006), PE detection rates might be considerably suppressed after collapse (i.e. $\nu \propto N_{\rm BH}^2$). More information on the typical properties and long-term evolution of core collapsed clusters is needed to make PE detection rates less uncertain.

4.7.4 Implications

Opening the gravitational-wave window to observe parabolic encounters of black holes in globular clusters offers a new possibility to constrain BH mass functions and GC models. Since PEs are very sensitive to the number of higher mass stellar BHs (Figures 4.6 and 4.7), my results indicate that a regular detection of PE events would provide accurate limits on the stellar BH mass distribution in GCs. My analysis shows that this might be possible with AdLIGO if average GCs carry at least 500 BHs.

Galactic Nuclei

The analysis can be extended for other spherically symmetric systems using the scaling $\nu \propto N_{\rm BH}^2 n_{\rm system} v_{\rm vir}^{-1}$. Consider first galactic nuclei, hosting 2500 BHs and approximately all of these BHs have undergone mergers (Portegies Zwart & McMillan, 2000). Galactic nuclei abundance in the universe is 100 times less than for GCs (Section 4.4.2). Assuming that the virial velocity is a factor of $\sqrt{10}$ higher in galactic nuclei and that the CO mass function has the same distribution as in GCs, I get detection rates $\nu^{\rm gal} = 5^2 \times 1/100 \times 1/\sqrt{10} \times \nu^{\rm gc}$. However, the large number of BH mergers likely increases BH masses in galactic nuclei. For a uniform distribution (i.e. $p = 0$) of $N_{\rm BH} = 2500$ between $m_{\rm min} = 80$ and $m_{\rm max} = 100\mathrm{M}_\odot$ I get $2500^2/[500 \times (100-80)/(100-5)]^2 \times 1/(100\sqrt{10}) = 1.8$ times the rates shown in the corresponding row of Tab. 4.1 for GCs: $4. \times 10^{-4}\mathrm{yr}^{-1}$ for InLIGO, 2.1×10^{-3} for VIRGO, $0.61\mathrm{yr}^{-1}$ for AdLIGO, and $5.2 \times 10^{-6}\mathrm{yr}^{-1}$ for *LISA*. These numbers should only be regarded as rough estimates, since they result from the direct application of simplified GC model assumptions to galactic nuclei. The calculation assumed uncorrelated two-body interactions which does not hold for motion in the potential of galactic centers (Rauch & Tremaine, 1996).

Primordial Black Holes in Galaxies

For a second example consider the GW detections from galactic haloes comprised of low-mass primordial BHs (PBHs) (see e.g. Abbott et al. 2005c and references therein). For a quick upper-limit estimate on the PE detection rate I repeat my analysis for GCs by changing the model parameters to describe galactic haloes. I assume $N_{\rm PBH} = 10^{11}$ PBHs within a maximum radius $R = 5\,\mathrm{kpc}$, a virial velocity $v_{\rm vir} = 220\,\mathrm{km/s}$, and a uniform distribution of masses between $m_{\rm min} = 0.25\mathrm{M}_\odot$ and $m_{\rm max} = 0.95\mathrm{M}_\odot$. The maximum distance of a matched filtering detection at a characteristic frequency of $0.9 f_{M\,\max} = 4260\text{Hz}$ with angular-averaged signal-to-noise ratio $S/N = 5$ is 0.33, 0.62, 4.5, 0, and 0.06Mpc for InLIGO, VIRGO, AdLIGO, *LISA*, and *NGLISA*, respectively. The final result for the detection rate after the compilation of the full analysis described above gives $\nu = 1.5 \times 10^{-11}$, 1.6×10^{-11}, 2.9×10^{-10}, 2.6×10^{-11}, and 1.4×10^{-9}, respectively. These numbers are comparable to the total NS–NS PE rate in GCs. It is 9 orders of magnitudes smaller than the event rates estimates for PBH binary coalescence in one Milky Way sized galaxy (Abbott et al., 2005c; Ioka et al., 1998).

Unresolved Parabolic Encounter Background

Another extension of the present analysis is to estimate the number of low S/N PE events, which possible add an unresolved astrophysical background to the GW detector noise budget similar to the unresolved WD background (Benacquista et al., 2004; Cornish & Crowder, 2005; Hils et al., 1990; Nelemans et al., 2001) and unresolved capture sources (Barack & Cutler, 2004a). Since PE rates are progressively larger for progressively smaller characteristic frequencies, f_0, and since all PE waveforms extend to GW frequencies $f \lesssim f_0$, PE background will be most substantial for space detectors, especially around the minimum frequency noise wall ($f_{\min} = 10^{-5}$–10^{-4}Hz). The total number of PE events within a distance D, can be obtained from equation (4.19) neglecting cosmology as

$$R = \frac{4\pi}{3} D^3 n^{\rm gc} \int_{f_{\min}}^{f_{\max}} \mathrm{d}\nu^{\rm II} \approx 2\pi D^3 n^{\rm gc} \nu_1^{\rm II} \left(\frac{f_{\min}}{f_{100}}\right)^{-2/3} \tag{4.43}$$

where $f_{\max}$ is the maximum frequency for PEs avoiding a collision, equation (4.32), which drops out to leading order if $f_{\min} \ll f_{\max}$. For $D = 10\,\text{Gpc}$ and $f_{\min} = 10^{-5}$Hz (10^{-4}Hz) I get one event every $1/R = 19\,\text{sec}$ ($88\,\text{sec}$), which corresponds to $k = 5300$ (110) events for a 10^{-5}Hz (10^{-4}Hz) frequency bin. If core contraction enhances PE rates by a factor of 14^4 (see Section 4.7.3), I get $k = 2 \times 10^8$ (4×10^6) events per frequency bin.

These events will typically have a very low signal-to-noise ratio, e.g. for a single PE encounter with $f_0 = 10^{-5}$Hz for $m_1 = m_2 = 50\text{M}_\odot$ at $d_{\rm L} = 10\,\text{Gpc}$ I get $(S/N)_1 \sim 8 \times 10^{-9}$, and $f_0 = 10^{-4}$Hz yields $(S/N)_1 \sim 2 \times 10^{-7}$ for *LISA*. Assuming that average unresolved PE noise accumulates proportional to $\sqrt{k}$, I get a net amplitude of only $(S/N)_{\rm net} = 10^{-4}$ or 5×10^{-4} for *LISA* even in the core contracted case for frequencies 10^{-5}Hz or 10^{-4}Hz, respectively. Thus, I anticipate that the unresolved PE background adds a negligible amount to the *LISA* noise, and the unresolved PE background from stellar BH encounters will not be an issue for near-future extensions either.

Chapter 5

Concluding Remarks and the Doctoral Theses

I conclude the dissertation with a bulleted list of the most important findings presented in this work.

5.1 Quasar counterparts

1. I have considered the possibility that SMBH-SMBH mergers, detected as gravitational wave sources by LISA, are accompanied by gas accretion and quasar activity with a luminosity approaching the Eddington limit. Under this assumption, I have computed the number of quasar counterparts that would be found in the three–dimensional error volume provided by LISA for a given GW event, for various masses and redshifts.

2. I computed the expected uncertainties caused by the LISA noise, cosmological parameters, peculiar velocities, and weak gravitational lensing as a function of redshift. I found that weak lensing errors exceed other sources of uncertainties on the inferred redshift of the EM counterpart and increase the effective error volume by nearly an order of magnitude.

3. I have proposed a new method to correct for the weak lensing uncertainties by accounting for the matter distribution on large scales and calculated its efficiency. The residual weak lensing uncertainties were found to remain the major limitations of the localization of the redshift.

4. Nevertheless, I found that for mergers between $\sim(4\times10^5-10^7)\mathrm{M}_\odot$ SMBHs at $z\sim1$, the error box may contain a single quasar with a B-band luminosity $L_B = (10^{10}\text{–}10^{11})\mathrm{L}_\odot$. Furthermore this allows to test the hypothesis that the counterparts to SMBH merger events are quasars.

This would make the identification of unique EM counterparts feasible, allowing precise determinations of the Eddington ratio of distant accreting SMBHs, and providing an alternative method to constrain cosmological parameters.

5.2 Evolution of parameter estimation accuracy

5. I have developed a new harmonic mode decomposition (HMD) method to study the feasibility of using LISA inspiral signals to locate coalescing SMBH binaries on the sky, as the mergers proceed. This method is three order of magnitudes faster to calculate the time evolution of the parameter estimation covariance matrix.

6. I have developed toy models and found a way to comprehend the evolution of parameter errors. I found that exactly 4 combinations of the physical parameters improve throughout the observation with the signal to noise ratio. Marginalized errors cease to improve near merger.

7. I have explored in detail how the GW source localization accuracy depends on the sky position, detector orientation, and observation time before merger. I found no significant systematic effect with sky position except in the orbital plane.

8. According to my extensive HMD survey of potential LISA sources, it will be possible to trigger large field-of-view searches for prompt EM counterparts during the final stages of inspiral and coalescence. My results indicate, for instance, that for a typical $z\sim1$ merger event with total mass $M\sim10^5-10^7\mathrm{M}_\odot$, a 10-day advance notice will be available to localize the source to within a $10\,\mathrm{deg}^2$ region of the sky. The advance notice to localize the source to a 10 times smaller area of $1\,\mathrm{deg}^2$ is <1 day for the typical event, suggesting that a wide–field instrument of the LSST class, with a $10\,\mathrm{deg}^2$ field-of-view, may offer significant advantages over a smaller, $1\,\mathrm{deg}^2$ field-of-view instrument for observational efforts to catch prompt EM counterparts to SMBH binary inspirals.

The robust identification of such EM counterparts would have multiple applications (Holz & Hughes, 2005; Kocsis et al., 2006), from an alternative method to measure cosmological parameters to precise measurements of merger geometries in relation to host galaxy properties. If such EM counterpart searches can be implemented effectively and successfully, LISA could become an extremely valuable instrument for astrophysics and cosmology, beyond the original general relativistic measurement goals. Given the advance warning time capabilities established here, effective strategies for EM counterpart searches, including the concept of partially dedicating a $\gtrsim 10\,\mathrm{deg}^2$ field-of-view fast survey instrument of the LSST class, can be considered in detail.

5.3 Expectations on Detecting GWs from Parabolic Encounter

9. I have considered an additional possibility of GW bursts produced during unbound orbits of stellar mass compact objects. I estimated the rate of successful detections for specific detectors: the initial Laser Interferometric Gravitational-Wave Observatory (InLIGO), the French-Italian gravitational-wave antenna VIRGO, the near-future Advanced-LIGO (AdLIGO), the space-based *Laser Interferometric Space Antenna* (*LISA*), and the *Next Generation LISA* (*NGLISA*). The dominant contribution among unbound orbits that have GW frequencies in the sensitive band of the detectors correspond to near-parabolic encounters (PEs) within globular clusters (GCs). I have constructed simple GC models to account for the compact object mass function, mass segregation, number density distribution, and velocity distribution.

10. I found that typical PEs with masses $m_1 = m_2 = 40\mathrm{M}_\odot$ are detectable with matched filtering over a signal to noise ratio $S/N = 5$ within a distance $d_L =$ 200Mpc for InLIGO and VIRGO, $z = 1$ for AdLIGO, 0.4Mpc for *LISA*, and 1 Gpc for *NGLISA*.

11. I estimated single datastream total detection rates of $5.5 \times 10^{-5}\mathrm{yr}^{-1}$ for InLIGO, $7.2 \times 10^{-5}\mathrm{yr}^{-1}$ for VIRGO, $0.063\mathrm{yr}^{-1}$ for AdLIGO, $2.9 \times 10^{-6}\mathrm{yr}^{-1}$ for *LISA*, and $1.0\mathrm{yr}^{-1}$ for *NGLISA*, for reasonably conservative assumptions.

12. I gave ready-to-use formulas to recalculate the estimates when these input parameters become better-determined.

These estimates are subject to uncertainties in the GC parameters, most importantly the total number and mass-distribution of black holes (BHs) in the cluster core. In reasonably optimistic cases, I get $\gtrsim 1$ detections for AdLIGO per year. I can expect that a coincident analysis using multiple detectors and accounting for GW recoil capture significantly increases the detection rates. The regular detection of GWs during PEs would provide a unique observational probe for constraining the stellar BH mass function of dense clusters.

Appendix A

Parameters Estimation Errors in Nonstationary Noise

A.1 Simple Toy Models

A.1.1 Single Frequency Model

First, let us consider the following simple model with two unknowns, c_0 and c_1,

$$h(t) = c_0 + c_1 \cos(2\pi f_\oplus t), \tag{A.1}$$

where $f_\oplus \equiv \mathrm{yr}^{-1}$ is fixed and assumed to be known prior to the observation. I call t the "look–back time" before merger. Let us assume that the relative noise continuously decreases during the observation and that the differential squared signal-to-noise ratio (without modulation) is given by $\sigma^{-2}(t) = t^{-2}$ in eq. (3.50). Here $t = 0$ is a proxy for the "merger". Close to merger, the signal-to-noise ratio accumulates very rapidly. I assume that $h(t)$ is measured in the time interval $t_\mathrm{i} \geq t \geq t_\mathrm{f}$, where t_i is the start of observation, t_f is the end of observation (i.e. $x = t_\mathrm{merger} - t$, $x_\mathrm{min} = t_\mathrm{f}$, and $x_\mathrm{max} = t_\mathrm{i}$ in eq. [3.50]). I fix t_i and examine the dependence of parameter estimation errors as a function of t_f, assuming $t_\mathrm{f} \ll t_\mathrm{i}$.

Note that, for the signal (A.1), the fiducial values (c_0, c_1) drop out when calculating the RMS parameter errors Δc_0 and Δc_1 using eq. (3.50). More generally, this is true for any signal which is a linear combination of the unknown parameters. All our toy models

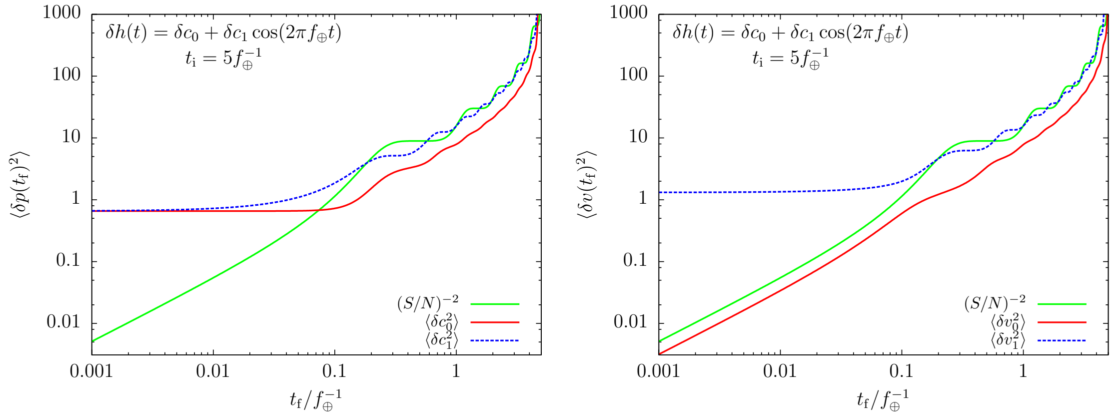

Figure A.1 Marginalized parameter errors *(top)* and principal errors *(bottom)* for the single frequency model. The green curve shows the scaling with inverse squared signal-to-noise ratio, $(S/N)^{-2}$, for reference on both plots. A total observation of $t_\mathrm{i} = 5\mathrm{yr}$ is assumed. Marginalized errors follow the signal-to-noise ratio for large t_f, but they stop improving within $t_\mathrm{f} < t_\mathrm{c} \sim 0.1\mathrm{yr}$ from merger. Only one eigenvalue scales with the signal-to-noise ratio near merger.

will have this property and the results presented in this section will be general in that respect.

First, let us substitute (A.1) in (3.49) and (3.50), and evaluate the expected co-variance matrix numerically. Figure A.1 displays the time dependence of marginalized parameter errors and principal errors. The plots show that the parameter errors all decrease with the signal to noise ratio when the look–back time before merger is large. However if the end of the observation is within a certain critical time to merger, $t_\mathrm{f} < t_\mathrm{c}$, only one principal component follows the signal-to-noise ratio. Figure A.1 shows that $t_\mathrm{c} \sim 0.1\mathrm{yr}$. The start of the observation in Figure A.1 was fixed at $t_\mathrm{i} = 5\mathrm{yr}$.

It is also interesting to examine what happens for general total observation times, do errors stop improving within some time t_c before merger? If yes, how does t_c depend on the two timescales t_i and $f_\oplus^{-1}$? I examine this question numerically, substituting (A.1) in (3.49) and (3.50) and now varying both $t_\mathrm{f}/f_\oplus^{-1}$ and $t_\mathrm{i}/f_\oplus^{-1}$. Let us define the critical end-of-observation, t_c, as the time when the marginalized squared parameter error is first within a factor of 2 of its final value. Figure A.2 plots the result for the two parameters. Figure A.2 shows that t_c is determined by $f_\oplus^{-1}$ for large t_i, but becomes t_i-dependent for lower t_i values. In the limit $t_\mathrm{i} \ll f_\oplus^{-1}$, the critical look–back time is independent of $f_\oplus^{-1}$, it becomes a constant fraction of t_i.

Note that, in the limit of an observation extending up to merger, at $t = 0$, the signal

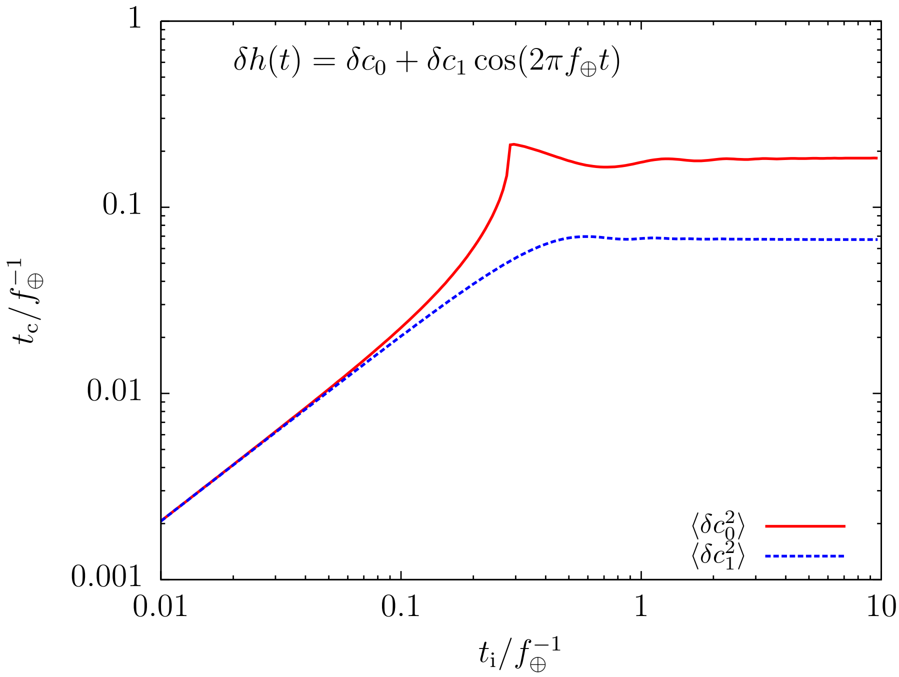

Figure A.2 Critical look–back time, t_c, at which parameter errors stop improving. Here t_c is defined as the time at which marginalized squared errors are within a factor of 2 of their final values for the first time.

becomes $h(0) = c_0 + c_1$ and it has infinite instantaneous signal-to-noise ratio. Therefore, this is the best combination of parameters for which the scaling of errors can follow $(S/N)^{-1}$ all the way to $t = 0$. The worst combination is $c_0 - c_1$, which stops improving before $t = 0$.

For this simple model, the origin of these features can be understood by analyzing the principal errors and the marginalized errors in the error covariance matrix. For this purpose, I present an analytical algebraic solution to this problem. To simplify the equations, let us set the time-scale to $f_\oplus^{-1}/(2\pi)$. In this case the Fisher matrix (3.50) is

$$\Gamma_{ij}(t_\mathrm{f}, t_\mathrm{i}) = \begin{pmatrix} \int_{t_\mathrm{f}}^{t_\mathrm{i}} t^{-2}\mathrm{d}t & \int_{t_\mathrm{f}}^{t_\mathrm{i}} \cos(t) t^{-2}\mathrm{d}t \\ \int_{t_\mathrm{f}}^{t_\mathrm{i}} \cos(t) t^{-2}\mathrm{d}t & \int_{t_\mathrm{f}}^{t_\mathrm{i}} \cos^2(t) t^{-2}\mathrm{d}t \end{pmatrix}. \tag{A.2}$$

The integrals can be evaluated analytically,

$$\Gamma_{ij}(t_\mathrm{f}, t_\mathrm{i}) = \left. \begin{pmatrix} \frac{1}{t} & \frac{\cos(t)}{t} + \mathrm{Si}(t) \\ \frac{\cos(t)}{t} + \mathrm{Si}(t) & \frac{\cos(2t)+1}{2t} + \mathrm{Si}(2t) \end{pmatrix} \right]_{t_\mathrm{i}}^{t_\mathrm{f}}, \tag{A.3}$$

where $\mathrm{Si}(x) = \int_0^x \frac{\sin(x)}{x}\mathrm{d}x$ is the sine integral.

In the next two subsections, I find the limiting behavior of marginalized and principal parameter errors in two different limits: $f_\oplus^{-1} \ll t_\mathrm{i}$ and $t_\mathrm{i} \ll f_\oplus^{-1}$, respectively.

Long Observations ($f_\oplus^{-1} \ll t_\mathrm{i}$)

Here, I assume that the signal has been measured for a very long total time and I concentrate on the effects of changing the end of the observation time, t_f, near merger. Therefore, I take the limit $t_\mathrm{i} \to \infty$, for which

$$\begin{aligned}\Gamma_{ij}(t_\mathrm{f}) &= \begin{pmatrix} \frac{1}{t_\mathrm{f}} & \frac{\cos(t_\mathrm{f})}{t_\mathrm{f}} + \mathrm{Si}(t_\mathrm{f}) \\ \frac{\cos(t_\mathrm{f})}{t_\mathrm{f}} + \mathrm{Si}(t_\mathrm{f}) & \frac{\cos(2t_\mathrm{f})+1}{2t_\mathrm{f}} + \mathrm{Si}(2t_\mathrm{f}) \end{pmatrix} \\ &\quad - \begin{pmatrix} 0 & \pi/2 \\ \pi/2 & \pi/2 \end{pmatrix}. \end{aligned} \tag{A.4}$$

I consider the case of a total observation time which is not negligible compared to a cycle time, $f_\oplus^{-1}$, i.e. $t_\mathrm{f} \ll t_\mathrm{i}$. I next examine two possible cases, $f_\oplus^{-1} \ll t_\mathrm{f} \ll t_\mathrm{i}$ and $t_\mathrm{f} \ll f_\oplus^{-1} \ll t_\mathrm{i}$, separately.

First let us assume that the merger is still far away in time in units of a cycle period ($f_\oplus \ll t_\mathrm{f} \ll t_\mathrm{i}$). I substitute (A.4) in (3.49) and expand $\Gamma^{-1}(t_\mathrm{f})$ into a t_f^{-1} series:

$$(\Gamma^{-1})_{ij} \approx \frac{t_\mathrm{f}}{1 - \frac{\sin(2t_\mathrm{f})}{2t_\mathrm{f}} + \frac{\cos(2t_\mathrm{f})-1}{t_\mathrm{f}^2}} \begin{pmatrix} 1 - \frac{\sin(2t_\mathrm{f})}{2t_\mathrm{f}} & \frac{2\sin(t_\mathrm{f})}{t_\mathrm{f}} \\ \frac{2\sin(t_\mathrm{f})}{t_\mathrm{f}} & 2 \end{pmatrix}. \tag{A.5}$$

Equation (A.5) gives the large t_f behavior of marginalized errors and correlations, which can be compared to Figure A.1 in the appropriate regime, $t_\mathrm{f} > 1\mathrm{yr}$. In this case, to leading order, *all of the squared errors* scale with t_f, which is the scaling of the inverse squared signal-to-noise ratio, $(S/N)^{-2}$, for our noise model.

Next, let us examine the case when the end-of-observation time is close to merger, i.e. $t_\mathrm{f} \ll f_\oplus \ll t_\mathrm{i}$. Now, taking the inverse of the matrix and expanding into a t_f series around $t_\mathrm{f} = 0$ gives

$$(\Gamma^{-1})_{ij} \approx \frac{2}{\pi} \begin{pmatrix} 1 + \frac{2}{3\pi} t_\mathrm{f}^3 & -1 + \frac{t_\mathrm{f}^2}{2\pi^2} \\ -1 + \frac{t_\mathrm{f}^2}{2\pi^2} & 1 + \frac{\pi}{2} t_\mathrm{f} \end{pmatrix}, \tag{A.6}$$

which gives the short timescale behavior of marginalized errors and correlations. The eigenvalues of Γ^{-1} define the squared length of the individual principal axes of the parameter error ellipsoid, in this case

$$\begin{pmatrix} \langle \delta v_0^2 \rangle \\ \langle \delta v_1^2 \rangle \end{pmatrix} \approx \begin{pmatrix} \frac{t_\mathrm{f}}{2} + \frac{3\pi}{16} t_\mathrm{f}^2 \\ \frac{4}{\pi} + \frac{t_\mathrm{f}}{2} + \left(\frac{5\pi}{16} - \frac{2}{\pi}\right) t_\mathrm{f}^2 \end{pmatrix}. \tag{A.7}$$

Note that, in eqs. (A.2)-(A.7), time is measured in units of $f_\oplus^{-1}/(2\pi)$. In full units, the squared marginalized parameter errors (i.e. diagonal elements) of (A.6) become

$$\begin{pmatrix} \langle \delta c_0^2 \rangle \\ \langle \delta c_1^2 \rangle \end{pmatrix} = \begin{pmatrix} \frac{2}{\pi} \left[1 + \left(\frac{t_\mathrm{f}}{\sqrt[3]{3/(16\pi^2)} f_\oplus^{-1}} \right)^3 \right] \\ \frac{2}{\pi} \left[1 + \frac{t_\mathrm{f}}{\frac{1}{\pi^2} f_\oplus^{-1}} \right] \end{pmatrix}. \tag{A.8}$$

For the eigenvalues (A.7), I get

$$\begin{pmatrix} \langle \delta v_0^2 \rangle \\ \langle \delta v_1^2 \rangle \end{pmatrix} = \begin{pmatrix} t_\mathrm{f} / \left(\frac{1}{\pi} f_\oplus^{-1}\right) \\ \frac{4}{\pi} \left[1 + \frac{t_\mathrm{f}}{\frac{4}{\pi^2} f_\oplus^{-1}} \right] \end{pmatrix}. \tag{A.9}$$

Equation (A.8) implies that the evolution of the marginalized squared error on c_0 is very flat for small t_f, when the second term is negligible, i.e. $t_\mathrm{f} \ll \sqrt[3]{\frac{3}{16\pi^2}} f_\oplus^{-1} = 0.267\mathrm{yr}$, then rises steeply ($\propto t_\mathrm{f}^3$). The marginalized squared c_1 error is also constant near merger, for $t_\mathrm{f} \ll \frac{1}{\pi^2} f_\oplus^{-1} \approx 0.1\mathrm{yr}$, and it increases $\propto t_\mathrm{f} \propto (S/N)^{-2}$ for larger t_f. Equation (A.9) shows that one of the principal errors has a very different time-evolution: it has no constant term proportional to t_f^0. Therefore the semi-minor axis of the error ellipsoid can decrease continuously with the signal to noise ratio. On the other hand, the semi-major axis becomes constant for $t_\mathrm{f} \ll \frac{4}{\pi^2} f_\oplus^{-1} = 0.4\mathrm{yr}$. Since the marginalized errors are nontrivial linear combinations of the principal errors, the constant principal error carries over to both marginalized errors and dominates their evolution. All of these findings are in excellent agreement with the numerical results shown in Fig. A.1 for $t_\mathrm{f} \ll 1\mathrm{yr}$ and in Fig. A.3 for $t_\mathrm{i}/f_\oplus^{-1} > 1$.

It is worth emphasizing that, even if the total observation time had been infinite, $t_{\rm i} \to \infty$, the parameters could *not* have been estimated to infinite precision in this model. It is not very surprising if one recalls that in this model I defined errors to be infinitely large at infinitely early times ($\sigma^2(t) \propto t^2$). For stationary noise, the contribution of the last cycle to the resultant RMS estimation error for a total observation of $N_{\rm cyc}$ cycles is $1/\sqrt{N_{\rm cyc}}$. In contrast, *rather than the total number of cycles, the typical error during the last cycle dominates the determination of noise*, for the particular noise model used here.

The main conclusion from this toy model analysis is that errors stop improving close to merger, at $t_{\rm c} \sim 0.1 f_\oplus^{-1}$. It can be extended to more general noise models, with $\sigma^{-2}(t) = t^{-\alpha}$ and $\alpha \neq 2$. Repeating the calculations for larger α values, I find that parameter estimation errors become more and more insensitive to very early times, $t_{\rm f} \ll t \sim t_{\rm i}$, and that marginalized parameter estimation errors cease to improve at some $t_{\rm c}$, which is now an α-dependent fraction of a single cycle time before merger. For $\alpha > 2$, I find that errors increase more abruptly at $t_{\rm f} \gtrsim t_{\rm c}$, which is consistent with the signal-to-noise ratio being a steeper function of time. On the other hand, for lower α values, parameter estimation errors become more and more sensitive to very early times, $t_{\rm f} \ll t \sim t_{\rm i}$. In this case, the marginalized parameter estimation errors are again very slowly changing for $0 \sim t_{\rm f} < t_{\rm c}$, but the approximate time $t_{\rm c}$ at which parameter errors stop decreasing will be primarily determined by $t_{\rm i}$, rather than by the cycle period $f_\oplus^{-1}$. The transition at $t_{\rm f} \gtrsim t_{\rm c}$ is not as abrupt, but extends to several cycles. The $\alpha = 0$ case corresponds to a stationary instantaneous signal-to-noise ratio, with errors scaling slowly as $1/\sqrt{t_{\rm i} - t_{\rm f}}$. This case is irrelevant to LISA inspiral signals, which have $\alpha \sim 2$ to a good approximation for $1\text{day} < t < t_{\rm i}$ in the relevant range of SMBH masses.

Short observations ($t_{\rm i} \ll f_\oplus^{-1}$)

Let us now examine the opposite limiting case, where the start of observation time is already within the final cycle before merger. This is relevant to LISA signals, since the observation time of SMBH inspirals is often below a full year, especially for $(1+z)\,M \geq 4 \times 10^6 \mathrm{M}_\odot$.

I again restrict ourselves to the case with a total observation time that is non-negligible, i.e. $t_{\rm f} \ll t_{\rm i}$. Using time units of $f_\oplus^{-1}/(2\pi)$, expanding (A.3) into a series of both t_i and $t_\mathrm{f}/t_\mathrm{i}$, I get

$$(\Gamma^{-1})_{ij} \approx \frac{120}{t_\mathrm{i}^3(10-t_\mathrm{i}^2)}\left[\begin{pmatrix} 1 & -1 \\ -1 & 1 \end{pmatrix} + \frac{t_\mathrm{f}}{t_\mathrm{i}}\begin{pmatrix} \frac{30-10t_\mathrm{i}^2}{10-t_\mathrm{i}^2} & -\frac{30-5t_\mathrm{i}^2}{10-t_\mathrm{i}^2} \\ -\frac{30-5t_\mathrm{i}^2}{10-t_\mathrm{i}^2} & \frac{30-\frac{5}{3}t_\mathrm{i}^2}{10-t_\mathrm{i}^2} \end{pmatrix}\right] \tag{A.10}$$

Equation (A.10) gives the parameter estimation covariance during the final stages of observation before merger for small total observation times. In this case, the final errors strongly depend on the total observation time. The errors reach their final values when the second term becomes negligible in eq. (A.10). To leading order, this happens at $t_\mathrm{c} \sim t_\mathrm{i}/3$ for both parameters, independently of the cycle time, $f_\oplus^{-1}$. Equation (A.10) approximates well the t_i dependence of t_c shown in Fig. A.2 for $t_\mathrm{i}/f_\oplus^{-1} < 0.2$

A.1.2 Double Frequency Model

Now consider a more elaborate model with five unknowns c_0, s_1, c_1, s_{10}, and c_{10}:

$$\begin{aligned} h(t) &= c_0 + s_1\sin(2\pi f_1 t) + c_1\cos(2\pi f_1 t) \\ &\quad + s_{10}\sin(2\pi f_2 t) + c_{10}\cos(2\pi f_2 t). \end{aligned} \tag{A.11}$$

Here, the signal is comprised of two different characteristic frequencies, f_1 and f_2, for which I assume $f_1 \ll f_2$. Moreover I assume that f_1 and f_2 are fixed and known prior to the measurement, e.g. I take $f_1 \equiv 1\mathrm{yr}^{-1}$ and $f_2 \equiv 10\mathrm{yr}^{-1}$. I again assume an observation in the look–back time interval $t_\mathrm{i} \geq t \geq t_\mathrm{f}$ and take the average instantaneous signal-to-noise ratio to increase as $\sigma(t)^{-2} = t^{-2}$.

Let us substitute in (3.49) and (3.50), and evaluate the expected covariance matrix numerically. Figure A.3 displays the results. As in the previous model, these plots show that all parameter errors decrease with signal to noise ratio until the last cycle and all marginalized errors stop improving beyond some nonzero residual error at late times. Thus, the general trends shown in Fig. A.3 are very much similar to the ones in the previous simple model (Fig. A.1). Again, contrary to the standard $1/\sqrt{N_\mathrm{cyc}}$ expectation, the error during the last cycle dominates the total error of the accumulated signal. Moreover, comparing Figs. A.1 and A.3 shows that the presence of additional

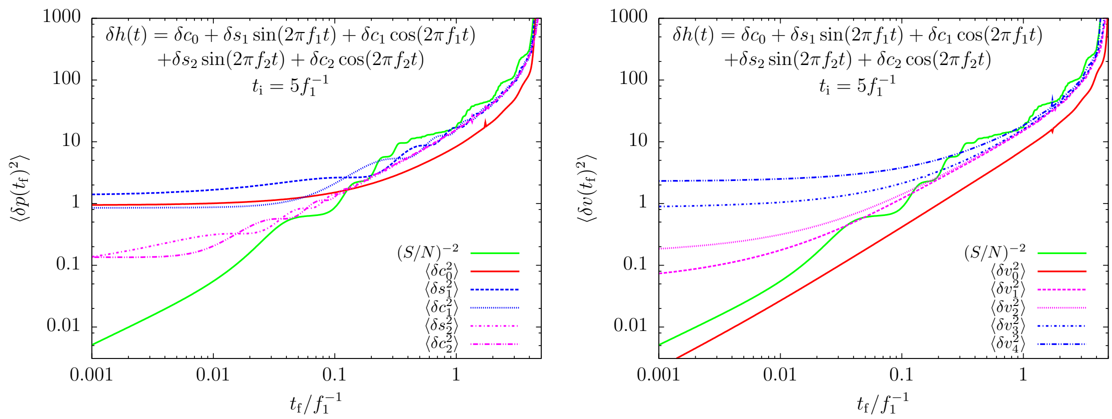

Figure A.3 Marginalized parameter errors (top) and principal errors (bottom) for the double frequency model. The green curve shows the scaling with $(S/N)^{-2}$ for reference on both plots. A total observation time $t_\mathrm{i} = 5\mathrm{yr}$ is assumed. Marginalized errors follow the signal-to-noise ratio for large t_f values, but they stop improving after $t_\mathrm{f} \lesssim 0.1f$, for both frequencies. By comparing the two plots, it is clear that high frequency component errors decouple and that they are determined by two corresponding eigenvalues in the bottom panel.

independent high frequency degrees of freedom practically does not modify the evolution of marginalized parameter errors associated with low frequency components, if $t_\mathrm{i} > f_1^{-1}$. During the final cycle, the error ellipsoid becomes "thin" and the narrow dimension will not be aligned with any of the parameters. As a result, this bad principal error dominates each of the marginalized parameter errors at late times. (Note that the start-of-observation time in Figure A.3 is $t_\mathrm{i} = 5\mathrm{yr}$.)

The critical look–back time, t_c, at which this happens is different for the different frequency components. The top panel in Fig. A.3 shows that $t_{\mathrm{c}i} \sim 0.1 f_i$ approximately for both sets of components (s_1, c_1) and (s_{10}, c_{10}), where f_i denotes the corresponding frequencies $f_1 = 1\mathrm{yr}^{-1}$ and $f_2 = 10\mathrm{yr}^{-1}$, respectively. The bottom panel in Fig. A.3 shows that the principal errors separate in three groups. There is one best eigenvector that improves continuously until the end, two that stop improving near $t_{\mathrm{c}1} \sim 0.1 f_1$ and two that stop improving at $t_{\mathrm{c}2} \sim 0.1 f_2$. The high frequency parameters (s_{10}, c_{10}) totally decouple from the two worst principal components, (v_0, v_1), and, as a result, decouple from the low frequency parameters (c_0, s_1, c_1) which are primarily determined by (v_0, v_1).

As for our previous model in § A.1.1, the critical look–back time is generally different for different t_i values. The bottom panel in Figure A.4 shows the time t_c at which the squared errors first double, as a function of t_i/f_1^{-1}, as in Fig. A.2. Fig. A.4 justifies the

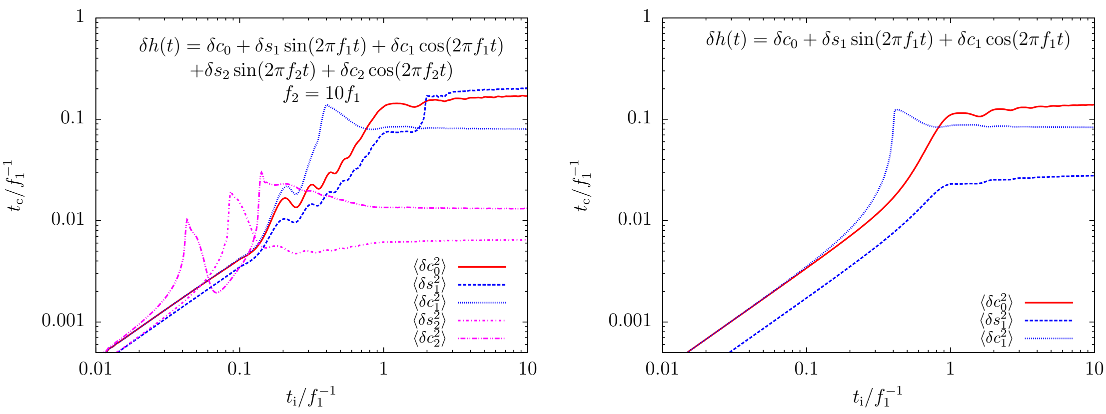

Figure A.4 Critical look–back time, t_c (as in Fig. A.2), at which marginalized parameter errors stop improving. *Top:* Only (c_0, s_1, c_1) are allowed to vary, using the prior $(s_{10}, c_{10}) \equiv (0, 0)$. *Bottom:* All 5 parameters $(c_0, s_1, c_1, s_{10}, c_{10})$ are determined from the observation. For $t_{\rm i} \gtrsim f_1^{-1}$, estimations of low frequency parameters (c_0, s_1, c_1) stop improving at $t_c \sim 0.1 f_1^{-1}$, while improvement for high frequency parameters occurs all the way to $t_c \sim 0.1 f_2^{-1}$.

rule-of-thumb scaling $t_{ci} \sim 0.1 f_i$ if the observation time is at least one cycle period, f_1^{-1}.

The central question for the present analysis is how sensitive is the time evolution of low frequency modulation errors to the presence of high frequency components. I can examine this question by computing the critical look–back time, t_c, when the high frequency terms are totally neglected. The top panel in Fig. A.2 shows that, if one limits the parameters to (c_0, s_1, c_1), and the total observation time is not smaller than the long-period cycle time, $\sim f_1^{-1}$, the resulting t_c value for parameters c_0 and c_1 is unchanged at the few percent level. However, if the high frequency components are introduced, the s_1 error evolves differently since it asymptotes already at much larger t_c values ($\sim 0.1 f_1^{-1}$ rather than $\sim 0.03 f_{-1}$). The reason is that, for small t, with a noise level decreasing quickly, the corresponding function $s_1 \sin(2\pi f_1 t) \approx 2\pi f_1 s_1 t$ is linearly independent of, and thus uncorrelated with, the functions c_0 and $c_1 \cos(2\pi f_1 t)$ which are both constant to first order. Hence, if there are no more unknowns than (c_0, s_1, c_1), then c_0 and c_1 are correlated while s_1 is decoupled and can be determined independently of the other parameters. However, if I add any parameters which are *not* constant for $t \ll f_1^{-1}$, then s_1 becomes correlated with those. This is exactly what happens in the bottom panel of Fig. A.2, when considering the high frequency modulations: the estimation on s_1 becomes limited for $t \lesssim t_{c1} \sim 0.1 f_1^{-1}$ due to the correlations with s_{10} and c_{10}. Quite similarly, if one introduces any other low-frequency function that is not constant to first order, like $s_2 \sin(4\pi f_1 t)$, then the correlations with this parameter will limit the improvement of estimation errors for s_1 at $t_{\rm c} \sim 0.1 f_1$, even when neglecting the high frequency components. As I shall see, this is the case for LISA: there are generally more than one sin and cos low-frequency modes. In this case, the evolution of estimation errors for low frequency parameters can be obtained with the high frequency modes (like s_{10} and c_{10}) priored out. This justifies our simple intuition: once the signal is decomposed into different time-scale components, the parameter estimation problem becomes separable and the evolution of parameter errors corresponding to different such time-scales can be estimated independently from each other.

Rather than going through an analytical derivation as in § A.1.1, I answer one remaining question here: what combination of the original parameters $(c_0, s_1, c_1, s_{10}, c_{10})$ corresponds to the best principal component, v_0, which can be determined extremely accurately at late times, $t_{\rm f} \to 0$? At $t = 0$, the noise drops to zero. Therefore, the quantity I can measure using the $t = 0$ information is simply $h(t = 0)$. Looking back at eq. (A.11), this is $c_0 + c_1 + c_2$. It will be interesting to look for similar "best determined combinations" of physical parameters for the case of the LISA's realistic signals.

A.1.3 Four data-stream models

For our final toy model, I insert additional features of a realistic LISA data-stream. I consider five low frequency unknowns, c_0, s_1, c_1,s_2, c_2, and a high frequency carrier signal with additional unknowns s_{10}, and c_{10}. Moreover I consider the simultaneous measurement of four data-streams. The signal is

$$\begin{aligned} h(t) \quad = \quad & c_0 + s_1 \sin(2\pi f_1 t + \varphi_i^{s_1}) + c_1 \cos(2\pi f_1 t + \varphi_i^{c_1}) \\ & + s_2 \sin(2\pi f_1 t + \varphi_i^{s_2}) + c_2 \cos(2\pi f_1 t + \varphi_i^{c_2}) \\ & + s_{10} \sin(2\pi f_2 t) + c_{10} \cos(2\pi f_2 t), \end{aligned} \tag{A.12}$$

where $\varphi_i^{c_1,s_1,c_2,s_2}$ $(i = 1 \ldots 4)$ are fixed at a priori randomly chosen numbers defining the relative phases of the various modes which are being simultaneously measured. I compute independent Fisher matrices for each four set of $\varphi_i^{c_1,s_1,c_2,s_2}$. I assume that $f_1 \ll f_2$ and that f_1 and f_2 are fixed and known prior to the measurement. I choose $f_2 = 10 f_1$ and find the evolution of marginalized errors and principal errors in two limits:

(i) neglecting cross-correlations with the high frequency parameters by assuming a prior $\delta s_{10} = \delta c_{10} = 0$, and

(ii) accounting for these high frequency parameters.

I again assume an observation in the look–back time interval $t_\mathrm{i} \geq t \geq t_\mathrm{f}$ and take the average instantaneous signal-to-noise ratio to increase as $\sigma(t)^{-2} = t^{-2}$.

The results for these models are shown in Figure A.5. Th marginalized errors (top) and principal errors (bottom) are shown for both cases (i) and (ii) above. The figures show that, in agreement with our previous model, uncertainties on the low frequency parameters are not affected by the high frequency parameters, except during the final 0.1 cycle time of the high frequency component, $0.1 f_2^{-1}$. The figures also show that the four principal components of the error ellipsoid improve quickly at late times.

Marginalized parameter errors improve quickly if they have negligible projection on the bad directions of the error ellipsoid. As a result, our expectation is that errors will typically not stop improving abruptly, but that there will be a shallower evolution in the final two weeks. In the worst case for a given parameter, if it is aligned with the bad ellipsoid principal component, it will stop improving near merger. In the best case, if the parameter is orthogonal to the bad ellipsoid principal component, it will improve quickly throughout the final days of inspiral. Therefore, I understand that the distribution of errors broadens for $t_\mathrm{f} \ll 0.1 f_1^{-1}$.

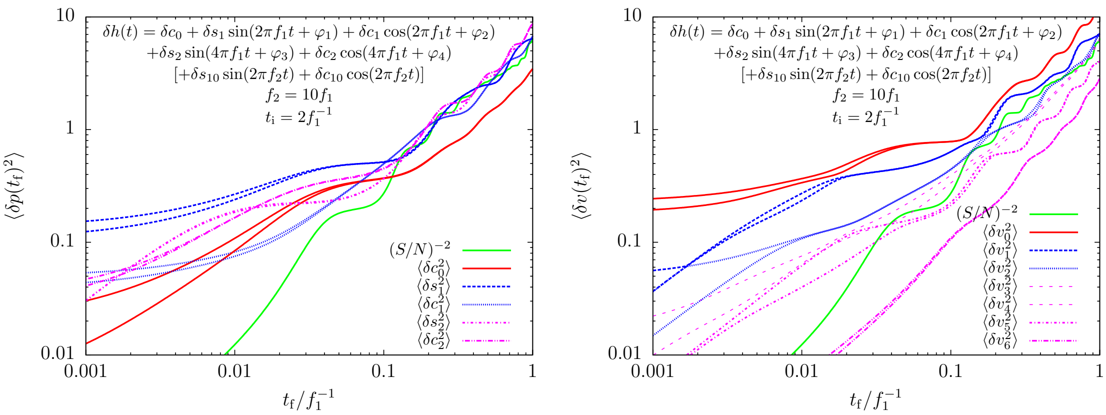

Figure A.5 Marginalized parameter errors *(top)* and principal errors *(bottom)* for the four data-stream model. Pairs of curves with the same line style show results for cases with five and seven parameters. The extra two parameters correspond to high frequency (f_2) components, which affect errors on the other parameters through correlations only slightly (factor of $\lesssim 2$) if $t_\mathrm{f} \lesssim 0.1 f_2^{-1}$. The green curve shows the scaling with inverse squared signal-to-noise ratio, $(S/N)^{-2}$, for reference on both plots. A total observation time $t_\mathrm{i} = 2\mathrm{yr}$ is assumed. Marginalized errors follow the signal-to-noise ratio for large t_f values. Four principal errors scale with the signal-to-noise ratio near merger.

A.1.4 Best Determined Parameters

In the previous section, I have shown that, if the noise decreases quickly like t^2 near merger (at $t = 0$), the best-determined parameters are the eigenvectors of the error covariance matrix that improve with $(S/N)^{-1}$. Near merger, these are the independent detector outputs at $t = 0$. In the case of LISA inspirals, the observation only extends down to ISCO. In this case, the best determined combination of physical parameters p_1 at ISCO are the real and imaginary parts of $h_1^{\mathrm{I,II}}(p_1)$. To prove this, I have to show that these are uncorrelated and decrease with $(S/N)^{-1}$. The functions $h^{\mathrm{I}}(t)$ and $h^{\mathrm{II}}(t)$ are uncorrelated by construction, since they correspond to the two independent Michelson detector outputs (see § 3.2.2 and Cutler, 1998). The real and imaginary parts of one of the detectors, $\mathfrak{Re}\, h_1^{\mathrm{I}}(t)$ and $\mathfrak{Im} h_1^{\mathrm{I}}$, are uncorrelated since they are the coefficients of the high frequency carrier, $\sin\phi_{GW}$ and $\cos\phi_{GW}$, for which correlation over one ϕ_{GW} cycle (during which the detector noise is approximately constant) is zero. Another way to see this is to focus on the real part in the definition of the Fisher matrix (3.57), which is expressed as the integral of $\mathfrak{Re}\,[\overline{\partial_a h_1^{\mathrm{I,II}}(t)}\partial_b h_1^{\mathrm{I,II}}(t)]$. The term in brackets is purely imaginary for the cross correlation of $\mathfrak{Re}\, h_1^{\mathrm{I}}(t)$ and $\mathfrak{Im} h_1^{\mathrm{I}}$, hence the real part is always zero. Therefore, the correlation matrix for $\mathfrak{Re}\, h_1^{\mathrm{I,II}}, \mathfrak{Im} h_1^{\mathrm{I,II}}$ is diagonal. For diagonal terms, the derivatives are 1 and the integrals become simply $\int \sigma^{-2} \mathrm{d}t$, which is exactly $(S/N)^2$. The RMS estimation uncertainty of $\mathfrak{Re}\, h_1^{\mathrm{I,II}}(p_1)$ and $\mathfrak{Im} h_1^{\mathrm{I,II}}(p_1)$ follows the $(S/N)^{-1}$ all the way down to ISCO. These best combinations are $d_{\mathrm{L}}^{-1}(1+\cos^2\theta_{NL})F_+^{I,II}(\Omega)$ and $d_{\mathrm{L}}^{-1}\cos\theta_{NL}F_\times^{I,II}(\Omega)$.

The evolution of an arbitrary combination of angles will be determined by the projection of this combination on the covariance matrix eigenvectors. A linear combination of good eigenvectors leads to similarly quick improvement of errors with $(S/N)^{-1}$. However, as soon as there is a nonzero projection on the fifth eigenvector, the estimation uncertainty will stop improving at $\sim 0.1 T_{\mathrm{cycle}}$ which, for the highest $j = 4$ harmonic, is between 1–2 weeks.

A.2 Angular variables

Here I define the relative angles θ_{NL} and ϕ_{NL}, using the polar angles (θ_N, ϕ_N) and (θ_L, ϕ_L) and the corresponding unit vectors $\hat{\mathbf{N}}$ and $\hat{\mathbf{L}}$.

Let us write a rotation around $\hat{\mathbf{z}}$ and $\hat{\mathbf{y}}$ as $O_z(\phi)$ and $O_y(\theta)$, respectively. Then,

$\hat{\mathbf{z}} = O_y(-\theta_N)O_z(-\phi_N)\hat{\mathbf{N}}$ and I define

$$\begin{pmatrix} \sin(\theta_{NL})\cos(\phi_{NL}) \\ \sin(\theta_{NL})\cos(\phi_{NL}) \\ \cos(\theta_{NL}) \end{pmatrix} \equiv O_y(-\theta_N)O_z(-\phi_N)\hat{\mathbf{L}}. \tag{A.13}$$

This uniquely defines θ_{NL} and ϕ_{NL}, which correspond to the relative latitude and longitude, respectively. More explicitly, I get

$$\begin{aligned} \theta_{NL} &= \arccos(\hat{\mathbf{N}}\cdot\hat{\mathbf{L}}) = \qquad (A.14)\\ &= \arccos\left[\sin\theta_N\sin\theta_L\cos(\phi_L-\phi_N)+\cos\theta_N\cos\theta_L\right], \end{aligned}$$

$$\phi_{NL} = \begin{cases} 2\pi-\phi_0 & \text{if } (\phi_L-\phi_N)/\pi \in [-1,0]\bigcup[1,2] \\ \phi_0 & \text{otherwise} \end{cases}, \tag{A.15}$$

where

$$\phi_0 = \arccos\left(\frac{\cos\theta_N\sin\theta_L\cos(\phi_L-\phi_N)-\sin\theta_N\cos\theta_L}{\sin\theta_{\rm NL}}\right). \tag{A.16}$$

Appendix B

Parabolic Encounter Event Rates

B.1 Approximate Analytical Formulae

The integrals given in Eq. (4.19) can be carried out analytically as a Taylor-expansion with respect to the small quantities $\kappa_{\rm BH} = m_{\rm min}/m_{\rm max}$ and $\kappa_{\rm NS} = m_{\rm NS}/m_{\rm max}$. The PE event rate is calculated in three parts

$$\nu_1^{\rm II} = \nu_{1,\rm BH-BH}^{II} + \nu_{1,\rm BH-NS}^{II} + \nu_{1,\rm NS-NS}^{\rm II}, \tag{B.1}$$

where $\nu_{1,\rm BH-BH}^{II}$, $\nu_{1,\rm BH-NS}^{II}$, and $\nu_{1,\rm NS-NS}^{II}$ are the event rates of BH-BH, BH-NS, and NS-NS encounters. Substituting the mass dependence in Eq. (4.19) I get,

$$\nu_1^{\rm II}(m_1, m_2) = \frac{\mathrm{G}^{4/3}}{(4\pi)^{2/3}} \frac{N_{\rm CO}^2}{R_{\rm gc}^3 v_{\rm vir}} \frac{(m_1+m_2)^{4/3} m_>^{3/2}}{(m_1^{-1}+m_2^{-1})^{1/2}} f_{100}^{-2/3}, \tag{B.2}$$

$$\nu_2^{\rm II}(m_1, m_2) = \frac{2^{1/3}\mathrm{G}^{2/3}}{3\pi^{4/3}} \frac{N_{\rm CO}^2 v_{\rm vir}}{R_{\rm gc}^3} (m_1+m_2)^{4/3} (m_1^{-1}+m_2^{-1})^{1/2} m_>^{3/2} f_{100}^{-4/3}. \tag{B.3}$$

Next I present ready-to-use formulas for calculating the detection rates of PEs. Assuming a constant density of GCs, no cosmological and no general relativistic corrections, the detection rate per logarithmic frequency bin becomes

$$\frac{\mathrm{d}\nu^{\rm tot}}{\mathrm{d}\ln(f_0)} = k \frac{(2\mathrm{GM}_\odot)^{19/3}}{\mathrm{c}^{12}} n^{\rm gc} N_{\rm CO}^2 R_{\rm gc}^{-3} v_{\rm vir}^{-1} f_0^{4/3} \left(\frac{W(f_0)}{S/N}\right)^3 K(f_0, \lambda) \tag{B.4}$$

where S/N is the minimum signal-to-noise ratio (which is set equal to 5 in our numerical results above), $k \equiv 85^{3/2}2^{1/3}\pi^{7/3}/6144 = 2.323$ is a constant coefficient, $v_{\rm vir}$ is the virial velocity (4.9), $n^{\rm gc}$ is the average GC density in the universe, $R_{\rm gc}$ is the typical radius of the GC, $N_{\rm CO}$ is the number of COs in the GC, $K(f_0,\lambda)$ and $W(f_0)$ are dimensionless terms, $K(f_0,\lambda)$ depending on the CO mass distribution, $g_{\rm CO}$, and $W(f_0)$ on the normalized GW energy spectrum $F(f/f_0)$ Eq. (4.5), and the detector spectral noise density, $S_n(f)$:

$$K(f_0,\lambda) = \int\int_{f_0\leq f_{0,\max}[\mathrm{M}_\odot(x_1+x_2),\lambda]} \mathrm{d}x_1\mathrm{d}x_2\; g_{\rm CO}(x_1)g_{\rm CO}(x_2)\frac{(x_1x_2)^{7/2}x_>^{3/2}}{(x_1+x_2)^{1/6}}, \tag{B.5}$$

$$W(f_0) = \sqrt{\frac{4}{5}\int_{f_{\min}}^{f_{\max}} \frac{1}{f^2}\frac{F(f/f_0)}{S_n(f)^2}\,\mathrm{d}f}. \tag{B.6}$$

In terms of f_0, $K(f_0,\lambda)$ is constant for $f_0 \leq f_{0,max}(2m_{\min},\lambda)$, decreases monotonically for larger f_0 and attains 0 for $f_0 \geq f_{0,\max}(2m_{\max},\lambda)$ (see Eq. [4.33] for the definition of $f_{0,\max}(M,\lambda)$, and $m_{\min}$ and $m_{\max}$ are the minimum and maximum masses of the COs, respectively). In Eq. (B.5), the integration variables x_1 and x_2 are the dimensionless masses of the COs, for which $m_{\min}/\mathrm{M}_\odot \leq x_{1,2} \leq m_{\max}/\mathrm{M}_\odot$. For core collapsed clusters $\mathrm{M}_\odot$ has to be changed to $m_{\rm core}$, the typical mass of individual components in the core, $R_{\rm gc}$ has to be changed to $R_{\rm core}$, and $v_{\rm vir}$ to $v_{\rm core}$. These values should be set consistently with the core velocity dispersion and core radius which are input parameters for a globular cluster model. For given m components, the velocity dispersion is then $v_m = (m/m_{\rm core})^{-1/2}v_{\rm core}$ and maximum radius from the cluster center is $R_m = (m/m_{\rm core})^{-1/2}R_{\rm core}$.

The total detection rate of parabolic encounters (again assuming a constant density of GCs and no cosmological and general relativistic corrections) is

$$\nu^{\rm tot} = k\frac{(2\mathrm{G}m_{\rm core})^{19/3}}{\mathrm{c}^{12}}(S/N)^{-3}n^{\rm gc}N_{\rm CO}^2R_{\rm core}^{-3}v_{\rm core}^{-1}\int_{f_{\min}/10}^{f_{0,\max}(2M_{\max},\lambda)} \mathrm{d}f_0\, f_0^{1/3}W(f_0)^3K(f_0,\lambda). \tag{B.7}$$

Bibliography

Abbott, B., et al. 2005a, Phys. Rev. Lett., 94, 181103

—. 2005b, Phys. Rev., D72, 042002

—. 2005c, Phys. Rev., D72, 082002

—. 2005d, Phys. Rev., D72, 062001

Abbott, T. L. S. C. 2004, NUCL.INSTRUM.METH.A, 517, 154

Acernese, F., et al. 2005, Class. Quant. Grav., 22, S869

Adelberger, K. L., & Steidel, C. C. 2005, Astrophys. J., 627, L1

Ando, M. 2005, Class. Quant. Grav., 22, S881

Anninos, P., Hobill, D., Seidel, E., Smarr, L., & Suen, W.-M. 1993, Physical Review Letters, 71, 2851

Armitage, P. J., & Natarajan, P. 2002, Astrophys. J. Lett., 567, L9

Armitage, P. J., & Natarajan, P. 2005, Astrophys. J., 634, 921

Arun, K. G. 2006, Phys. Rev., D74, 024025

Atakan Gurkan, M., Freitag, M., & Rasio, F. A. 2004, Astrophys. J., 604, 632

Baker, J. G., Centrella, J., Choi, D.-I., Koppitz, M., & van Meter, J. 2006, Phys. Rev., D73, 104002

Barack, L., & Cutler, C. 2004a, Phys. Rev., D70, 122002

—. 2004b, Phys. Rev., D69, 082005

Barnes, J. E., & Hernquist, L. E. 1992, Ann. Rev. Astron. Astrophys., 30, 705

Begelman, M. C., Blandford, R. D., & Rees, M. J. 1980, Nature, 287, 307

Belczynski, K., Sadowski, A., Rasio, F. A., & Bulik, T. 2006, Astrophys. J., 650, 303

Benacquista, M. J., DeGoes, J., & Lunder, D. 2004, Class. Quant. Grav., 21, S509

Berti, E., Buonanno, A., & Will, C. M. 2005a, Phys. Rev., D71, 084025

—. 2005b, Phys. Rev., D71, 084025

—. 2005c, Class. Quant. Grav., 22, S943

Berti, E., Cardoso, V., & Will, C. M. 2006, Phys. Rev., D73, 064030

Binney, J., & Tremaine, S. 1987, Galactic dynamics (Princeton, NJ, Princeton University Press, 1987, 747 p.)

Blanchet, L., Damour, T., Esposito-Farese, G., & Iyer, B. R. 2005, Phys. Rev., D71, 124004

Blanchet, L., Damour, T., Iyer, B. R., Will, C. M., & Wiseman, A. G. 1995, Phys. Rev. Lett., 74, 3515

Blanchet, L., & Schafer, G. 1989, Mon. Not. Roy. Astron. Soc., 239, 845

Blecha, L., et al. 2006, Astrophys. J., 642, 427

Cardoso, V., & Lemos, J. P. S. 2003, Phys. Rev., D67, 084005

Casares, J. 2006, in The Many Scales in the Universe: JENAM 2004 Astrophysics Reviews, ed. J. C. Del Toro Iniesta, E. J. Alfaro, J. G. Gorgas, E. Salvador-Sole, & H. Butcher, 145–+

Cen, R., & Ostriker, J. P. 2000, Astrophys. J., 538, 83

Chandar, R., Whitmore, B., & Lee, M. G. 2004, Astrophys. J., 611, 220

Cornish, N. J., & Crowder, J. 2005, Phys. Rev., D72, 043005

Cornish, N. J., & Rubbo, L. J. 2003, Phys. Rev., D67, 022001

Croom, S. M., et al. 2005, Mon. Not. Roy. Astron. Soc., 356, 415

Crowder, J., & Cornish, N. J. 2005, Phys. Rev., D72, 083005

Cutler, C. 1998, Phys. Rev., D57, 7089

Cutler, C., & Flanagan, E. E. 1994, Phys. Rev., D49, 2658

Cutler, C., Kennefick, D., & Poisson, E. 1994, Phys. Rev., D50, 3816

Cutler, C., & Thorne, K. S. 2002, ArXiv General Relativity and Quantum Cosmology e-prints

Dalal, N., Holz, D. E., Chen, X., & Frieman, J. A. 2003, Astrophys. J. Lett., 585, L11

Danzmann, K., & Rüdiger, A. 2003, Classical and Quantum Gravity, 20, 1

Davis, M., Ruffini, R., Press, W. H., & Price, R. H. 1971, Phys. Rev. Lett., 27, 1466

D'eath, P. D., & Payne, P. N. 1992, Phys. Rev. D, 46, 694

DeSalvo, R. 2004, Class. Quant. Grav., 21, S1145

Djorgovski, S., & Meylan, G. 1994, Astron. J., 108, 1292

Dotti, M., Salvaterra, R., Sesana, A., Colpi, M., & Haardt, F. 2006, Mon. Not. Roy. Astron. Soc., 372, 869

Dreyer, O., et al. 2004, Class. Quant. Grav., 21, 787

Dymnikova, I. G., Popov, A. K., & Zentsova, A. S. 1982, Astrophys. and Space Sci., 85, 231

Eisenstein, D. J. 1997, ArXiv Astrophysics e-prints

Escala, A., Larson, R. B., Coppi, P. S., & Mardones, D. 2004, Astrophys. J., 607, 765

Fang, T., & Canizares, C. R. 2000, Astrophys. J., 539, 532

Farouki, R. T., & Salpeter, E. E. 1982, Astrophys. J., 253, 512

Finn, L. S. 1992, Phys. Rev., D46, 5236

Flanagan, É. É., & Hughes, S. A. 1998, Phys. Rev. D, 57, 4566

Freitag, M. 2003, Astrophys. J., 583, L21

Freitag, M., Gurkan, M. A., & Rasio, F. A. 2006, Mon. Not. Roy. Astron. Soc., 368, 141

Fryer, C. L., & Kalogera, V. 2001, Astrophys. J., 554, 548

Gair, J. R., Kennefick, D. J., & Larson, S. L. 2005, Phys. Rev., D72, 084009

—. 2006, Astrophys. J., 639, 999

Gair, J. R., et al. 2004, Class. Quant. Grav., 21, S1595

Gebhardt, K., Rich, R. M., & Ho, L. C. 2005, Astrophys. J., 634, 1093

Goudfrooij, P., et al. 2003, Mon. Not. Roy. Astron. Soc., 343, 665

Gould, A., & Rix, H.-W. 2000, Astrophys. J. Lett., 532, L29

Greene, J. E., & Ho, L. C. 2004, Astrophys. J., 610, 722

Grote, H., et al. 2005, Class. Quant. Grav., 22, S193

Haiman, Z., & Loeb, A. 1998, Astrophys. J., 503, 505

Haiman, Z., & Menou, K. 2000, Astrophys. J., 531, 42

Hamana, T., Kayo, I., Yoshida, N., Suto, Y., & Jing, Y. P. 2003, Mon. Not. Roy. Astron. Soc., 343, 1312

Heggie, D. C., Trenti, M., & Hut, P. 2006, Mon. Not. Roy. Astron. Soc., 368, 677

Hennawi, J. F., et al. 2006, Astron. J., 131, 1

Hills, J. G., & Day, C. A. 1976, Astrophys. Lett., 17, 87

Hils, D., Bender, P. L., & Webbink, R. F. 1990, Astrophys. J., 360, 75

Holz, D. E., & Hughes, S. A. 2005, Astrophys. J., 629, 15

Holz, D. E., & Linder, E. V. 2005, Astrophys. J., 631, 678

Hopkins, P. F., et al. 2006, Astrophys. J. Suppl., 163, 1

Hopman, C., & Alexander, T. 2005, Astrophys. J., 629, 362

Hu, W., & Haiman, Z. 2003, Phys. Rev., D68, 063004

Hughes, S. A. 2002a, Mon. Not. Roy. Astron. Soc., 331, 805

—. 2002b, Mon. Not. Roy. Astron. Soc., 331, 805

Hughes, S. A., Marka, S., Bender, P. L., & Hogan, C. J. 2001, ArXiv Astrophysics e-prints

Hughes, S. A., & Menou, K. 2005, Astrophys. J., 623, 689

Ioka, K., Chiba, T., Tanaka, T., & Nakamura, T. 1998, Phys. Rev., D58, 063003

Islam, R. R., Taylor, J. E., & Silk, J. 2004, Mon. Not. Roy. Astron. Soc., 354, 629

Jaranowski, P., Krolak, A., Kokkotas, K. D., & Tsegas, G. 1996, Class. Quant. Grav., 13, 1279

Kalogera, V., et al. 2004, Astrophys. J., 601, L179

Kaspi, S., et al. 2000, Astrophys. J., 533, 631

Kauffmann, G., & Haehnelt, M. 2000, Mon. Not. Roy. Astron. Soc., 311, 576

—. 2002, Mon. Not. Roy. Astron. Soc., 332, 529

Khanna, G., et al. 1999, Phys. Rev. Lett., 83, 3581

Kocsis, B., Frei, Z., Haiman, Z., & Menou, K. 2006, Astrophys. J., 637, 27

Kocsis, B., & Gáspár, M. E. 2004, expectations on the Gravitational-Wave Signals Associated with Cosmic Bremsstrahlung Events, LIGO Note

Kocsis, B., Gáspár, M. E., & Márka, S. 2006, Astrophys. J., 648, 411

Kocsis, B., Haiman, Z., & Frei, Z. 2005, Astrophys. J., 623, 632

Kocsis, B., Haiman, Z., Menou, K., & Frei, Z. 2007, ArXiv Astrophysics e-prints

Kocsis, B., Haiman, Z., Menou, K., & Frei, Z. 2007, in preparation

Kollmeier, J. A., et al. 2006, Astrophys. J., 648, 128

Kovacs, S. J., & Thorne, K. S. 1978, Astrophys. J., 224, 62

Kroupa, P., & Weidner, C. 2003, Astrophys. J., 598, 1076

Lang, R. N., & Hughes, S. A. 2006, Phys. Rev., D74, 122001

Lee, M. H. 1993, Astrophys. J., 418, 147

Lidz, A., Hopkins, P. F., Cox, T. J., Hernquist, L., & Robertson, B. 2006, Astrophys. J., 641, 41

Lotz, J. M., Miller, B. W., & Ferguson, H. C. 2004, Astrophys. J., 613, 262

Madau, P. 1995, Astrophys. J., 441, 18

Madau, P., Haardt, F., & Rees, M. J. 1999, Astrophys. J., 514, 648

Martel, K. 2004, Phys. Rev., D69, 044025

Menou, K. 2003, Classical and Quantum Gravity, 20, 37

Menou, K., Haiman, Z., & Narayanan, V. K. 2001, Astrophys. J., 558, 535

Meylan, G. 1987, Astron. and Astrophys., 184, 144

Micic, M., Holley-Bockelmann, K., Sigurdsson, S., & Abel, T. 2007, ArXiv Astrophysics e-prints

Mikoczi, B., Vasuth, M., & Gergely, L. A. 2005, Phys. Rev., D71, 124043

Miller, M. C. 2002, Astrophys. J., 581, 438

—. 2004, Astrophys. J., 618, 426

Miller, M. C., & Colbert, E. J. M. 2004, Int. J. Mod. Phys., D13, 1

Milosavljevic, M., & Phinney, E. S. 2005, Astrophys. J., 622, L93

Mino, Y., Shibata, M., & Tanaka, T. 1996, Phys. Rev. D, 53, 622

Misner, C. W., Thorne, K. S., & Wheeler, J. A. 1973, Gravitation (San Francisco: W.H. Freeman and Co., 1973)

Moore, T. A., & Hellings, R. W. 2002, Phys. Rev., D65, 062001

Moreschi, O. M. 1999, Phys. Rev., D59, 084018

Nakar, E., Gal-Yam, A., & Fox, D. B. 2006, Astrophys. J., 650, 281

Nelemans, G., Yungelson, L. R., & Portegies Zwart, S. F. 2001, Astron. Astrophys., 375, 890

O'Leary, R. M., Rasio, F. A., Fregeau, J. M., Ivanova, N., & O'Shaughnessy, R. 2006, Astrophys. J., 637, 937

Papaloizou, J. C. B., Nelson, R. P., & Masset, F. 2001, Astron. and Astrophys., 366, 263

Perna, R., & Loeb, A. 1998, Astrophys. J. Lett., 503, L135+

Peters, P. C. 1964, Physical Review, 136, 1224

Poisson, E., & Will, C. M. 1995, Phys. Rev., D52, 848

Portegies Zwart, S. F., & McMillan, S. L. W. 2000, Astrophys. J. Lett., 528, L17

Postnov, K. A., & Prokhorov, M. E. 2001, Astronomy Reports, 45, 899

Price, R. H., & Pullin, J. 1994, Phys. Rev. Lett., 72, 3297

Prince, T. A., Tinto, M., Larson, S. L., & Armstrong, J. W. 2002, Phys. Rev., D66, 122002

Pryor, C., & Meylan, G. 1993, in Astronomical Society of the Pacific Conference Series, Vol. 50, Structure and Dynamics of Globular Clusters, ed. S. G. Djorgovski & G. Meylan, 357–+

Ptak, A., & Colbert, E. 2004, Astrophys. J., 606, 291

Rauch, K. P., & Tremaine, S. 1996, New Astron., 1, 149

Richards, G. T., et al. 2005, Mon. Not. Roy. Astron. Soc., 360, 825

Sasaki, M., & Nakamura, T. 1982, Prog. Theor. Phys., 67, 1788

Saslaw, W. C. 1985, Gravitational physics of stellar and galactic systems (Cambridge, Cambridge University Press, 1985, 506 p.)

Scalo, J. M. 1986, Fund. Cosmic Phys., 11, 1

Schutz, B. F. 1986, Nature, 323, 310

Sesana, A., Haardt, F., Madau, P., & Volonteri, M. 2004, Astrophys. J., 611, 623

Sesana, A., Volonteri, M., & Haardt, F. 2007, Mon. Not. Roy. Astron. Soc., 377, 1711

Seto, N., Kawamura, S., & Nakamura, T. 2001, Phys. Rev. Lett., 87, 221103

Sigurdsson, S., & Hernquist, L. 1993, Nature, 364, 423

Sigurdsson, S., & Phinney, E. S. 1995, Astrophys. J. Suppl., 99, 609

Sigurdsson, S., & Rees, M. J. 1997, Mon. Not. Roy. Astron. Soc., 318

Small, T. A., & Blandford, R. D. 1992, Mon. Not. Roy. Astron. Soc., 259, 725

Smith, R. E., et al. 2003, Mon. Not. Roy. Astron. Soc., 341, 1311

Spergel, D. N., et al. 2003, Astrophys. J. Suppl., 148, 175

Sperhake, U., Kelly, B., Laguna, P., Smith, K. L., & Schnetter, E. 2005, Phys. Rev., D71, 124042

Spitzer, L. J. 1969, Astrophys. J. Lett., 158, L139+

Tegmark, M., et al. 2004a, Phys. Rev., D69, 103501

—. 2004b, Phys. Rev., D69, 103501

Thompson, T. A., Quataert, E., & Murray, N. 2005, Astrophys. J., 630, 167

Thorne, K. S. 1987, Three Hundred Years of Gravitation (Cambridge University Press), 330–458, ed. Hawking, S.W. and Israel, W.

Tully, R. B. 1988, Astron. J., 96, 73

Turner, M. 1977, Astrophys. J., 216, 610

Tyson, J. A. 2002, Proc. SPIE Int. Soc. Opt. Eng., 4836, 10

van den Bergh, S. 2006, Astron. J., 131, 304

Van Den Broeck, C., & Sengupta, A. S. 2007a, Classical and Quantum Gravity, 24, 1089

—. 2007b, Classical and Quantum Gravity, 24, 155

Vecchio, A. 2004, Phys. Rev., D70, 042001

Vestergaard, M. 2004, Astrophys. J., 601, 676

Volonteri, M., Madau, P., Quataert, E., & Rees, M. J. 2005, Astrophys. J., 620, 69

Wang, S., Khoury, J., Haiman, Z., & May, M. 2004, Phys. Rev., D70, 123008

Wang, Y., Holz, D. E., & Munshi, D. 2002, Astrophys. J., 572, L15

Watters, W. A., Joshi, K. J., & Rasio, F. A. 2000, Astrophys. J., 539, 331

White, M. J., & Hu, W. 2000, Astrophys. J., 537, 1

Will, C. M. 2004, Astrophys. J., 611, 1080

Woo, J.-H., & Urry, C. M. 2002, Astrophys. J., 579, 530

Wyithe, J. S. B., & Loeb, A. 2002, Astrophys. J., 577, 615

Wyithe, J. S. B., & Loeb, A. 2003, Astrophys. J., 595, 614